May 2021

Extracting Information from Compact Binary Coalescences with Gravitational Waves

Xiaoshu Liu
University of Wisconsin-Milwaukee

EXTRACTING INFORMATION FROM COMPACT BINARY COALESCENCES WITH GRAVITATIONAL WAVES

by

Xiaoshu Liu

A Dissertation Submitted in
Partial Fulfillment of the
Requirements for the Degree of

Doctor of Philosophy
in Physics

at
The University of Wisconsin-Milwaukee
May 2021

ABSTRACT

EXTRACTING INFORMATION FROM COMPACT BINARY COALESCENCES WITH GRAVITATIONAL WAVES

by

Xiaoshu Liu

The University of Wisconsin-Milwaukee, 2021
Under the Supervision of Professor Jolien Creighton

Gravitational waves (GWs) radiated by compact binary coalescences (CBCs) carry useful information about their sources. These source properties obtained via the parameter estimation technique can help us to answer a wide range of physics problems. In this dissertation, I will present three major research projects. Firstly, binary neutron stars (BNSs) detected by Advanced LIGO and Advanced Virgo are ideal to study the equation of state (EoS). The EoS enters GW waveforms through tidal deformability, which can be measured by Advanced LIGO and Advanced Virgo. By performing Bayesian model selection, we can test plausible models from a large set of proposed EoSs. Secondly, the time delay between GW detectors can be used to measure the speed of gravitational waves. Although the uncertainty of results produced by this method is larger than using the time delay between GW and gamma-ray burst (GRB), it does provide a model independent means to measure the speed of gravitational waves. Finally, gravitational waves that lensed by galaxies or galaxy clusters are expected to produce multiple images with the time delay ranging from minutes to months. The fact that lensed GW signals are sharing some source properties allows us to identify potential lensed GW events by comparing Bayesian evidences between individual parameter estimation runs and joint parameter estimation runs.

TABLE OF CONTENTS

LIST OF FIGURES

LIST OF TABLES

ACKNOWLEDGMENTS

I would like to thank my adviser Jolien Creighton for guiding me during my graduate school years, and for proving insights in research projects that I have worked on. I would like to thank Shaon Ghosh, Ignacio Magaña Hernandez, Shasvath Kapadia, and Patrick Brady for useful discussions and advice. I would like to thank Phil Chang, David Kaplan, and Alan Wiseman for being my dissertation committee members and for your useful comments. I would like to thank all members of the Physics department at UWM for helping me over the years.

I would like to thank all my collaborators in the LIGO-Virgo scientific collaboration, especially, Otto Hannuksela, K. Haris, Rico K. L. Lo, Jose Ezquiaga, David Keitel, Will Farr, Jay Tasson, Greg Ashton, Chris Pankow, and Les Wade.

I would like to thank for computational resources provided by the LIGO Laboratory and those provided by the Leonard E. Parker Center for Gravitation, Cosmology and Astrophysics at the University of Wisconsin–Milwaukee. This work was supported by NSF awards PHY-1607585 and PHY-1912649.

PREFACE

This dissertation is organized as follows. In Chapter 1, I review gravitational-wave astronomy and observations made by Advanced LIGO and Advanced Virgo. In Chapter 2, I give an introduction to Bayesian parameter estimation, which is the main technique used to produce results in Chapter 3, 4, and 5. Chapters 3, 4, and 5 describe original work I either led or substantially contributed to as part of my doctoral studies. In Chapter 3, I present results of measuring the tidal deformability of neutron stars and neutron star equation of state model selection for GW170817 and GW190425. In Chapter 4, I present results of measuring the speed of gravitational waves, which then can be used to test the general theory of relativity. In Chapter 5, I present results of identifying potential lensed gravitational-wave events using Bayesian model selection.

Chapter 1

Introduction

1.1 Introduction to gravitational waves

1.1.1 Linearized gravity

The Einstein field equations

$$G_{\alpha\beta} = \frac{8\pi G}{c^4} T_{\alpha\beta}, \tag{1.1}$$

relate geometry of spacetime to the matter. Here, $G_{\alpha\beta}$ is the Einstein tensor, which describes the curvature of spacetime. G and c are the gravitational constant and the speed of light in vacuum, respectively. $T_{\alpha\beta}$ is the stress-energy tensor, which is the combination of the energy density, the momentum density, and the stress tensor.

In the weak-field approximation, we can write the spacetime metric $g_{\alpha\beta}$ as the Minkowski metric $\eta_{\alpha\beta}$ plus a small perturbation $h_{\alpha\beta}$:

$$g_{\alpha\beta} = \eta_{\alpha\beta} + h_{\alpha\beta}. \tag{1.2}$$

In a four-dimensional Euclidean space, $\eta_{\alpha\beta}$ can be expressed as

$$\begin{bmatrix} -c^2 & 0 & 0 & 0 \\ 0 & 1 & 0 & 0 \\ 0 & 0 & 1 & 0 \\ 0 & 0 & 0 & 1 \end{bmatrix}. \tag{1.3}$$

To simplify the calculation in the Einstein tensor, we introduce the trace-reversed metric perturbation $\bar{h}_{\alpha\beta}$, which is defined by

$$\bar{h}_{\alpha\beta} = h_{\alpha\beta} - \frac{1}{2}\eta_{\alpha\beta}h. \tag{1.4}$$

Note that $h = -\eta^{\alpha\beta}\bar{h}_{\alpha\beta} = -\bar{h}$. Then under the Lorenz gauge condition $\partial\bar{h}^{\mu\alpha}/\partial x^{\mu} = 0$, the linearized Einstein field equations become

$$\Box\bar{h}_{\alpha\beta} = -\frac{16\pi G}{c^4}T_{\alpha\beta}, \tag{1.5}$$

where $\Box$ is the d'Alembertian operator.

1.1.2 Propagation of gravitational waves

Eq. (1.5) is a wave equation with a source provided by the stress-energy tensor. In the vacuum, the linearized Einstein field equations for the trace-reversed metric become

$$\Box\bar{h}_{\alpha\beta} = 0. \tag{1.6}$$

The solution to the Eq. 1.6 for the metric perturbation is called a gravitational wave (GW), which is traveling at the speed of light. The Lorenz gauge implies the the wave is transverse, one can further choose a gauge along with the Lorenz gauge to make the metric perturbation purely spatial $h_{0i} = 0$ and traceless $h^i_i = 0$, and the gauge is called transverse

traceless gauge (TT gauge). The transverse traceless gauge also exhibits that gravitational waves have two polarizations. For a GW traveling along z direction, the non-vanishing components in the TT gauge are:

$$h_{11}^{TT} = -h_{22}^{TT} = h_{+}(t - z/c), \tag{1.7}$$

$$h_{12}^{TT} = h_{21}^{TT} = h_{\times}(t - z/c). \tag{1.8}$$

In a non-vacuum spacetime, the Einstein equations are

$$\Box \bar{h}_{\alpha\beta} = -\frac{16\pi G}{c^4} T_{\alpha\beta} + O(h^2), \tag{1.9}$$

where the $O(h^2)$ term is the second order in the metric perturbation. This term can be interpreted as the contribution of the gravitational radiation itself to the stress-energy tensor. We can combine the $T^{\alpha\beta}$ and $O(h^2)$ by introducing the effective stress-energy tensor $\tau^{\alpha\beta}$, then Eq. (1.9) can be written as

$$\Box \bar{h}_{\alpha\beta} = -\frac{16\pi G}{c^4} \tau_{\alpha\beta}. \tag{1.10}$$

In the far-field zone, where the distance (r) between the source and the observer is much greater than the gravitational-wave wavelength, which is much greater than the size of the source, the solution to Eq. (1.10) is [1]

$$h_{ij} \approx \frac{2G}{c^4 r} \ddot{I}_{ij}(t - r/c), \tag{1.11}$$

where I_{ij} is the quadrupole tensor:

$$I_{ij}(t) = \int x^i x^j \tau^{00}(t - r/c, \vec{x}) d^3\vec{x}. \tag{1.12}$$

In the transverse traceless gauge, we can use the projection operator $P_{ij} = \delta_{ij} - \hat{n}_i\hat{n}_j$ to project the quadrupole tensor: $I_{ij}^{TT} = P_{ik}I^{kl}P_{lj} - 0.5P_{ij}P_{kl}I^{kl}$, where $\hat{n}_i = x^i/r$ is the unit vector in the propagation direction. The solution to Eq. (1.10) in the TT gauge becomes

$$h_{ij}^{TT} \approx \frac{2G}{c^4 r}\ddot{I}_{ij}^{TT}(t - r/c), \tag{1.13}$$

1.1.3 Energy and luminosity of gravitational waves

Similar to electromagnetic waves, gravitational waves carry energy away from their sources. The effective stress-energy tensor is given by [2, 3]

$$T_{\alpha\beta}^{\mathrm{GW}} = \frac{c^4}{32\pi G}\left\langle \frac{\partial h_{TT}^{ij}}{\partial x^\alpha}\frac{\partial h_{ij}^{TT}}{\partial x^\beta}\right\rangle, \tag{1.14}$$

where $\langle . \rangle$ is an integral average over a spacetime region containing many wavelengths. For a gravitational plane wave traveling in z-direction, we find

$$T_{00}^{\mathrm{GW}} = -cT_{03}^{\mathrm{GW}} = -cT_{30}^{\mathrm{GW}} = c^2T_{33}^{\mathrm{GW}} = \frac{c^4}{16\pi G}\left\langle \dot{h}_+^2 + \dot{h}_\times^2\right\rangle, \tag{1.15}$$

and all other components vanish.

A gravitational wave with energy dE passing through an area dA in time dt is the gravitational-wave flux, which is given by

$$\frac{dE}{dtdA} = -\frac{c^3}{16\pi G}\left\langle \dot{h}_+^2 + \dot{h}_\times^2\right\rangle, \tag{1.16}$$

the gravitational-wave luminosity is

$$L_{GW} = -\frac{dE}{dt} = \frac{1}{5}\frac{G}{c^5}\left\langle \dddot{I}_{ij}\dddot{I}^{ij}\right\rangle, \tag{1.17}$$

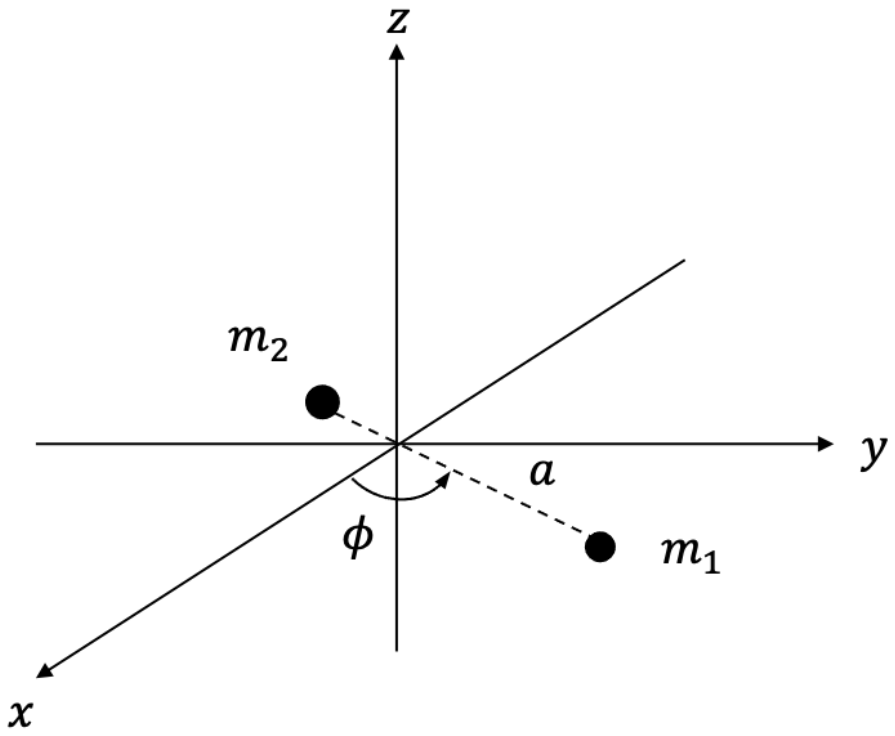

Figure 1.1: A binary system orbits on the x-y plane.

where $\mathcal{I}_{ij}$ is defined by

$$\mathcal{I}_{ij} = \int (x^i x^j - \frac{1}{3} r^2 \delta_{ij}) \tau^{00}(\vec{x}) d^3\vec{x}. \tag{1.18}$$

1.1.4 Gravitational waves produced by orbiting binaries

Gravitational waves produced by compact binary coalescences are the only type of GW sources that have been detected by Advanced LIGO and Advanced Virgo so far. Suppose a binary system with the primary mass m_1 and the secondary mass m_2 in a circular orbit on the $x - y$ plane is rotating around its center of mass (Shown in Figure. (1.1)), and the separation of the two objects is a. The metric perturbation in the TT-gauge for an

observer at the angle of inclination ι is [1]

$$h_{ij}^{TT} = -\frac{4G\mu a^2\omega^2}{c^4 r}\begin{bmatrix} \frac{1+\cos^2\iota}{2}\cos 2\phi & \cos\iota\sin 2\phi & 0 \\ \cos\iota\sin 2\phi & -\frac{1+\cos^2\iota}{2}\cos 2\phi & 0 \\ 0 & 0 & 0 \end{bmatrix}, \tag{1.19}$$

where $\mu = m_1 m_2/M$ is the reduced mass of the system, $M = m_1 + m_2$ is the total mass of the system, a is the orbital separation, $\omega = \phi/t$. With the Kepler's third law, $GM = a^3\omega^2$, the two polarizations become

$$h_+ = -\frac{4G\mu}{c^2 r}\frac{1+\cos^2\iota}{2}\left(\frac{v}{c}\right)^2\cos 2\phi, \tag{1.20}$$

$$h_\times = -\frac{4G\mu}{c^2 r}\cos\iota\left(\frac{v}{c}\right)^2\sin 2\phi, \tag{1.21}$$

where $v = (GM\omega)^{1/3} = (\pi GMf)^{1/3}$. From Eq. (1.20, 1.21), we find the frequency of gravitational waves is the twice of the orbital frequency, $f = 2f_{\rm orbital} = \omega/\pi$.

The gravitational-wave luminosity is given by

$$L_{GW} = \frac{32}{5}\frac{c^5}{G}\eta^2\left(\frac{v}{c}\right)^{10}, \tag{1.22}$$

where $\eta = \mu/M$ is the symmetric mass ratio. The Newtonian energy of the binary system is

$$E = -\frac{1}{2}\mu v^2. \tag{1.23}$$

Since $L_{GW} = -dE/dt$, we find

$$\frac{d(v/c)}{dt} = \frac{32\eta}{5}\frac{c^3}{GM}\left(\frac{v}{c}\right)^9. \tag{1.24}$$

Then the time until coalescence τ_c can be obtained by integrating Eq. (1.24) to $v \to \infty$,

the result is

$$\tau_c = \frac{5}{256\eta}\frac{GM}{c^3}\left(\frac{\pi GM f_0}{c^3}\right)^{-8/3}, \tag{1.25}$$

where f_0 is the initial GW frequency.

1.1.5 Phase evolution and Newtonian chirp

Given the energy function $E(v)$ and the luminosity function $L_{\rm GW}(v)$, since $L_{\rm GW} = -dE/dt$, we have

$$t(v) = t_c + \int_v^{v_c} \frac{1}{L}\frac{dE}{dv}dv, \tag{1.26}$$

where t_c and v_c are the time at coalescence and velocity at the coalescence time, respectively. Then the phase evolution is given by

$$\phi(v) = \phi_c + \int_v^{v_c} \frac{v^3}{GM}\frac{dE}{dv}dv, \tag{1.27}$$

where ϕ_c is the phase at coalescence.

In the Newtonian limit, $E(v)$ and $L_{\rm GW}(v)$ are given by

$$E(v) = -\frac{1}{2}M\eta c^2\left(\frac{v}{c}\right)^2, \tag{1.28}$$

$$L_{\rm GW}(v) = \frac{32}{5}\frac{c^5}{G}\eta^2\left(\frac{v}{c}\right)^{10}. \tag{1.29}$$

Using Eq. (1.26,1.27) and assume $v_c \to \infty$, we find

$$t(v) = t_c - \frac{5}{256\eta}\frac{GM}{c^3}\left(\frac{v}{c}\right)^{-8}, \tag{1.30}$$

$$\phi(v) = \phi_c - \frac{1}{32\eta}\left(\frac{v}{c}\right)^{-5}. \tag{1.31}$$

Since the gravitational-wave frequency $f = v^3/(\pi GM)$,

$$\frac{df}{dt} = \frac{96}{5}\pi^{8/3}\left(\frac{GM_c}{c^3}\right)^{5/3} f^{11/3}, \tag{1.32}$$

where $M_c = \eta^{3/5}M$ is known as the chirp mass. The gravitational-wave waveform in the time domain can be written as

$$h_+ = -\frac{GM_c}{c^2 r}\frac{1+\cos^2\iota}{2}\left(\frac{c^3(t_c-t)}{5GM_c}\right)^{-1/4}\cos\left[2\phi_c - 2\left(\frac{c^3(t_c-t)}{5GM_c}\right)^{5/8}\right], \tag{1.33}$$

$$h_\times = -\frac{GM_c}{c^2 r}\cos\iota\left(\frac{c^3(t_c-t)}{5GM_c}\right)^{-1/4}\sin\left[2\phi_c - 2\left(\frac{c^3(t_c-t)}{5GM_c}\right)^{5/8}\right]. \tag{1.34}$$

As the orbit of a binary system decays due to radiate energy, the frequency and the amplitude of GWs increase, this is known as chirp. As we can see from Eq. (1.32, 1.33, 1.34), the frequency evolution and the waveform only depend on the chirp mass, not other combinations of component masses in the Newtonian chirp. In the relativistic case, other combinations of component masses (such as η) need to be taken into account.

1.1.6 Post-Newtonian wavefroms

In the previous section, we compute the waveforms in the Newtonian limit in which the orbital velocity is much less than the speed of light $v \ll c$. However, in the relativistic case, the Newtonian results are not accuracy to model binary systems. One method that is widely used in modeling such case is known as post-Newtonian (PN) theory, which expands the equations of motion in General Relativity and adds relativistic corrections to the Newtonian results. Different waveform models arise from different methods of truncating a PN power series.

A commonly used PN waveform model in the gravitational-wave data analysis is the TaylorF2 waveform. The TaylorF2 is a post-Newtonian waveform in the frequency domain

that is computed via the Fourier transform with the stationary phase approximation, the waveform is [4]

$$\tilde{h}_+(f) \approx -\frac{1+\cos^2\iota}{2}\left(\frac{5\pi}{24}\right)^{1/2}\eta^{1/2}\frac{G^2M^2}{c^5r}x^{-7/4}e^{-2\pi i f t_c}e^{2\pi i\phi_c}e^{-i\Phi(f)}, \tag{1.35}$$

$$\tilde{h}_\times(f) \approx i\cos\iota\left(\frac{5\pi}{24}\right)^{1/2}\eta^{1/2}\frac{G^2M^2}{c^5r}x^{-7/4}e^{-2\pi i f t_c}e^{2\pi i\phi_c}e^{-i\Phi(f)}, \tag{1.36}$$

where $x = (GM\omega/c^3)^{2/3}$ is the post-Newtonian parameter, $\Phi(f)$ is the stationary phase function. $\Phi(f)$ depends on the PN order that is used for the calculation, the currently known PN orders are up to 3.5PN ($x^{3.5}$) [5].

1.2 Detection of gravitational waves

1.2.1 Sources of gravitational waves

From the previous section, we have concluded that in order to radiate gravitational waves, the system must have a non-vanishing second derivative of the quadrupole moment with respect to time. Any rotating binary (e.g. the Earth orbiting the Sun) emits gravitational waves; however, in order to be observed by GW detectors, the masses must be large, the orbiting velocity must be large, and the density of the objects must be high enough to produce strong gravitational fields. Compact binaries such as binary neutron stars and binary black holes with mass between 1 $M\odot$ and 1000 $M\odot$ produce gravitational waves in the high frequency band (between 1 Hz and 10 kHz). The ground-based GW detectors (e.g. LIGO and Virgo) are sensitive to frequencies in this band. Compact binaries such as binary white dwarfs and supermassive black holes ($M \sim 10^3$ $M\odot$ to 10^9 $M\odot$) produce gravitational waves in the low frequency band (1 mHz - 1 Hz), which need to be observed by space-based GW detectors such as LISA.

Apart from compact binary coalescences, gravitational waves can also be produced

by rotating systems such as spinning neutron stars that are not axis-symmetric due to deformation in their structures. Gravitational waves produced by those systems have some particular steady frequencies over some period of time which is longer than the observational time. This type of gravitational waves is known as continuous gravitational waves. Binary systems can also produce continuous gravitational waves when their orbital decay timescale is much longer than the observational timescale.

Gravitational waves emitted from astrophysical phenomena that happen in a short duration such as supernovae, stellar core collapse, or gamma-ray bursts are called burst gravitational waves. Modeling gravitational waves from some such systems is challenging because we do not well enough know physics of the systems, which makes it difficult to detect burst gravitational waves.

Gravitational waves produced by cosmological sources in the early evolution of the Universe are known as stochastic gravitational waves. These gravitational waves are produced by many random independent events and may carry information about the early Universe. However, these signals are very weak and random, which makes it difficult to detect the gravitational-wave background.

1.2.2 Gravitational-wave observation by Advanced LIGO and Advanced Virgo

The Laser Interferometer Gravitational-Wave Observatory (LIGO) is a ground based gravitational-wave detector. It uses laser interferometry to detect small changes in the length of optical path when gravitational waves arrive. There are two detectors located in the United States, one of them is located in Hanford, WA, and the other is located in Livingston, LA. Each observatory is L-shaped with a 4 km long arm on each side (shown in Figure 1.2), and uses a dual-recycled Fabry-Perot Michelson Interferometer [1].

The initial LIGO operated in the early 2000s, but no GW events were observed. The detectors were then upgraded to Advanced LIGO [6], and they started the first observing

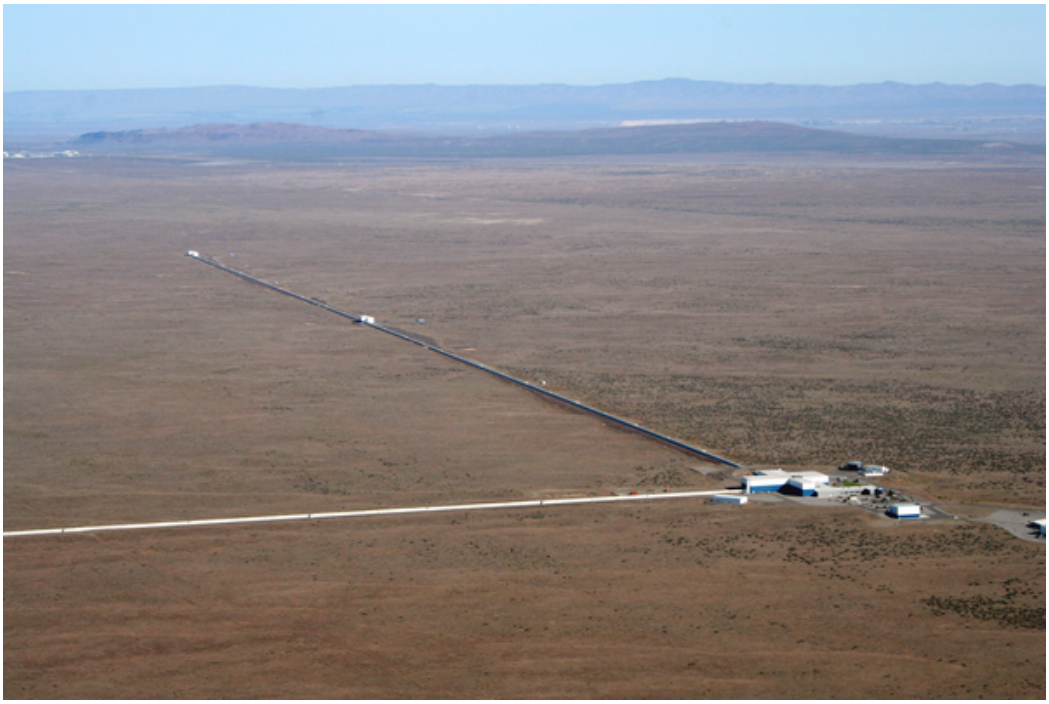

Figure 1.2: Image of LIGO Hanford Observatory, each arm is 4 km long. Image source: https://www.ligo.caltech.edu.

run (O1) in September 2015. On September 14, 2015, the first gravitational-wave event GW150914 was observed simultaneously by the two Advanced LIGO detectors[7]. It is the first detection of gravitational waves, which came about one hundred years after the prediction of the existence of GWs by Einstein in 1916, and is the first direct observation of a binary black hole (BBH) merger. The gravitational waves were produced by a binary black hole merger with total mass $\sim 60\ M_{\odot}$, and distance ~ 400 Mpc. During the first observing run, which took place from September 12th, 2015 to January 19th, 2016, the two additional BBHs GW151012 [8] and GW151226 [9] were also detected by Advanced LIGO.

The second observing run (O2) of the Advanced LIGO took place from November 30th, 2016 to August 25th, 2017. In the later O2, Advanced Virgo [10] joined the observation, which formed a three-detector network [11].

The first observation of a binary neutron star system PSR B1913+16 was made by Hulse and Taylor in 1970s [12]. Subsequent observations made by Taylor and Weisberg discovered the decay of the orbit of PSR B1913+16 [13] due to the emission of gravita-

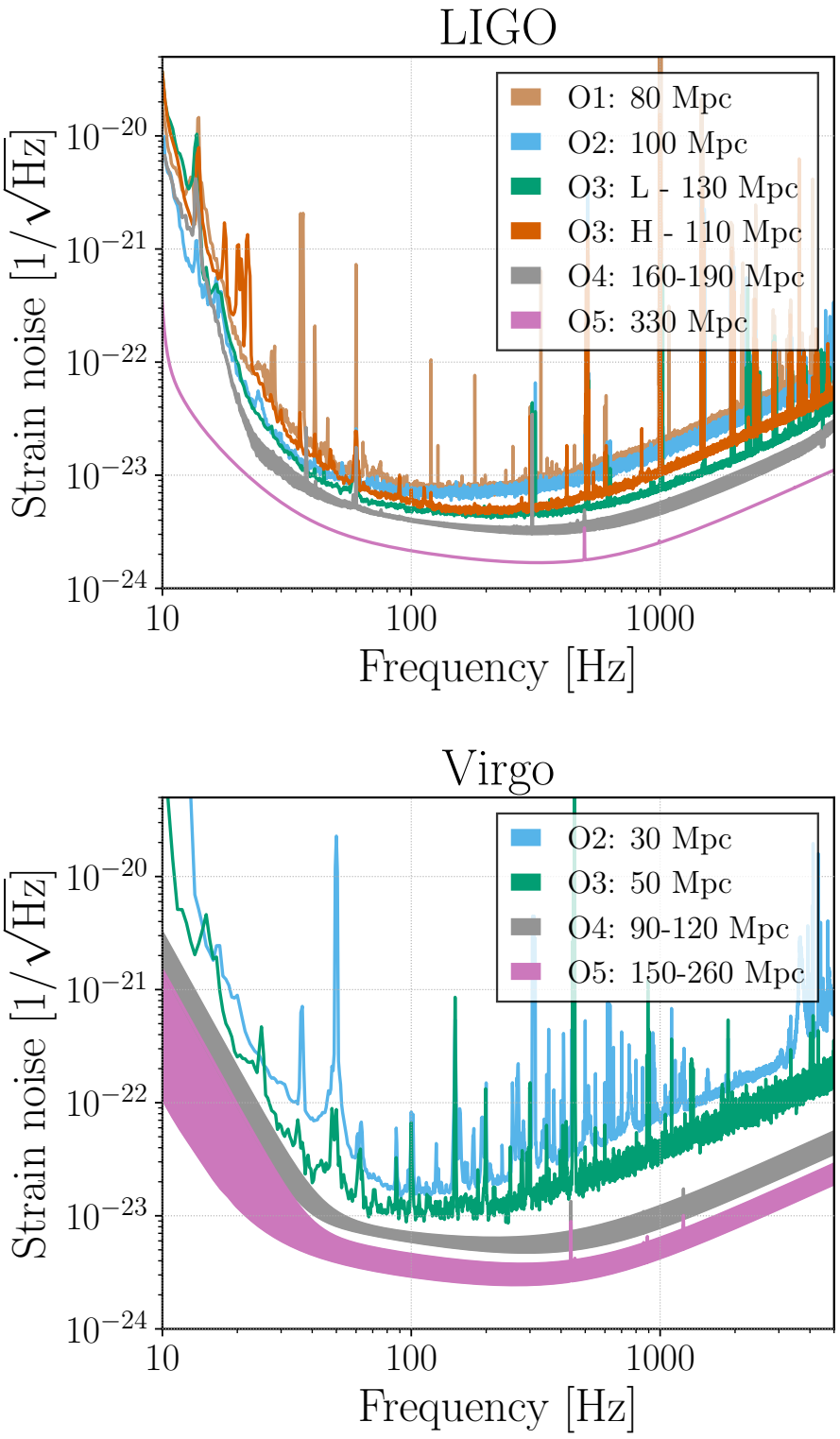

Figure 1.3: Sensitivity curves of Advanced LIGO (top) and Advanced Vrigo (bottom) as a function of frequency, the quoted range is for 1.4 $M_\odot - 1.4\ M_\odot$ BNS system. Image source: https://dcc.ligo.org/LIGO-P1200087/public.

tional waves, which is the first indirect evidence of the existence of GWs. On August 17, 2017, Advanced LIGO and Advanced Virgo made the first direct observation of a binary neutron star inspiral, GW170817 [14]. The total mass of the BNS was $\sim 2.7\ M_{\odot}$ and had a luminosity distance of ~ 40 Mpc. About 1.74s later, the gamma-ray burst (GRB) counterpart GRB 170817A was observed by Fermi Gamma-ray Burst Monitor and the Anti-Coincidence Shield for the Spectrometer for the International Gamma-Ray Astrophysics Laboratory [15]. The subsequent electromagnetic (EM) follow-up observations identified the host galaxy of GW170817 as NGC 4993 [16]. During O2, seven BBHs GW170104, GW170608, GW170729, GW170809, GW170814, GW170818, and GW170823, were also detected by Advanced LIGO and Advanced Virgo [17].

The third observing run (O3) was divided into to O3a and O3b, with O3a from April 1st, 2019 to September 30th, 2019, and O3b from November 1st, 2019 to the end of March, 2020. Due to the increase in the sensitivity, 39 gravitational-wave events were detected in O3a [18]. The least massive binary detected in O3a was GW190425 [19] with total mass $\sim 3.4\ M_{\odot}$. Although the component masses are consistent with the masses of known neutron stars, the total mass is significantly larger than known Galactic BNSs. Given that tidal deformability was not detected and the lack of the EM counterpart, the probability that the system consists of one or two black holes cannot be ruled out [19]. Short after the detection of GW190425, Advanced LIGO and Advanced Virgo observed a high false alarm rate (FAR) event GW190426 [18], which had the primary mass $m_1 \sim 5.7\ M_{\odot}$, and the secondary mass $m_2 \sim 1.5\ M_{\odot}$. Although the secondary mass is consistent with the mass of a neutron star, the data do not provide evidence to reject the probability of being a black hole; thus implies the system could be a BBH or a neutron star–black hole (NSBH) if the signal is real. In addition to GW190426, there is another potential NSBH GW event GW190814 [20] detected in O3a. The secondary mass of GW190814 is $\sim 2.6\ M_{\odot}$, which makes the interpretation as BBH or NSBH unclear. The primary mass is $\sim 23 M_{\odot}$, resulting in an extreme mass ratio $q = \dfrac{m_2}{m_1} \sim 0.11$. In the BBHs observed in O3a, there is

an interesting event GW190521 [21, 22]. GW190521 is the heaviest binary with the total mass $\sim 150M_{\odot}$ that has been observed by Advanced LIGO and Advanced Virgo so far. The remnant with mass $\sim 142M_{\odot}$ can be considered to be an intermediate mass black hole (IMBH) [21, 22].

As the results of improvements in the sensitivity of Advanced LIGO (shown in Figure and Advanced Virgo (See Figure 1.3)), there will be more events detected in the future as well as increased range of the detection. The Advanced LIGO detection range for a 1.4 $M_{\odot}$ − 1.4 $M_{\odot}$ BNS system would reach 330 Mpc incorporating A+ upgrade in the fifth observing run (O5) [23]; this would be a dramatic improvement on the current O3 sensitivity (110 Mpc - 130 Mpc). Moreover, LIGO-India will join in O5 with a design sensitivity of 330 Mpc, and KAGRA is expected to reach a sensitivity of 130+ Mpc in O5 [23]. The network composed of five gravitational-wave detectors will help to better localize GW sources, as well as help to improve measurement accuracy of other source parameters. The accurate measurement of the sky localization can help astronomers to facilitate electromagnetic follow-up searches for GW transients such as BNSs and NSBHs.

Chapter 2

Parameter estimation for gravitational waves

2.1 Introduction

Since the first observation of gravitational waves on September 14, 2015, there are more than 50 GW events that have been detected by Advanced LIGO and Advanced Virgo. The accurate estimation of source parameters is crucial for understanding the physical properties and implying the underlying physical processes. Accurate measurements of masses allow us to establish mass distributions for BBH, BNS, and NSBH, as well as to study population properties. Also, the mass distributions can be used to determine the minimum mass of a black hole and the maximum mass of a neutron star, which then can be used to test the existence of a mass gap [24] between neutron stars and black holes. Accurate measurements of the tidal deformability of neutron stars and their masses provided information about the underlying equation of state [25, 26]. Moreover, the Hubble constant can be estimated by the luminosity distance measured by GWs along with EM observations of the source redshift [27, 28]. This method dose not require the use of a cosmic distance ladder in the previous measurements [29]. Accurate measurements of the sky localization

of a GW event can help to localize the host galaxy, and the corresponding EM counterpart can be identified if the source emits electromagnetic waves. This would allow observe the same compact binary objects in multi-messenger astronomy [16]. Finally, gravitational waves produced by compact binary objects provide opportunities to test general relativity that cannot be achieved with other types of observations [30, 31, 32].

2.2 Bayesian inference

The gravitational-wave data collected at a GW detector is d. Our goal is to estimate the source parameters ($\vec{\theta}$) that produced this data. Bayesian inference is a means to achieve this by using Bayes' theorem:

$$p(\vec{\theta}|d) = \frac{p(d|\vec{\theta})p(\vec{\theta})}{p(d)}. \tag{2.1}$$

Here, $p(\vec{\theta}|d)$ is the posterior distribution of parameters $\vec{\theta}$ conditional on data d; $p(\vec{\theta})$ is the prior distribution of $\vec{\theta}$ before the data is collected, and $\int p(\vec{\theta})d\vec{\theta} = 1$; $p(d|\vec{\theta})$ is the likelihood function, which is the conditional distribution of data d given parameters $\vec{\theta}$; $p(d)$ is known as the evidence, and it can be computed by marginalizing likelihood: $p(d) = \int p(d|\vec{\theta})p(\vec{\theta})d\vec{\theta}$. The evidence is not important in the case of parameter estimation as it is simply a normalization constant. However, in model selection problems, the ratio of evidences can be used to select a model that fits data better. Since the evidence is not a function of parameters $\vec{\theta}$, Eq. (2.1) can be written as:

$$p(\vec{\theta}|d) \propto p(d|\vec{\theta})p(\vec{\theta}). \tag{2.2}$$

This means to compute the posterior we do not need to evaluate the evidence explicitly, because it is just a normalization constant and it does not affect the posterior distributions of the parameters. Sometimes we might be only interested in the single parameter $\theta_1 \in \vec{\theta} =$

$\{\theta_1, \theta_2, \ldots, \theta_N\}$, the marginalized posterior can be found by integrated out other unwanted parameters:

$$p(\theta_1|d) = \int p(\vec{\theta}|d) d\theta_2 d\theta_3 \ldots d\theta_N \tag{2.3}$$

The evidence $Z' = \int p'(d|\vec{\theta}) p'(\vec{\theta}) d\vec{\theta}$ computed with likelihood $p'(d|\vec{\theta})$ and prior $p'(\vec{\theta})$ can be reweighted to obtain Z for another likelihood $p(d|\vec{\theta})$ and prior $p(\vec{\theta})$ without running the analysis again. Multiply the right-hand side of Eq. (2.1) by $p'(\vec{\theta}|d)/p'(\vec{\theta}|d)$

$$\begin{aligned} p(\vec{\theta}|d) &= \frac{p(d|\vec{\theta}) p(\vec{\theta})}{p(d)} \frac{p'(\vec{\theta}|d)}{p'(\vec{\theta}|d)} \\ &= Z' \frac{p'(\vec{\theta}|d)}{Z} \frac{p(d|\vec{\theta})}{p'(d|\vec{\theta})} \frac{p(\vec{\theta})}{p'(\vec{\theta})}. \end{aligned} \tag{2.4}$$

Since the posterior is normalized $\int p(\vec{\theta}|d) d(\vec{\theta}) = 1$, by integrating over $p(\vec{\theta})$ on both sides of the above equation, we obtain

$$\begin{aligned} Z &= Z' \int p'(\vec{\theta}|d) \frac{p(d|\vec{\theta})}{p'(d|\vec{\theta})} \frac{p(\vec{\theta})}{p'(\vec{\theta})} d(\vec{\theta}) \\ &= \frac{Z'}{n} \sum_{k=0}^{n-1} w(d|\vec{\theta}_k) w(\vec{\theta}_k), \end{aligned} \tag{2.5}$$

where $w(d|\vec{\theta}) = \dfrac{p(d|\vec{\theta})}{p'(d|\vec{\theta})}$ and $w(\vec{\theta}) = \dfrac{p(\vec{\theta})}{p'(\vec{\theta})}$ are the weighted function of likelihood and weighted function of prior, respectively. Eq. (2.5) can be evaluated by sum over n discrete posterior samples $p'(\vec{\theta}|d)$ [33]. Thus, we can reweight the evidence to any prior or likelihood distribution that is different from the one used in the current analysis.

The ratio of evidences is useful when we wish to compare which model fits data better:

$$B^{H_0}_{H_1} = \frac{p(d|H_0)}{p(d|H_1)}, \tag{2.6}$$

where H_0 and H_1 represent two different models. The ratio $B^{H_0}_{H_1}$ is known as the Bayes factor, which quantifies how much more likely one model is supported by the data than

the other. If we have prior information about models before we analyze the data, then the product of the Bayes factor and the ratio of prior of the models is the odds

$$O = \frac{p(d|H_0)}{p(d|H_1)} \frac{p(H_0)}{p(H_1)} = \frac{p(H_0|d)}{p(H_1|d)}. \tag{2.7}$$

The prior used in the gravitational wave analysis is usually uniform and isotropic on the parameters, because of lacking information about the source properties before gravitational-wave signals arrive at GW detectors. For example, the component masses m_1 and m_2 are usually chosen to be uniformly distributed in a certain range, e.g. $1 < m_1, m_2 < 3$ for a BNS analysis, although the actual unknown distribution of the population might not be uniform. The homogeneous and isotropic prior is used for the right ascension α, declination δ, luminosity distance D_L, and inclination ι. α is uniform between 0 and 2π, $\delta \propto \cos\delta$ between $-\pi/2$ and $\pi/2$, $D_L \propto D_L^2$, and $\iota \propto sin\iota$ between 0 and π. Notice that cos and sin prior are uniform in sin and cos, respectively. The prior for polarization angle ψ is uniform from 0 to π and the prior for coalescence phase is uniform from 0 to 2π. For the aligned spin case, we use uniform prior in dimensionless spin magnitude $a_i = |cS_i/(Gm_i^2)|$, where S_i is the spin angular momentum. For black holes the prior range of a_i is between 0 and 1. For neutron stars, the limit of available rapid waveform models has dimensionless spin magnitude $a_i \sim 0.89$ [14], note that the fastest-spinning known neutron star has $a_i \leq 0.04$ [34]. We also apply a small time window ($\pm 0.1s$) centered on the coalescence time t_c found by a search pipeline to accommodate the uncertainties of t_c and termination times of different waveforms. Priors that are used for analyzing a typical BBH with aligned spin waveforms are summarized in Table (2.1). Priors used for BNSs will be discussed in Charpter 3.

Table 2.1: Priors for parameters used for analysis aligned spin BBHs, the minimum and maximum values are estimated based on typical BBHs detected in the first two observing runs of Advanced LIGO and Advanced Virgo.

parameter	prior	minimum	maximum
$m_{1,2}$	uniform	1 $M_\odot$	100 $M_\odot$
D_L	$D_L \propto D_L^2$	1 Mpc	5000 Mpc
α	uniform	0	2π
δ	$\delta \propto \cos\delta$	$-\pi/2$	$\pi/2$
ι	$\iota \propto \sin\iota$	0	π
ϕ	uniform	0	2π
ψ	uniform	0	π
$a_{1,2}$	uniform	0	1
t_c	uniform	-0.1s	0.1s

2.3 Gravitational-wave signals in noisy data

The data $d(t)$ collected at a GW detector can be modeled as the sum of pure gravitational-wave signal $h(t)$ and noise $n(t)$:

$$d(t) = h(t) + n(t). \tag{2.8}$$

The GW signal is the combination of $h_+(t), h_\times(t)$ with antenna response functions [35] $F_+, F_\times$:

$$h(t) = F_+ h_+(t) + F_\times h_\times(t). \tag{2.9}$$

The antenna beam pattern F_+ and $F_\times$ not only depend on the sky location and polarization angle, they also depend on the orientation of a detector and the signal arrival time.

We assume the noise $n(t)$ is stationary Gaussian distributed. Stationary means the mean and variance are constant over time. According to the central limit theorem, the sum of independent random variables tend to be Gaussian distributed, even if each original random variable is not Gaussian distributed. Thus, we expect the sum of multiple

independent types of noise is approximately Gaussian distributed. The above assumption of the noise allow us to construct the likelihood function in the form of

$$p(d|\vec{\theta}) \propto \exp\left\{-\sum_{i=0}^{N-1}\frac{(d_i-h_i)^2}{2\sigma^2}\right\}, \tag{2.10}$$

where we assume noise is white noise with the standard deviation σ, N is the number of sample points. The power spectral density (PSD) $S_x(f)$ of a stationary time series $x(t)$ is defined by

$$S_x(f) = \lim_{T\to\infty}\frac{2}{T}\left|\int_{-T/2}^{T/2} x(t)e^{-2\pi ift}dt\right|^2. \tag{2.11}$$

Eq. (2.10) can then be written as [1]

$$p(d|\vec{\theta}) \propto \exp\left\{-2\int_0^\infty \frac{|\hat{d}(f)-\hat{h}(f)|^2}{S_n(f)}\right\}, \tag{2.12}$$

where $\hat{d}(f) = \int_{-\infty}^{\infty} d(t)e^{-2\pi ift}dt$ and $\hat{h}(f) = \int_{-\infty}^{\infty} h(t)e^{-2\pi ift}dt$ are the Fourier transform of the data $d(t)$ and the waveform $h(t)$, respectively. For a k-detector network, the likelihood is the product of the likelihood for each detector:

$$p(d|\vec{\theta}) = \prod_{i=1}^{k} p_i(d|\vec{\theta}), \tag{2.13}$$

where $p_i(d|\vec{\theta})$ is the likelihood for the ith detector.

Consider the null hypothesis H_0 where the data only contains noise: $d(t) = n(t)$, and the alternative hypothesis H_1 where the data contains both signal and noise: $d(t) = h(t)+n(t)$, the likelihood ratio of the two hypotheses is

$$\Lambda = \frac{p(d|H_0)}{p(d|H_1)} = \exp\left\{4\int_0^\infty \frac{\hat{d}(f)\hat{h}^*(f)}{S_n(f)}df\right\}\exp\left\{-2\int_0^\infty \frac{|\hat{h}(f)|^2}{S_n(f)}df\right\}. \tag{2.14}$$

The term

$$\rho_o = \sqrt{4 \int_0^\infty \frac{|\hat{h}(f)|^2}{S_n(f)} df} \tag{2.15}$$

is called the optimal signal-to-noise ratio (SNR).

$$\rho_m = 4 \int_0^\infty \frac{\hat{d}(f)\hat{h}^*(f)}{S_n(f)} df \tag{2.16}$$

is known as the matched filter SNR, where the template h is normalized.

The traditional method of estimating PSD from a GW detector is based on the Welch's method [37] on off-source data. The recent developed method called BayesWave [38, 39] is widely used in computing PSD for gravitational waves. This method models the noise PSD using cubic splines to fit to the broad-band spectrum and Lorentzians for narrow-band line features, and using reversible jump Markov Chain Monte Carlo (RJMCMC) [40] to sample between different models that might have different number of parameters [39]. Then the median of the posterior of PSDs is obtained as a point estimate to approximate the full structure. Figure (2.1) shows the comparison of the two PSD estimation methods for GW170817.

2.4 Waveforms

There are several waveform models that have been developed to model gravitational waves. TaylorF2 is a post-Newtonian waveform in the frequency domain, which is discussed in Sec. (1.1.6). However, since TaylorF2 is a point particle waveform, it becomes inaccurate to describe BBHs during the merger and ringdown stages. Frequency domain phenomenological waveforms such as IMRPhenomD [41, 42] using post-Newtonian formalism during the inspiral and numerical relativity during the merger and ringdown stages to from a hybrid waveform. Thus, phenomenological waveforms can be used to describe inspiral-merger-ringdown (IMR) of a BBH. Another waveform can be used to model inspiral-merger-ringdown of

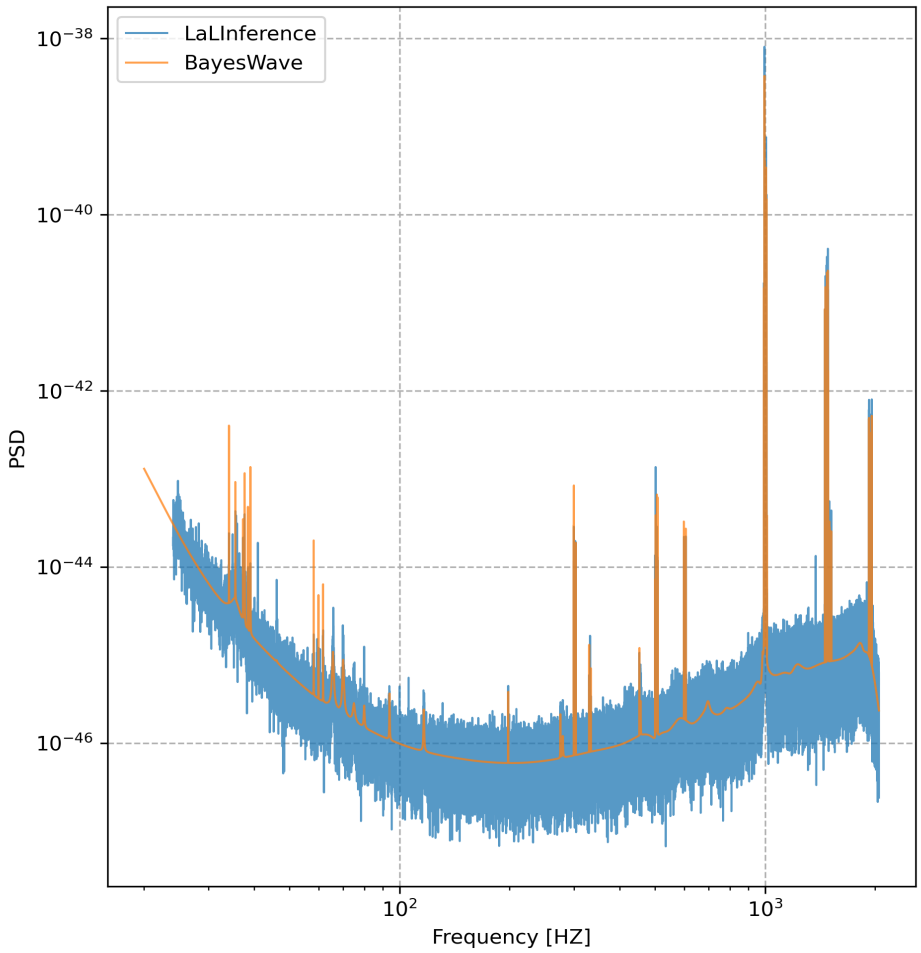

Figure 2.1: PSDs of GW170817 for the LIGO Hanford detector. The blue PSD is computed using LALInference [36], which implemented a method of computing PSD based on the Welch's method; the orange PSD is computed with BayesWave.

BBHs is effective one body (EOB) formalism, which models relativistic two-body problem as a test particle moving in an effective external metric [43].

These waveforms can be used to model more complicated systems by adding extra terms in the base waveforms. For example, IMRPhenomPv2 [44] that produced by adding precessing spin terms in IMRPhenomD can be used to model binary systems with precession; IMRPhenomHM [45] that produced by adding higher modes in IMRPhenomD can be used to produce more accurate results than $(2, 2)$-mode waveforms. Moreover, by adding tidal terms at the 5PN order and higher, TaylorF2 can be used to model BNSs with tidal deformability; by adding NRTidal [46, 47] terms that are calibrated to numerical relativity to IMRPhenomD and SEOBNRv4_ROM [48, 49] waveforms, the IMRPhenomPv2_NRTidal and SEOBNRv4_ROM_NRtidal can be used to describe BNSs. The state-of-the-art waveforms used in gravitational-wave data analysis can be found in Ref. [18].

2.5 Markov Chain Monte Carlo and Nested sampling

2.5.1 Markov Chain Monte Carlo

The objective of the parameter estimation is to find the posterior distribution $p(\vec{\theta}|d)$. For an aligned BBH, $\vec{\theta} = \{m_1, m_2, D_L, \iota, \alpha, \delta, \phi, \psi, t_c, a_1, a_2\}$ is an 11 dimensional vector; hence, the posterior is a complicated multi-dimensional distribution, which is difficult to sample with direct sampling. To effectively sample the posterior, Markov Chain Monte Carlo (MCMC) with Metropolis–Hastings algorithm [50, 51] is widely used in gravitational-wave data analysis[52]. Note that in MCMC, we only need to provide the likelihood $p(d|\vec{\theta})$ and the prior $p(\vec{\theta})$, and the normalization constant (the evidence $p(d)$) can be computed afterwards if one needs to conduct a model selection study. The process of drawing random samples using MCMC with Metropolis–Hastings algorithm from a posterior distribution is presented here:

1. Draw an initial point $\vec{\theta}_0$, which can be from the prior $p(\vec{\theta})$. For each parameter,

the prior is usually a simple 1-dimensional function that is independent of other parameters, which can be generated using a more direct sampling method.

2. For i in 1,2,3,...,N:

   - Draw a sample $\vec{\theta}_i$ according to a jump proposal $q(\vec{\theta}_i|\vec{\theta}_{i-1})$, which gives a probability distribution of moving $\vec{\theta}_{i-1}$ to $\vec{\theta}_i$.
   - Compute the acceptance ratio $r = \min\left\{1, \frac{q(\vec{\theta}_{i-1}|\vec{\theta}_i)}{q(\vec{\theta}_i|\vec{\theta}_{i-1})}\frac{p(d(\vec{\theta}_i|d))}{p(d(\vec{\theta}_{i-1}|d))}\right\}$.
   - Generate a random number n between 0 and 1, accept the new point $\vec{\theta}_i$ if $r \geq n$; otherwise, set $\vec{\theta}_i = \vec{\theta}_{i-1}$.

3. Obtain the marginalized posterior samples for each parameter by discarding samples during the burn-in stage.

Note that during the burn-in stage, samples are not guaranteed to be drawn from the posterior; thus, those points must be discarded during the post-processing. The log-likelihood is expected to be close to $L_{max} - Y$ [36], where L_{max} is the maximum value of the log-likelihood in the chain, Y is a random variable following a Gamma$(d/2, 1)$ distribution, d is the number of dimensions of $\vec{\theta}$. Thus, The end of burn-in stage can be chosen when the log-likelihood value is within $d/2$ of the maximum value of the log-likelihood.

The adjacent samples are usually correlated as the ith sample depends on the $(i-1)$th sample; rather than store every sample at each step, we can instead skip every k (e.g. 100) samples before we store one. Another way to remove correlated samples is to compute the integrated autocorrelation time (ACT) τ [36]:

$$\tau = 1 + 2\sum_{t=0}^{T-1} \hat{c}(t), \tag{2.17}$$

where T is the length of the series, and $\hat{c}(t)$ is the autocorrelation coefficient of the sample

x at the lag t:

$$\hat{c}(t) = \frac{\sum_{k=t}^{T-1}(x_k - \bar{x})(x_{k-t} - \bar{x})}{\sum_{k=0}^{T-1}(x_k - \bar{x})^2}, \tag{2.18}$$

where $\bar{x}$ is the mean of x. The range of $\hat{c}(t)$ is $-1 \leq \hat{c}(t) \leq 1$, and $\hat{c}(0) = 1$. If samples are independent, $\hat{c}(t)$ is expected to be 0, whereas $\hat{c}(t) \sim \pm 1$ (for $t > 0$) implies the samples are highly correlated at the lag t. The chain is thinned by using only every τth sample, if the value of τ is large for a given number of samples, implying the samples are highly correlated, we will need to skip more samples than a chain with smaller value of τ for the same number samples. The samples that remain after the burn-in and ACT thinning are called effective samples. The number of effective samples can be used as the termination condition for MCMC rather than the number of iteration, because samples produced with the former condition have no correlation or weak correlation compared to the latter. These effective samples are expected to perform more accurate results than the raw samples when constructing posterior distributions.

The jump proposals in MCMC are the key to efficiently explore the parameter space. A wider proposal compared to the true posterior distribution will cause low acceptance rates and many repeated samples, while the narrower proposal will lead to high acceptance rates and correlated samples. Gaussian jump proposals are usually sufficient for unimodal posteriors without correlations between parameters [36]. However, some parameters for compact binary coalescences are correlated and multimodal, which makes Gaussian jump proposals inefficient. To solve this problem, one have to use different proposals that can capture correlations for different parameters, the detailed discussion of choosing jump proposals for CBC can be found in Ref. [36].

Another technique that can help chains to explore the parameter space efficiently is parallel tempering. The parallel tempering introduces the "temperature" parameter $1/T$

for the likelihood:

$$p_T(d|\vec{\theta}) = p(d|\vec{\theta})^{\frac{1}{T}}. \tag{2.19}$$

When using a low temperature $T \sim 1$ likelihood, MCMC can sample the local parameter space very well, but it might not explore the rest of parameter space well; whereas when using a high temperature $T >> 1$ likelihood, MCMC samples a distribution closer to the prior, and it is more likely to explore the whole range of the space. One can combine the advantages of different tempering by periodically swapping chains between higher and lower temperatures. The swap rate r_s between adjacent chains i and j is given by [36]

$$r_s = \min\left\{1, \left(\frac{p(d|\vec{\theta}_j)}{p(d|\vec{\theta}_i)}\right)^{\frac{1}{T_i}-\frac{1}{T_j}}\right\}, \tag{2.20}$$

where $T_i < T_j$. In practice, we usually run 8 parallel chains with T between 0 and 50 distributed uniformly in logarithm. We only use the samples in the chain with $T = 1$, and discard other chains as they are not drawn from the target posterior. In summary, The parallel tempering together with the various jump proposals that fit parameters for compact binary coalescences can produce robust samples with MCMC drawn from the target posterior.

As mentioned earlier in this section, the evidence $p(d)$ is not calculated during the MCMC sampling process, as it can be calculated during the post-processing if one wants to use the evidence to compare different models. The thermodynamic integration is found to produce reliable estimation of the evidence $p(d)$ from MCMC posterior samples in the post-processing [36]. For MCMC with parallel tempering, the evidence at temperature $T = 1/\beta$ is

$$p(d;\beta) = \int p(d|\vec{\theta})^{\beta} p(\vec{\theta}) d\vec{\theta}, \tag{2.21}$$

Differentiate it with respect to β:

$$\frac{\partial}{\partial\beta}\ln p(d;\beta) = \int \ln(p(d|\vec{\theta}))\frac{p(d|\vec{\theta})^{\beta}p(\vec{\theta})}{\int p(d|\vec{\theta})^{\beta}p(\vec{\theta})d\vec{\theta}}\,d\vec{\theta}$$
$$= \left\langle \ln(p(d|\vec{\theta})) \right\rangle_{\beta}, \tag{2.22}$$

where $\left\langle \ln(p(d|\vec{\theta})) \right\rangle_{\beta}$ is the expectation value of the log likelihood for the chain with the $T = 1/\beta$. The expectation can be directly evaluated with the samples after burn-in in each chain. We can then find the log likelihood by integrating over β:

$$\ln(p(d)) = \int_0^1 \left\langle \ln(p(d|\vec{\theta})) \right\rangle_{\beta} d\beta. \tag{2.23}$$

Eq. (2.23) is a simple 1-dimensional integral, which is easy to evaluate. In summary, the parallel technique not only provides a more robust way to draw samples from the target posterior, the additional chains can also be used to compute the evidence.

2.5.2 Nested sampling

Nested sampling is an algorithm developed by Skilling [53] for computing the Bayesian evidence while drawing samples from posterior. Unlike MCMC that requires extra work to compute the evidence during the post-processing, and that the evidence is an optional by-product, the primary target for Nested sampling is to obtain the evidence that can be achieved by updating the value of evidence at each iteration of sampling.

The straightforward way to compute the evidence $Z = p(d)$ is to evaluate the integral:

$$Z = \int L(\vec{\theta})p(\vec{\theta})d(\vec{\theta}), \tag{2.24}$$

where $L(\vec{\theta}) = p(d|\vec{\theta})$ is the likelihood function. However, this is not practical when the dimension of $\vec{\theta}$ becomes large. Rather than directly evaluate Eq. (2.24), Nested sampling transforms the calculation from the parameter space to the prior volume X. X is defined

by

$$X(\lambda) = \int_{L(\vec{\theta})>\lambda} p(\vec{\theta}) d(\vec{\theta}), \tag{2.25}$$

which computes the prior volume that covers the likelihood greater than λ. Then the evidence calculation becomes a 1-dimensional integral over unit range [53]:

$$Z = \int_0^1 L(X) dX, \tag{2.26}$$

where $L(X)$ is the inverse function of Eq. (2.25), i.e. $L(X(\lambda)) = \lambda$, and $L(X)$ is a monotonically decreasing function of X, since larger prior volume enclosed implies lower likelihood value. Suppose we have a sequence with m points:

$$0 < X_{m-1} < \ddots < X_1 < X_0 < 1, \tag{2.27}$$

The evidence can be estimated with a simple rule:

$$Z = \sum_{i=1}^{m-1} (X_i - X_{i-1}) L_i, \tag{2.28}$$

where $L_i = L(X_i)$. The prior volume X_i can be approximated by $\log X_i \sim -i/N$ [53].

The steps of Nested sampling are summarized here:

1. Initiate N live points from the prior $p(\vec{\theta})$ and set $Z = 0$, $X_0 = 1$.

2. For i in 1,2,...,m:

   - Record the lowest value of likelihood as L_i,
   - Set $X_i = \exp(-i/N)$,
   - Set $w_i = X_{i-1} - X_i$,
   - Increment Z by $w_i L_i$,
   - Store the weight w_i and the point $\vec{\theta}_i$ of the lowest likelihood as a sample,

- Draw a new point $\vec{\theta}$ using MCMC until its likelihood is greater than L_i, and replace the point $\vec{\theta_i}$ of the lowest likelihood with the new point $\vec{\theta}$.

3. Increment Z by $N^{-1}X_j(L(\vec{\theta_1}) + ... + L(\vec{\theta_N}))$.

The last step is to fill the gap $0 < X < X_j$ with weight $N^{-1}X_j$. Instead of using the number of iteration as the termination condition, one can also use this condition [36]

$$L_{max}X_i < fZ_i, \tag{2.29}$$

where L_{max} is the current maximum value of the likelihood, X_i is the prior volume at iteration i, and Z_i is the evidence estimated at iteration i, f is a number close to 1 and it usually choose to be $e^{0.1}$ in LALInference [54] [36]. In other words, this termination condition checks whether the evidence can be increased by a factor f if the remaining prior volume are at the current maximum value of the likelihood.

To obtain the posterior, we need resample the points that are removed and the remaining live points. The probability of selecting a sample is given by [36]

$$p_i = \frac{w_i L_i}{Z} \tag{2.30}$$

Then the equally-weighted posterior samples are obtained by accepting each point as a posterior sample with probability p_i/K, where K is a number that is greater than the maximum value of p. The maximum number of posterior samples N_{max} is given by the entropy [53]

$$N_{max} = \exp(-\sum_i^m p_i \ln p_i). \tag{2.31}$$

Posteriors produced by MCMC and Nested sampling are consistent with each other [36]. Nested sampling has an advantage of obtaining evidence without post-processing, and it is desired if model selection is the main objective of an analysis. An example of the comparison between MCMC and Nested sampling for various parameter posteriors of

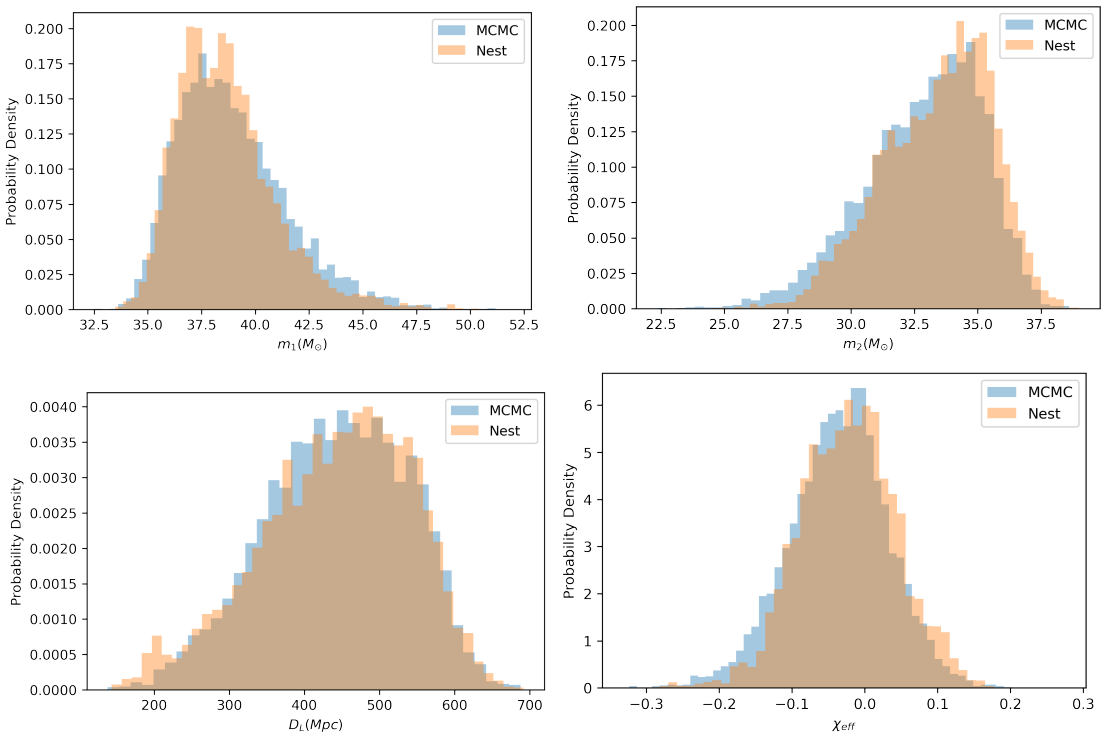

Figure 2.2: Comparison of posterior distributions from MCMC and Nested sampling for GW150914. Top left: posterior distributions of m_1, top right: posterior distributions of m_2, bottom left: posterior distributions of D_L, bottom left: posterior distributions of χ_{eff}.

GW150914 is shown in Figure 2.2.

Chapter 3

Constraining neutron star equation of state

3.1 Introduction

The discovery of first neutron star binary PSR B1913+16 by Hulse and Taylor [12] provided indirect evidence of the existence of gravitational waves. The observation found orbit decay resulting from emitting gravitational waves. On August 17, 2017 a binary neutron star inspiral was observed by Advanced LIGO and Advanced Virgo [14]. This observation of the binary neutron star not only provides the direct detection of gravitational waves emitted from a binary inspiral, it also gives an opportunity to constrain neutron start equation of state (EoS). On April 25, 2019, Advanced LIGO and Advanced Virgo observed a high-mass binary neutron star inspiral GW190425 [19]. These two observations and future BNS observations with GWs are excepted to help understand the internal structure of neutron stars through the equation of state.

The balance between the attractive gravitational force inside a neutron star and the pressure force of neutron-star matter determines internal structure of a neutron star. Neutron stars are cold high-density nuclear matter, which are excepted to have the same equa-

tion of state. While the gravitational field is described by general relativity, the pressure forces caused by nuclear interactions are not fully understood. The current terrestrial laboratories are able to probe densities near or below nucleus density $\rho_{nul} = 2.8 \times 10^{14} g/cm^3$, but unable to probe the extreme matter in the deep core of neutron stars [25]. This difficulty yields a wide range of plausible EoSs derived from theoretical models.

The equation of state prescribes the relation between the pressure and density, which determines the macroscopic properties of a neutron star such as its mass and radius. These parameters can be measured by astrophysical observations, which has the potential to give information about the internal structure of neutron stars. Unlike using the mass and radius from the EM observation, GW relies on measuring the tidal deformablity of neutron stars and their masses in order to constrain the equation of state. The measurement can be used to rule out certain EoSs that are significantly different from the posterior of tidal deformablity.

3.2 Mass-radius relation of neutron stars

The equation of state of neutron stars is usually given by the microscopic pressure(P)-density(ρ) relation

$$P = P(\rho). \tag{3.1}$$

This relation can also be written as $P = P(\epsilon)$, where ϵ is the energy density. The macroscopic properties of neutron stars is connected to the EoS by solving the Tolman-Oppenheimer-Volkoff (TOV) equations [55, 56, 57]

$$\frac{dP}{dr} = -G(\rho + \frac{P}{c^2})\frac{m(r) + 4\pi r^3 P/c^2}{r(r - 2Gm(r)/c^2)}, \tag{3.2}$$

$$\frac{dm(r)}{dr} = 4\pi r^2 \rho(r), \tag{3.3}$$

where ρ is the density, r is the radius, and $m(r)$ is mass within the radius r. The TOV equations are the relativistic case of the Newtonian hydrostatic equation. The TOV equations are solved as an initial value problem when the EoS Eq. (3.1) is specified [58]. Given the initial conditions (center pressure P_c and $m = 0$) at the center ($r = 0$) of a neutron star, we can integrate the Eq. (3.2, 3.3) outward until reach the surface of the neutron star where the pressure vanishes. Then the radius (R) of the neutron star is determined by $P(R) = 0$, and the mass (M) of the neutron star is determined by $M = m(R)$. Thus, for a given EoS, the mass-radius (M-R) relation is determined by integrating solving the TOV equations. In other words, this process can be viewed as a map from a curve in $P - \rho$ plane to a curve in $M - R$ plane [58].

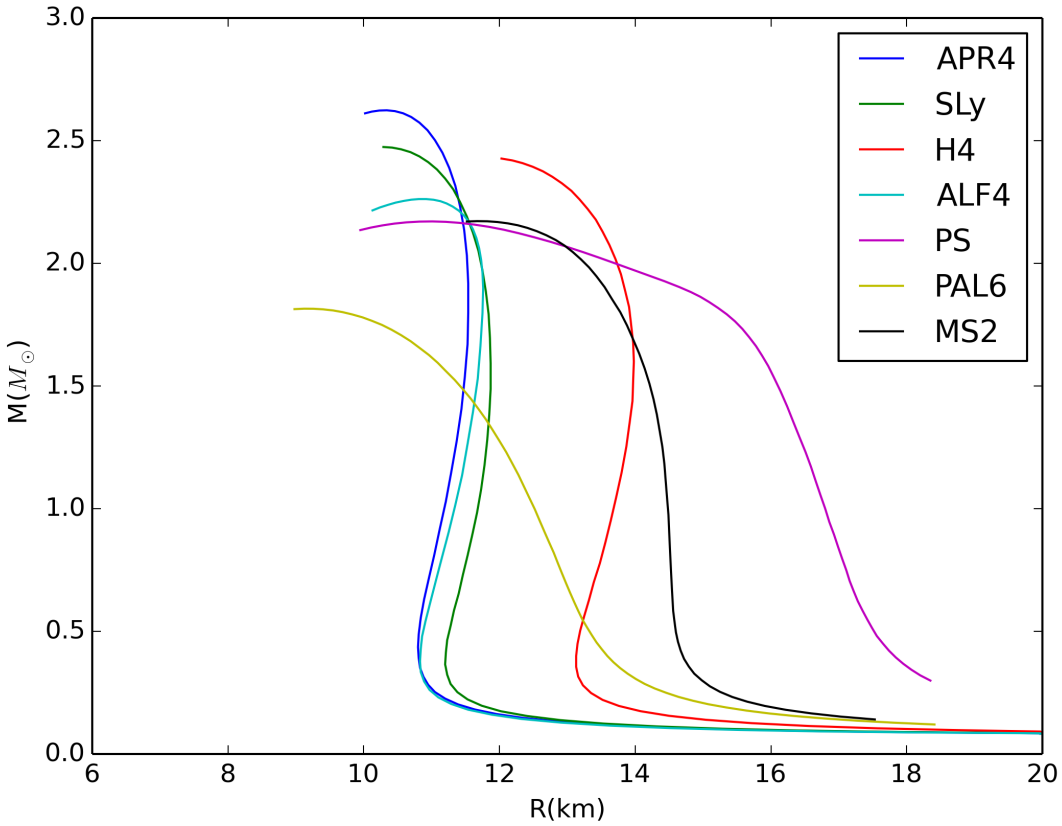

Figure 3.1: Mass-radius relations for seven different parametrized equation of states. These curves are obtained by numerically solving the TOV equations.

The solutions of the TOV equations provide the map between the EoS and the mass-radius (M-R) relation of neutron stars. By inverting this map, one can infer the EoS [58]. This requires to measure the entire M-R curve, however, the EM observations have only observed neutron stars with masses $\sim 1-2\ M_{\odot}$ [59] and EM observations of R are quite uncertain, which is insufficient to imply the EoS.

A study conducted by Read et al. [60] shows the EoS can be represented by piecewise polytropes with only a few parameters. This provides an opportunity to infer the internal structure of neutron stars with only a small number of observations. The pressure-density relation of neutron stars can be parametrized by piecewise polytropic EoS with 4-parameter [60]. The polytropic EoS has the form

$$P(\rho) = K\rho^{\Gamma}, \tag{3.4}$$

where Γ is the adiabatic index. Figure 3.1 shows the M-R relations for different parametrized piecewise polytropic EoSs by numerically solving the TOV equations. The values of the parameters for the EoSs are from Ref. [60].

The maximum mass of neutron stars can also be used to rule out certain EoSs that do not support such mass. These observations relies on measuring masses of pulsars and X-ray binaries, the detailed discussion can be found in Ref. [59, 61, 62].

3.3 Tidal deformability

Gravitational-wave observations of binary neutron stars provide an alternative means to constrain EoS. Other than directly measuring the radii of a binary neutron star, another intrinsic parameter that can be measured during the inspiral is the tidal deformability. When a binary neutron star system at the late stage of the inspiral, a neutron will be deformed by the tidal field $\mathcal{E}_{ij}$ that is produced by its companion. The neutron star will have non-vanishing quadrupole moment Q_{ij}, which is related to the tidal field in the linear

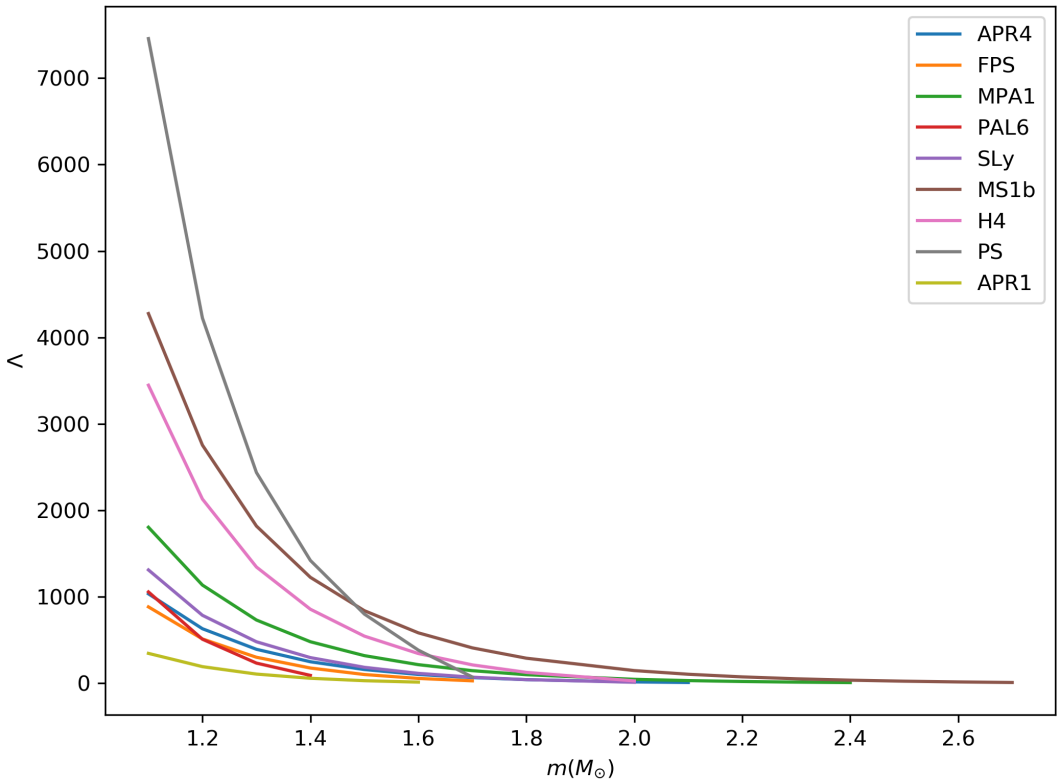

Figure 3.2: Dimensionless tidal deformability as a function of mass for for a variety of EoSs.

order [63] :

$$\mathcal{E}_{ij} = -\lambda Q_{ij}, \tag{3.5}$$

where λ is called tidal deformability, and it can be written in terms of dimensionless Love number k_2 [63]:

$$\lambda = \frac{2}{3} k_2 \frac{R^5}{G}. \tag{3.6}$$

For black holes k_2 is excepted to be 0 [14]. It is common to use the dimensionless tidal deformability Λ in GW data analysis; Λ is given by [64]

$$\Lambda = G\lambda \left(\frac{c^2}{Gm}\right)^5 = \frac{2}{3} k_2 \left(\frac{Rc^2}{Gm}\right)^5. \tag{3.7}$$

For a given EoS (k_2 is a constant), $\Lambda \sim (R/m)^5$, which can be used to indicate the compactness (M/R) of the neutron star. Also, for a fixed mass, a neutron star with a stiff EoS will have a large radius and a large value of Λ; a neutron star with a soft EoS will have a small radius and a small value of Λ. Λ can be viewed as a function of mass and EoS: $\Lambda = \Lambda(m, \text{EoS})$, Figure 3.2 shows the relation between Λ and m for a variety of EoSs. Thus, by measuring Λ and m through gravitational waves, we can imply the information about the underlying EoS.

The currently known tidal terms enter the waveforms at 5PN and up to 7.5PN [64, 47]. Here, we only consider the linear equilibrium tide, the studies of the dynamical tide can be found in Ref. [65] and the nonlinear tide can be found in Ref. [66]. The individual tidal parameters Λ_1 and Λ_2 can be transformed into $\tilde{\Lambda}$ and $\delta\tilde{\Lambda}$, where

$$\tilde{\Lambda} = \frac{8}{13}\left[(1+7\eta-31\eta^2)(\Lambda_1+\Lambda_2) + \sqrt{1-4\eta}\,(1+9\eta-11\eta^2)(\Lambda_1-\Lambda_2)\right] \tag{3.8}$$

$$\begin{aligned}\delta\tilde{\Lambda} = \frac{1}{2}\Bigg[&\sqrt{1-4\eta}\left(1-\frac{13272}{1319}\eta+\frac{8944}{1319}\eta^2\right)(\Lambda_1+\Lambda_2)+\\ &\left(1-\frac{15910}{1319}\eta+\frac{32850}{1319}\eta^2+\frac{3380}{1319}\eta^3\right)(\Lambda_1-\Lambda_2)\Bigg]\end{aligned} \tag{3.9}$$

The 5PN and 6PN tidal corrections to the phase are given by [64]

$$\delta\phi_{tidal} = \frac{3}{128\eta x^{5/2}}\left[\left(-\frac{39}{2}\tilde{\Lambda}\right)x^5 + \left(-\frac{3115}{64}\tilde{\Lambda}+\frac{6595}{364}\sqrt{1-4\eta}\delta\tilde{\Lambda}\right)x^6\right] \tag{3.10}$$

The tidal corrections in the 5PN only contain $\tilde{\Lambda}$, 6PN terms consist of both $\tilde{\Lambda}$ and $\delta\tilde{\Lambda}$. This makes $\tilde{\Lambda}$ much easier to measure than $\delta\tilde{\Lambda}$ as the coefficient of $\delta\tilde{\Lambda}$ is much less than the coefficient of $\tilde{\Lambda}$ in the 6PN.

Figure 3.3 shows posterior distributions of tidal parameters for GW170817. The parameter estimation runs incorporates a low-spin prior and a high-spin runs with the dimensionless component spin magnitudes $\chi < 0.05$ and $\chi < 0.89$, respectively. The low-spin prior is

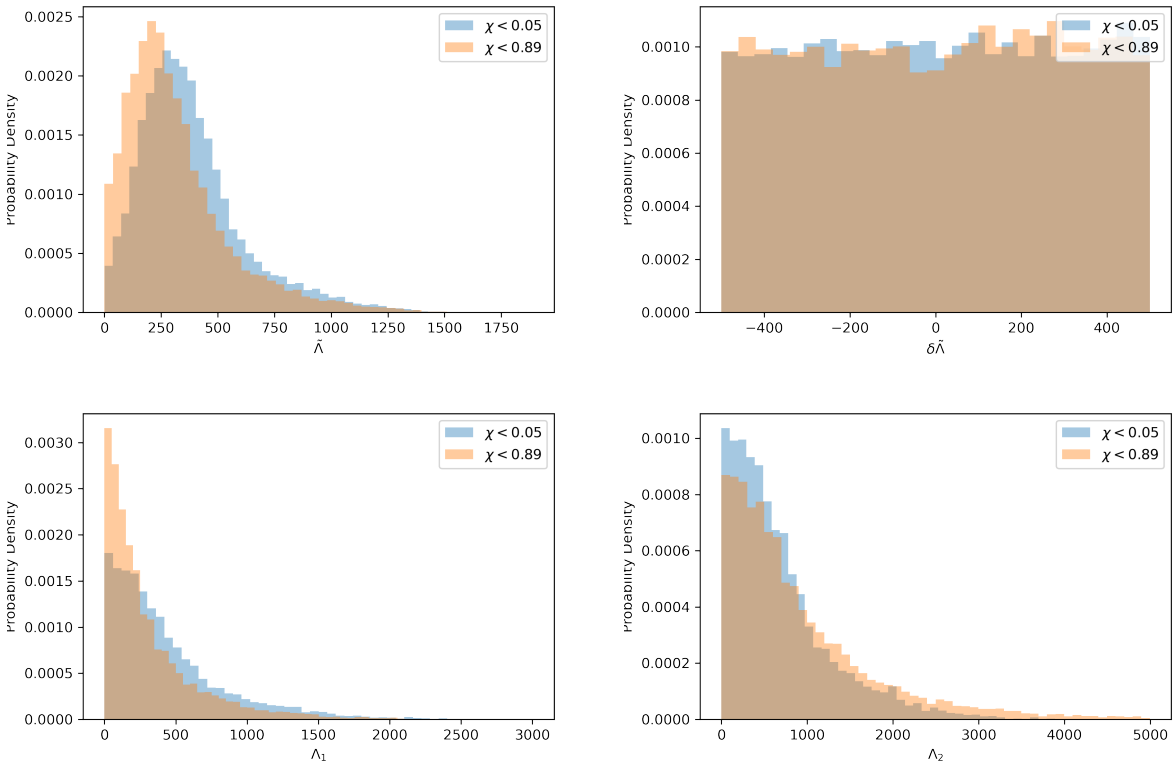

Figure 3.3: Posterior distributions of tidal parameters for GW170817 $\tilde{\Lambda}$ (top left), $\delta\tilde{\Lambda}$ (top right), Λ_1 (bottom left), and Λ_2 (bottom right). Each figure includes a low-spin prior ($\chi < 0.05$) and a high-spin prior ($\chi < 0.89$). The waveform used in this analysis is TaylorF2.

consistent with the observation where the fastest spin neutron star has $\chi < 0.04$ [34]; the high-spin prior is the maximum value of a neutron that is allowed by waveforms [14]. The top two plots for $\tilde{\Lambda}$ and $\delta\tilde{\Lambda}$ are obtained with the uniform prior on $\tilde{\Lambda}$ and $\delta\tilde{\Lambda}$, whereas the bottom two plots for Λ_1 and Λ_2 are obtained with the uniform prior on Λ_1 and Λ_2. As we can see from Figure 3.3, the $\delta\tilde{\Lambda}$ is not measurable under the current sensitivity of Advanced LIGO and Advanced Virgo. On the other hand, if one converts the $\delta\tilde{\Lambda}$ posteriors from the runs with uniform in Λ_1 and Λ_2, it will exhibit non-uniform distribution as opposed to the uniform distribution shown in Figure 3.3. This is because prior that is uniform in Λ_1 and Λ_2 is not uniform in $\delta\tilde{\Lambda}$, and since $\delta\tilde{\Lambda}$ is not measurable under the current sensitivity, the posterior distribution of $\delta\tilde{\Lambda}$ is essentially its prior distribution.

Figure 3.4 shows the posterior distributions of tidal parameters ($\tilde{\Lambda}$, $\delta\tilde{\Lambda}$, Λ_1, and Λ_2) for

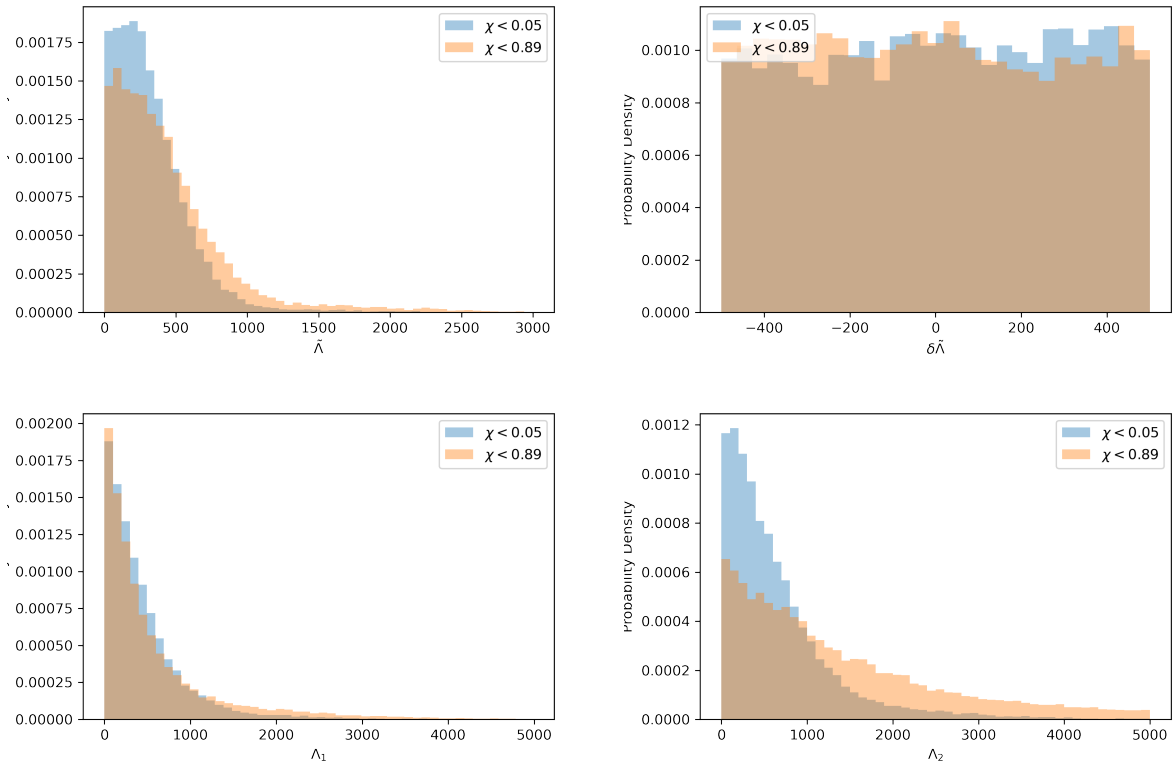

Figure 3.4: Posterior distributions of tidal parameters for GW190425. $\tilde{\Lambda}$ (top left), $\delta\tilde{\Lambda}$ (top right), Λ_1 (bottom left), and Λ_2 (bottom right). Each figure includes a low-spin prior ($\chi < 0.05$) and a high-spin prior ($\chi < 0.89$). The waveform used in this analysis is TaylorF2.

GW190425. The posteriors of GW190425 are not constrained as well as GW170817, this is because GW190425 is a high-mass BNS event with total mass ~ 3.4 [19], which makes $\tilde{\Lambda}$ close to 0. Moreover, the signal of GW190425 is much weaker than GW170817 due to the fact that the source was located much distant $\sim$ 160Mpc compared to GW170817 ($\sim$ 40Mpc). Lastly, the Hanford detector was temporarily offline when the signal arrived, and only Livingston detector and Virgo detector were taking data. The above facts make the tidal deformability poorly measured, as a result, 0 tidal deformability is not excluded in its 90% credible interval. Thus, we cannot rule out from the posterior of $\tilde{\Lambda}$ that one or two components were black holes.

The low-spin and high-low prior has little influence on $\tilde{\Lambda}$. However, as we can see from Figure 3.5, component masses m_1 and m_2 are changed significantly for two spin priors.

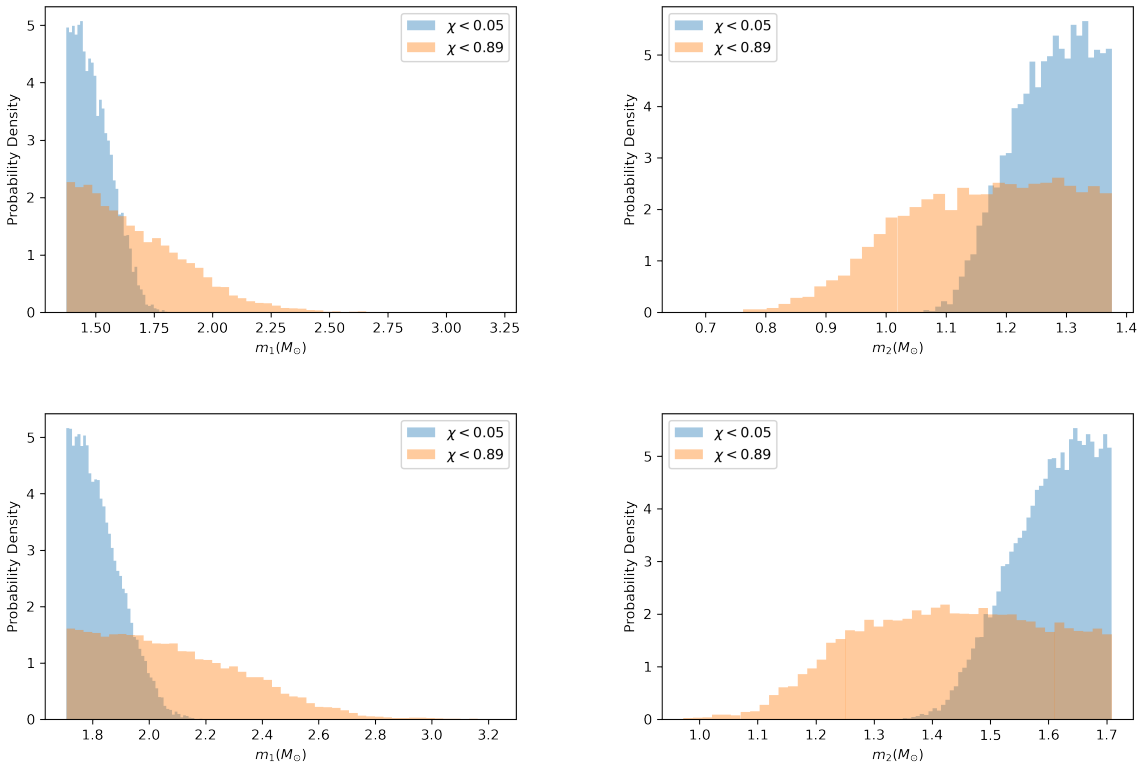

Figure 3.5: Posterior distributions of component mass for GW170817 (top) and GW190425 (bottom). Each figure includes a low-spin prior ($\chi < 0.05$) and a high-spin prior ($\chi < 0.89$). The waveform used in this analysis is TaylorF2.

The correlation between the mass ratio q and effective spin χ_{eff} makes the m_1 and m_2 distributions much wider for the high-spin prior than the low-spin prior.

3.4 Equation of state model selection

Given a set of proposed neutron star EoSs, we can rule out certain EoSs based on the observing data. The standard way to perform such model selection is to compute Bayesian evidence for each model, and then compare those values. If the evidence of model M_1 is much less than the evidence of model M_2 ($Z(M_1) << Z(M_2)$), then the M_2 is more likely to be the true model given the data. The results for GW170817 are presented in Ref. [26], where the evidence of each EoS model was carrying out with Nested sampling.

However, this method requires many individual parameter estimation runs in order to obtain evidences of proposed models. Here, we present two alternative methods which significant reduce the computational costs.

3.4.1 Evidence approximation [1]

The evidence approximation method presented here is a technique that is designed to help investigations of large number of models of equation of state of neutron stars. The crucial element of this technique is that one only needs a single instance of EoS agnostic parameter estimation run conducted with appropriate priors. The approximate Bayes factor between any two arbitrary models can then be computed very rapidly thereafter.

To compute the evidence, one need to carry out the high dimension integral

$$Z = \int p(d|\vec{\theta})p(\vec{\theta})d(\vec{\theta}). \tag{3.11}$$

EoSs are not expected to affect extrinsic parameters as they enters the waveform only through tidal parameters, which are also depend on masses. We can marginalize over other parameter in Eq. (3.11) except for M_c, q, $\tilde{\Lambda}$ and $\delta\tilde{\Lambda}$. The factor that has been integrated out should be approximately equal across EoSs, which we no longer need to consider in the model selection. Thus, we can simplify the integral in Eq. (3.11):

$$Z \propto \int p(d|M_c, q, \tilde{\Lambda}(M_c, q; \mathrm{EoS}), \delta\tilde{\Lambda}(M_c, q; \mathrm{EoS}))p(M_c, q)dM_c dq. \tag{3.12}$$

We can express the EoS constraints as delta-functions, Eq. (3.12) becomes

$$Z \propto \int p(d|M_c, q, \tilde{\Lambda}', \delta\tilde{\Lambda}')\delta(\tilde{\Lambda}' - \tilde{\Lambda}(M_c, q; \mathrm{EoS}))\delta(\delta\tilde{\Lambda}' - \delta\tilde{\Lambda}(M_c, q; \mathrm{EoS}))p(M_c, q)dM_c dq d\tilde{\Lambda}' d\delta\tilde{\Lambda}'. \tag{3.13}$$

Since the chirp mass is well constrained, we can approximate it as a constant M_0, which

[1] This section is based on Ref [67]

can be chosen to be the mean value of the posterior. Applying Bayes' theorem, we can approximate the product of the likelihood and prior in terms of posterior:

$$\begin{aligned} p(d|M_c, q, \tilde{\Lambda}, \delta\tilde{\Lambda})p(M_c, q) &\propto p(M_c, q, \tilde{\Lambda}, \delta\tilde{\Lambda})|d) \\ &\propto p(q, \tilde{\Lambda}|d)\delta(M_c - M_0), \end{aligned} \tag{3.14}$$

where we impose a uniform prior on $\tilde{\Lambda}$ and $\delta\tilde{\Lambda}$ and assume the above calculation is independent of $\delta\tilde{\Lambda}$ as it is not measurable under the current sensitive. Then Eq. (3.13) can be simplified as

$$Z \propto \int p(q, \tilde{\Lambda}(M_0, q; \mathrm{EoS})|d)dq. \tag{3.15}$$

Therefore, the high dimensional integral of the evidence is reduced to a one-dimensional integral that is evaluated over the two-dimensional posterior distribution $p(q, \tilde{\Lambda}|d)$ along the curve: $q \to \tilde{\Lambda}(M_0, q; \mathrm{EoS})$ determined by measured chirp mass M_0 and the EoS.

The evidence approximation scheme of estimating the evidence of an EoS is summarized as follows:

1. We first conduct a parameter estimation run with MCMC or Nested sampling in which $\tilde{\Lambda}$ is a free parameter to obtain the two-dimensional posterior distribution of q and $\tilde{\Lambda}$ for a BNS event.

2. Nest, we construct a kernel density estimation (KDE) to represent the two-dimensional distribution obtained in the previous step.

3. Lastly, we perform the one-dimensional integral (Eq. 3.13) in which the probability $p(q, \tilde{\Lambda})$ is approximate by the KDE to estimate the evidence for an EoS.

We can repeat the step 3 to compute evidences for other EoSs. Figure 3.6 shows the EoS lines in the two-dimension posterior of $(\tilde{\Lambda}, q)$ for GW170817, the low-spin prior and high-spin prior are shown in the left plot and the right plot, respectively. EoS lines that are close to the higher density region are expected to have higher values of the evidence.

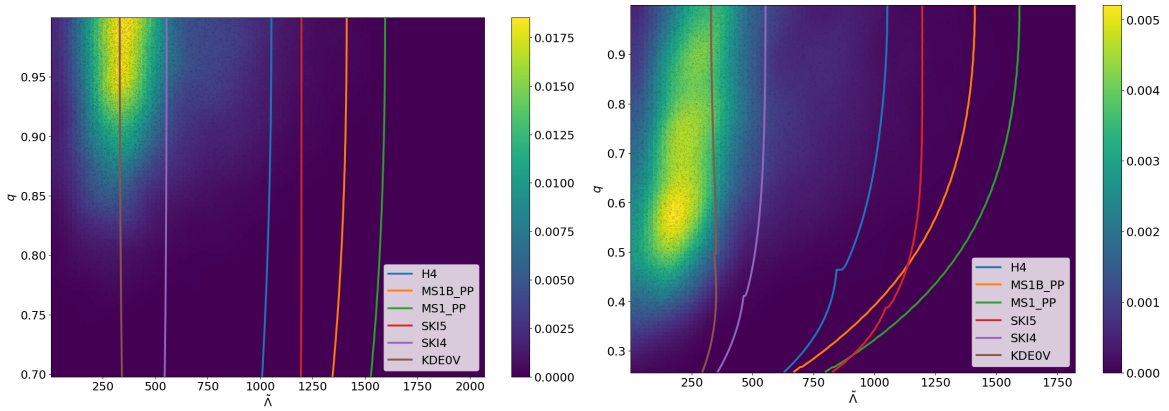

Figure 3.6: Left: Posterior distribution in $(\tilde{\Lambda}, q)$ for the low-spin prior and its KDE. For comparison we show the EoS curves for various models in $(\tilde{\Lambda}, q)$. Note that the models that gave the highest deviation with respect to (w.r.t) the nested sampling results in Ref [26] are also the most distant from the peak of the posterior distribution. Thus we can conclude that the error in the Bayes-factor computation for some of EoSs is due to the small number of samples in the parameter space through which the EoS line passes. Right: Same comparison for the high-spin prior case. We again show the EoS curves for various models in $(\tilde{\Lambda}, q)$. We see the identical relationship that for the EoSs that gave the largest deviation in the Bayes-factor computation w.r.t the nested sampling results, the posterior support is the weakest. Note that the kinks in the various EoSs in this plot are due to the fact that it extends to smaller values of q, where one of the object in the binary becomes more massive than the maximum allowed neutron star mass. At this point we consider that object a black hole and set the value of $\lambda_1 = 0$. This leads to a sudden change in the value of $\tilde{\Lambda}$ and hence creates these kinks.

This evidence approximation scheme gives us an opportunity to perform model selection without running Nested sampling for each individual EoS model. Rather, we only need to do a single parameter estimation run to obtain the posteriors, after which the evidences can be computed in a very short time ($\sim$ minutes). Thus, the computational cost of the evidence approximation is significantly reduced compared to the method presented in Ref [26]. The comparison of the two methods for GW170817 is shown in Figure 3.7, where the uncertainty of the evidence approximation method is computed with bootstrapping.

The waveform adopted in this analysis is TaylorF2, which is a post-Newtonian non-precessing frequency domain waveform that includes tidal effects. The waveform is terminate at ISCO [64] and the choice of the termination frequency has negligible effect on the results since even for the most massive samples this termination frequency is safely

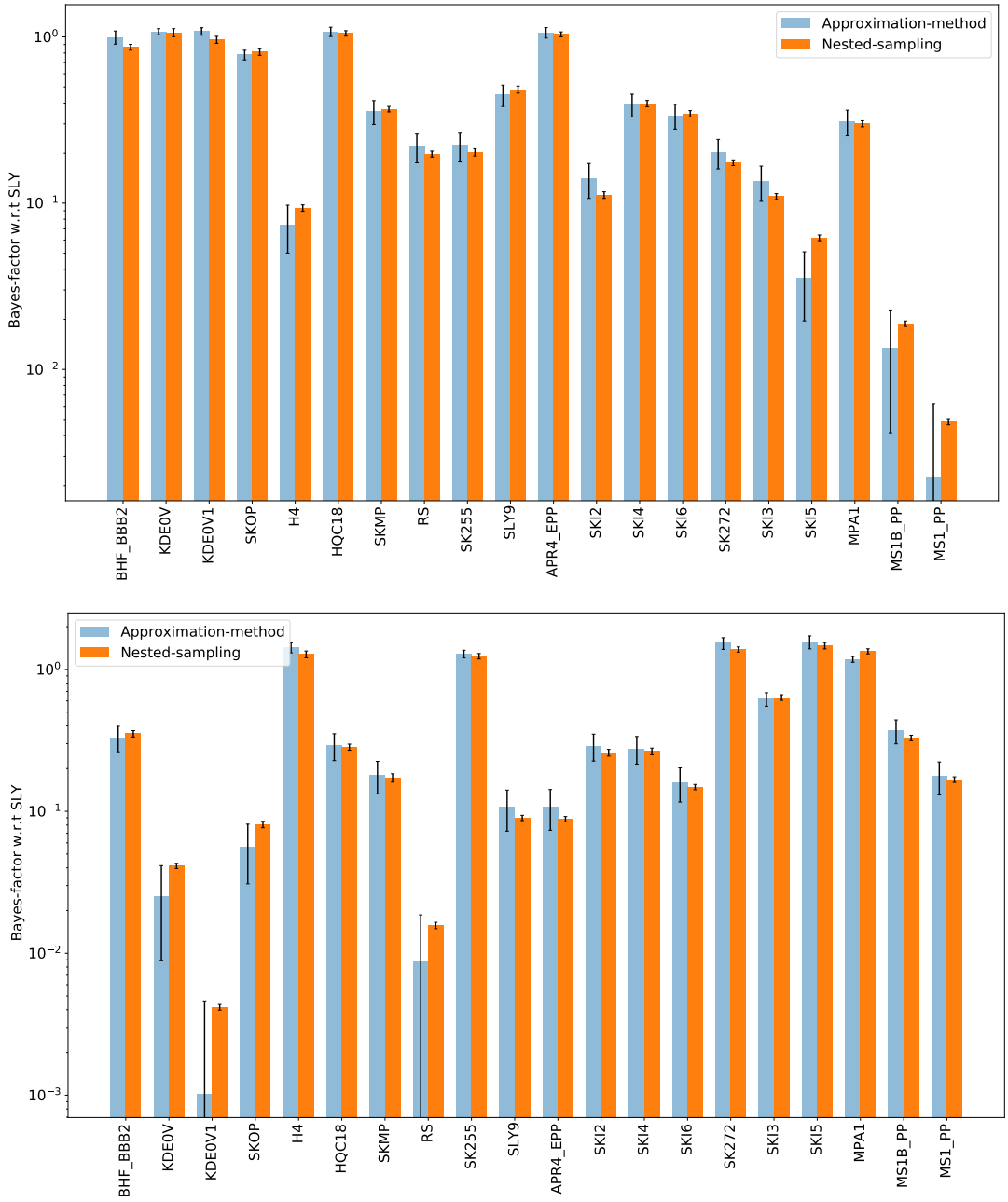

Figure 3.7: Comparison of Bayes factors obtained with our approximate Bayes-factor calculation scheme and the `LALINFERENCE_NEST` nested sampling results [26], shown here for the low-spin prior in the top panel and the high-spin prior in the bottom panel. The Bayes factors are computed w.r.t the "SLY" model in both cases. We show here results for the TaylorF2 waveform. The error bars in the Bayes factor for the approximation method are obtained by computing the standard deviation of the Bayes factors after resampling the posterior distribution repeatedly (ten thousand times). We further multiply the uncertainty by a factor of 2 (obtained from simulation studies) to accommodate biases in the computation of the Bayes factor introduced through resampling.

outside the sensitivity window of the detectors. The choice of low frequency cutoff usually depends on the sensitivity of the detectors. For GW170817 the low frequency cutoff is 23Hz [26], and we reduce the the low frequency cutoff of GW190425 to 19.4Hz [19], due to the improvement of the sensitivity.

The priors for mass and spin that we used for GW170817 are consistent with the priors presented in Ref. [26], specifically, we consider narrow and broad priors on masses and spins. Our choice of the narrow prior is based on binary neutron stars (BNS) observed in our galaxy, and we assume component masses of BNS follows a Gaussian distribution with mean 1.33 $M_\odot$ and standard deviation 0.09 $M_\odot$ [59], we also impose a constraint $m_2 \leq m_1$. Since the fastest observed spinning neutron star has dimensionless spin magnitude $\chi \sim 0.04$ [34], we impose a uniform prior on χ between 0 and 0.05. For the broad prior, the masses are uniformly distributed between 0.7 $M_\odot$ and 3.0 $M_\odot$. The prior on χ in this case is uniformly distributed between 0 and 0.7. Though it is narrower than the one adopted in Ref. [14], the results should not be affected as the 95% confidence interval of $\chi < 0.4$. For GW190425, a high-mass BNS with total mass $\sim 3.4 M_\odot$ and chirp mass $\sim 1.44 M_\odot$ [19], we put uniform prior on masses for both narrow and broad PE runs, because the masses are significant larger than those observed in our galaxy. We use the same spin priors that presented in Ref. [19], i.e. the dimensionless spin magnitude are uniformly distributed for low-spin $\chi < 0.05$ and high-spin $\chi < 0.89$.

The results produced from the evidence approximation scheme are generally in good agreement with those produced using the nested sampling method. Note, however, that the Bayes factors obtained within the approximation scheme have large fractional errors for equations of state predicting low evidences. This is due to the intrinsically poor sampling in the regions of parameter space that are least likely a posteriori. For example, the number of samples produced at very large tidal deformabilities will be dwarfed by the number of samples produced at more modest tidal deformabilities, where softer equations of state are most preferred by the gravitational-wave data. This is why we provide the Bayes factors

with respect to the SLY EoS as reference model for which the standard deviation of the evidence computation using the approximation method was relatively small, thus reducing the reference model contribution to the Bayes factor residuals.

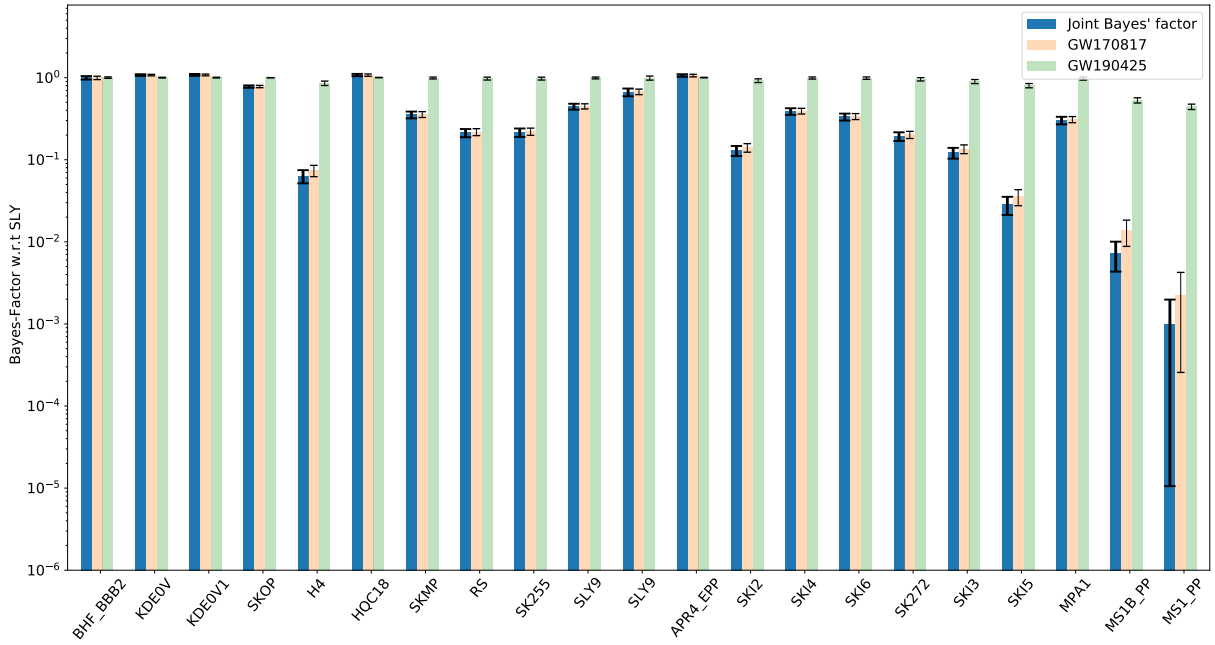

Figure 3.8: Bayes-factor of various EoSs w.r.t SLY model for GW170817, GW190425, and their combination by evidence-stacking. Note that the blue bars (joint Bayes-factor) and the orange bars (Bayes-factor from GW170817 data) are very similar to each other indicating that most of the information in discerning between the different models comes from the data of GW170817. The green bars for GW190425 are adding very little information as can also be seen from the fact that their variation in height across the various model is very small.

We have presented the evidence approximation method for a single BNS event, this method can also be extended to N BNS events. This is achieved by multiply the evidence of each event:

$$Z^E = \prod_{i=1}^{N} Z_i^E, \tag{3.16}$$

where Z_i^E is the evidence of EoS for event i, and Z^E is the stacked evidence for EoS. The Bayes factor for N BNS events between EoS E_1 and EoS E_2 is simply the ratio of the stacked evidence

$$B_{E_2}^{E_1} = \frac{Z^{E_1}}{Z^{E_2}}. \tag{3.17}$$

What makes GW190425 especially interesting is that the heavier object in the binary is estimated to be around $1.60\,M_{\odot}$ to $2.52\,M_{\odot}$ (if we apply a broad spin prior of the object as mentioned in this work) [19]. The upper-limit of the mass of this object is at the edge of maximum neutron star mass of some EoS models. Unfortunately, the luminosity distance of this event is $\sim$ 4 times greater than the luminosity distance of GW170817. Thus, the strength of the gravitational wave from this event is much weaker across the entire frequency band. This reduction in the signal strength, especially in the high frequency regime, severely affects our ability to infer on the tidal deformability and hence the neutron star EoS. Thus, we do not expect a very large effect of including the data from GW190425 in the computation of the Bayes factor between the various EoSs. The posterior samples from this run were then used to compute the Bayes factors against the SLY EoS using the approximation method. We then combine the Bayes factors for the various models with respect to SLY with the same computed for GW170817 using the method of evidence-stacking method. Figure 3.8 The figure shows the stacked Bayes factors of GW170817 and GW190425 with respect to SLY, as well as the individual Bayes factors, and the figure only shows the runs with the low-spin prior. However, due to the weaker signal of GW190425 compared to GW170817, the sacked evidences are not changed very much in comparison of the evidences for GW170817.

3.4.2 Evidence sampling

The evidence of given an EoS model M can be written as $p(d|M)$, apply Bayes theorem:

$$p(d|M) = \frac{p(d)p(M|d)}{p(M)}. \tag{3.18}$$

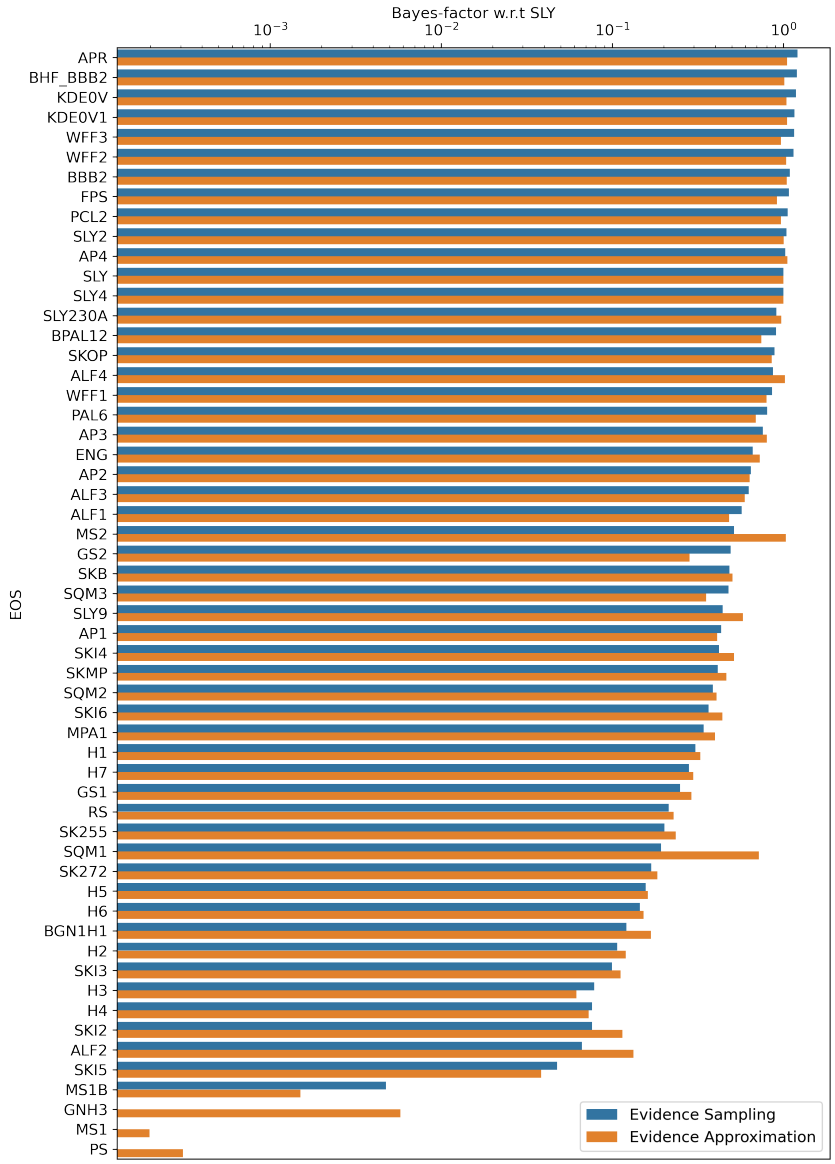

Figure 3.9: The figure shows the Bayes factors of GW170817 computed with the evidence sampling method and the the evidence approximation method. The Bayes factor are with respect to "SLY", and the figure only shows the runs with the low-spin prior.

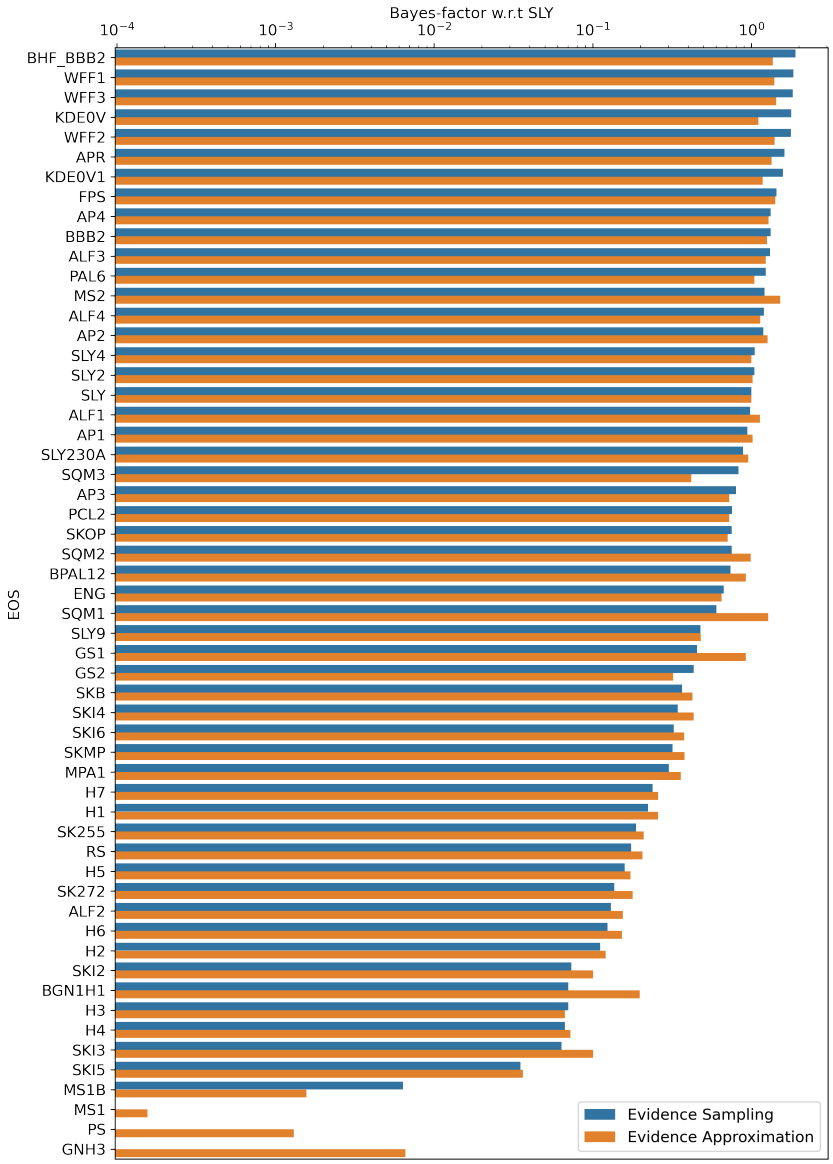

Figure 3.10: The figure shows the Bayes factors of GW170817 computed with the evidence sampling method and the the evidence approximation method. The Bayes factor are with respect to "SLY", and the figure only shows the runs with the high-spin prioror

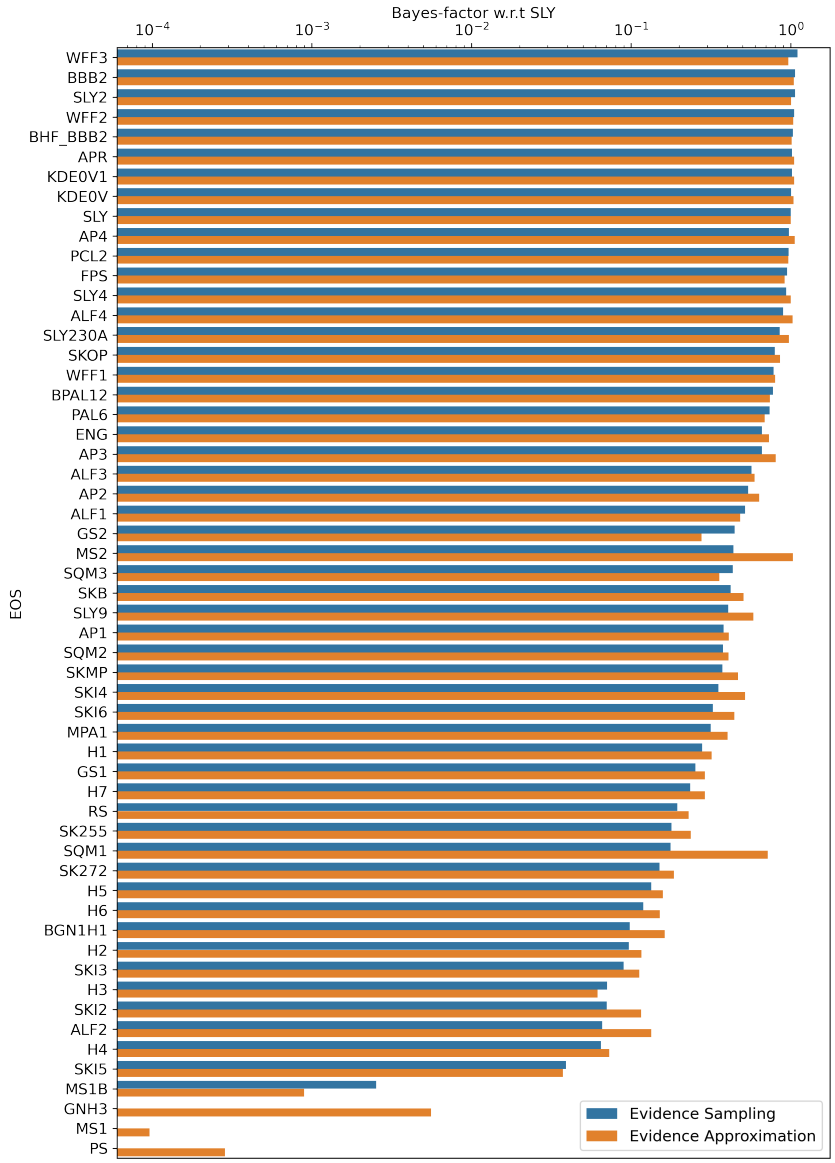

Figure 3.11: The figure shows the stacked Bayes factors of GW170817 and GW190425 computed with the evidence sampling method and the the evidence approximation method. The Bayes factor are with respect to "SLY", and the figure only shows the runs with the low-spin prior.

If we assume each EoS model is equally likely, i.e., $p(M)$ is a constant, then the Bayes factor between M_1 and M_2 becomes

$$B^{M_1}_{M_2} = \frac{p(d|M_1)}{p(d|M_2)} = \frac{p(M_1|d)}{p(M_2|d)}. \tag{3.19}$$

Thus, we can treat M as a random parameter along with other gravitational-wave signal parameters $\vec{\theta}$. We achieve this by mapping an EoS to an integer between 1 and k, where k is the total number of EoSs in the analysis. During a parameter estimation run with MCMC or Nested sampling, a random EoS is proposed, and the EoS is used to calculate $\tilde{\Lambda}$ and $\delta\tilde{\Lambda}$ with the proposed masses. These parameters then are used to generate a waveform in order to compute the likelihood. After the random sampling terminates, we can obtain the marginalized posterior of M by marginalizing over other parameters $\vec{\theta}$:

$$p(M|d) = \int p(M, \vec{\theta}|d) d\vec{\theta}. \tag{3.20}$$

The Bayes factor of any two EoSs is simply the ratio of the number of samples of the two EoSs.

Similar to the evidence approximation method, this evidence can be combined to apply to a case of N BNS events. The evidence of an EoS model M under N BNS signals $d_1, d_2, ..., d_N$ is

$$p(d_1, d_2, ..., d_N|M) = p(d_1|M)p(d_2|M)...p(d_N|M), \tag{3.21}$$

here, we assume the N events are mutually independent. The Bayes factor for N events is the product of Bayes factor for each individual event:

$$B^{M_1}_{M_2} = \frac{p(d_1, d_2, ..., d_N|M_1)}{p(d_1, d_2, ..., d_N|M_2)} = \prod_{i=1}^{N} \frac{p(M_1|d_i)}{p(M_2|d_i)}. \tag{3.22}$$

Figure 3.9 and Figure 3.10 show the Bayes factors of GW170817 computed with the evidence sampling method with low-spin and high-spin priors. The Bayes factors are with

respect to "SLY", and the Bayes factors are generally in agreement with Bayes factors computed with the evidence approximation. Figure 3.9 shows the stacked the Bayes factors of GW170817 and GW190425 of the two method with the low-spin prior. Due to the weaker signal and the higher masses of GW190425, the amount of Bayes factors of GW190425 contributing to the stacked Bayes factors are much less than GW170817. Again, the Bayes factors produced by the evidence sampling method and the evidence approximation method are generally in agreement with each other.

3.5 Discussion and conclusions

We need to mention that the two alternative methods presented in this chapter usually have lager statistical uncertainties compared to the direct estimation of the evidence using Nested sampling in Ref. [26]. The evidence approximation method relies on construct KDE to compute the integral, in a parameter space where only a few samples are available, then the evidence computation can have large statistical fluctuations such as extremely soft models are used in the case of GW170817. Similarly, the evidence sampling also require to have reasonable samples to be able to accurately represent the evidence, and the total number of samples should increase as the number of EoSs included in the analysis increases.

The evidence approximation method and the evidence sampling method presented in this chapter provided alternative means of computing evidence for the EoS model selection. The biggest advantage of the two methods is the computational efficiency, namely, we only need to perform a single parameter estimation run for each BNS event, and post-processing time is negligible compared to the parameter estimation run. The accuracy of the method is reasonably good and continues to perform well with stacking multiple events. These methods can be very useful in the future if many BNSs need to be analyzed. Moreover, from the results of the evidence approximation method and the evidence sampling method, we find these two method provide robust and accurate estimation of evidence when compares to

the evidence directly outputted from Nested sampling presented in Ref [26]. This agreement not only gives us confidence on the validity of the two alternative methods, it also suggests one can perform a such EoS model selection on a larger number of EoSs with only a single PE run. Finally, the values of the Bayes factor for GW170817, GW190425, and the stacked suggest the stiff EoSs are disfavored. On the other hand, there is no specific soft EoS model that is favored by the GW data, suggesting the GW observations so far are insufficient to determine the underlying EoS.

Chapter 4

Measuring the speed of gravitational waves from the first and second observing run of Advanced LIGO and Advanced Virgo [1]

4.1 Introduction

The first gravitational wave (GW) detection, GW150914 [69], was observed from a binary black hole (BBH) merger during the first observing run (O1) of Advanced LIGO [6] from September 12th, 2015 to January 19th, 2016. Later in O1, two BBH mergers GW151012 [70] and GW151226 [71] were also detected by the two Advanced LIGO detectors. The second observing run (O2) of the Advanced LIGO took place from November 30th, 2016 to August 25th, 2017. In O2 three BBH mergers GW170104 [72], GW170608 [73] and GW170823 [8] were detected by the two Advanced LIGO detectors. With the Advanced Virgo [10] detector joining in later O2, four more BBH mergers GW170729 [8], GW170809

[1] This chapter is based on Ref [68]

[8], GW170814 [74] , GW170818 [8] and one binary neutron star (BNS) inspiral GW170817 [14] were observed by the three-detector network [11].

General Relativity predicts that the speed of gravitational waves is equal to the speed of light in a vacuum. The GW seen by the Advanced LIGO and Advanced Virgo detectors can be used to test the theory of general relativity. The first measurement of the speed of gravitational waves using time delay among the GW detectors was suggested by Cornish *et al* [75]. By applying the Bayesian method the speed of gravitational waves is constrained to 90% confidence interval between $0.55c$ and $1.42c$ with GW150914, GW151226 and GW170104 [75].

Subsequent to Cornish *et al* [75], a more precise measurement of the speed of gravitational waves was facilitated by the measurement of the time delay between GW and electromagnetic observations of the same astrophysical source. On August 17, 2017, a binary neutron star inspiral GW170817 was observed by the Advanced LIGO and Advanced Virgo detectors, (1.74 ± 0.05)s later the Gamma-ray burst(GRB) was observed independently by Fermi Gamma-ray Laboratory. By using the lower bound of luminosity distance obtained from the GW signal, the time delay between the GW and GRB, and some astrophysical assumptions, the speed of gravitational waves(v_g) was constrained to $-3 \times 10^{-15}c < v_g - c < +7 \times 10^{-16}c$ [76].

Using the time delay between GW and GRB requires assuming the time difference of emission of the gamma rays relative to the peak of the gravitational waveform. For extreme models, this difference could be $\sim 1000s$ [77, 78] , which is much larger than the $10s$ lag adopted in Ref. [76], and emission of the gamma rays could even lead the merger [79], leading to a 2 order of magnitude increase in the range of the constrained speed on either side. While comparing the arrival time of the gravitational waves to the arrival time of the gamma rays requires various model assumptions, not present in the direct method, the precision of this method nevertheless vastly exceeds what could ever be obtained with the direct method presented here. Disagreement between the direct

method and the electromagnetic counterpart method would be nearly inexplicable. Not surprisingly, we find no such disagreement.

In this paper, we employ an approach similar to that used in Ref. [75], to make a local measurement of the speed of gravity based on the difference in arrival time across a network of GW detectors for pure GW observations made during O1 and O2. We consider both measurements of the speed of gravitational waves from individual events and then demonstrate how the accuracy can be improved by combining measurements from multiple GW observations. In Sec. 4.2, we discuss our methods and in Sec. 4.3 we present the speed of gravity results. Finally, in Sec. 4.4, we use a subset of the individual speed of gravity results to obtain constraints on local Lorentz violation in the context of the effective-field-theory-based test framework provided by the gravitational Standard-Model Extension (SME) [80, 81, 82, 83] within which a number of recent theoretical [84, 85, 86] and experimental [76, 87] studies of GWs have been performed. While the results achieved here are much weaker than those attained via multimessenger astronomy in Ref. [76], the analysis presented here offers several novel features. In Ref. [76], constraints on SME coefficients were attained using a maximum-reach approach [88], effectively constraining a series of 9 models having one parameter each. Here, we attain simultaneous constraints on multiple coefficients for Lorentz violation using direct observations of the speed of gravity for the first time. In addition, the approach is quite different from both that of Ref. [76] and those of earlier works [80] and hence is subject to a different set of assumptions. For example, the current approach is free of the astrophysical-modeling assumptions used in Ref. [76]. This also provides the first direct limits on direction-dependent GW speeds.

4.2 Methods

4.2.1 Measuring the speed of gravitational waves with a single GW event

The standard parameter estimation based on GW data from multiple detectors imposes the constraint that the signal propagation across the network is at the speed of light [54]. It first generates a random time at Earth center within a small time window ($\pm 0.1s$) of an arrival time reported by a search pipeline, and then v_g is used to compute the corresponding time at each detector in order to generate waveform templates. In this work, however, we remove this constraint, allowing v_g to be a parameter in order to be estimated along with all other signal parameters.

GW data d_i collected at detector i, can be decomposed into pure GW signal $h_i(t)$ plus random noise $n_i(t)$:

$$d_i(t) = h_i(t) + n_i(t), \tag{4.1}$$

the posterior distribution of a set of parameters $\vec{\theta}$ can be obtained via Bayes' theorem:

$$p(\vec{\theta}|d_1, d_2, ...) = \frac{p(\vec{\theta})p(d_1, d_2, ...|\vec{\theta})}{p(d_1, d_2, ...)}, \tag{4.2}$$

$$\propto p(\vec{\theta})p(d_1, d_2, ...|\vec{\theta}), \tag{4.3}$$

where $p(\vec{\theta})$ is the prior distribution which reflects what we know about $\vec{\theta}$ before the measurement. $p(d_1, d_2, ...) = \int p(\vec{\theta})p(d_1, d_2, ...|\vec{\theta})d\vec{\theta}$ is a normalization factor known as evidence which is independent of $\vec{\theta}$ and it is useful for model selection. Assuming the noise is stationary and Gaussian distributed, the likelihood $p(d_1, d_2, ...|\vec{\theta})$ can be written as:

$$p(d_1, d_2, ...|\vec{\theta}) \propto \prod_i \exp\left[-\int_{-\infty}^{\infty} \frac{|d_i(f) - h_i(f|\vec{\theta})|^2}{S_i(f)} df\right], \tag{4.4}$$

where $d_i(f) = \int_{-\infty}^{\infty} d_i(t)e^{-2\pi i f t}dt$ is the Fourier transform of $d_i(t)$. $h_i(f|\vec{\theta})$ is a waveform in

the frequency domain. $S_i(f)$ is the noise power spectral density(PSD) which characterizes the sensitivity of the GW detector.

The marginalized posterior of the speed of gravitational waves v_g is obtained by integrating over other parameters:

$$p(v_g|d_1, d_2, ...) = \int p(v_g, \vec{\theta'}|d_1, d_2, ...)d\vec{\theta'}, \tag{4.5}$$

where $\vec{\theta'}$ is a set of parameters in $\vec{\theta}$ except for v_g. Markov Chain Monte Carlo(MCMC) with Metropolis-Hastings algorithm [50, 51, 52] is an effective method to sample from multi-dimensional posterior distributions.

4.2.2 Combing multiple GW events

The accuracy of the speed of gravitational waves measurement can be improved by combing multiple GW events. Suppose the GW detectors observed n events with data $d_1, d_2, ..., d_n$, the posterior of v_g for the joint events can be computed by applying Bayes' theorem and assuming the events are mutually independent:

$$p(v_g|d_1, d_2, ..., d_n) \propto \frac{p(v_g|d_1)p(v_g|d_2)...p(v_g|d_n)}{p^{n-1}(v_g)}, \tag{4.6}$$

where $p(v_g|d_i)$ is the marginalized posterior of v_g for event i and $p(v_g)$ is prior distribution of v_g. With uniform prior, the Eq. 4.6 is simplified to:

$$p(v_g|d_1, d_2, ..., d_n) \propto p(v_g|d_1)p(v_g|d_2)...p(v_g|d_n), \tag{4.7}$$

which says that marginalized posterior of v_g for joint events is proportional to the product of marginalized posterior of v_g for a single event.

To estimate how much improvement of the combing measurement, we assume posterior of v_g for n GW events are independent and identical Gaussian distribution, i.e. $p(v_g|d_i) \propto$

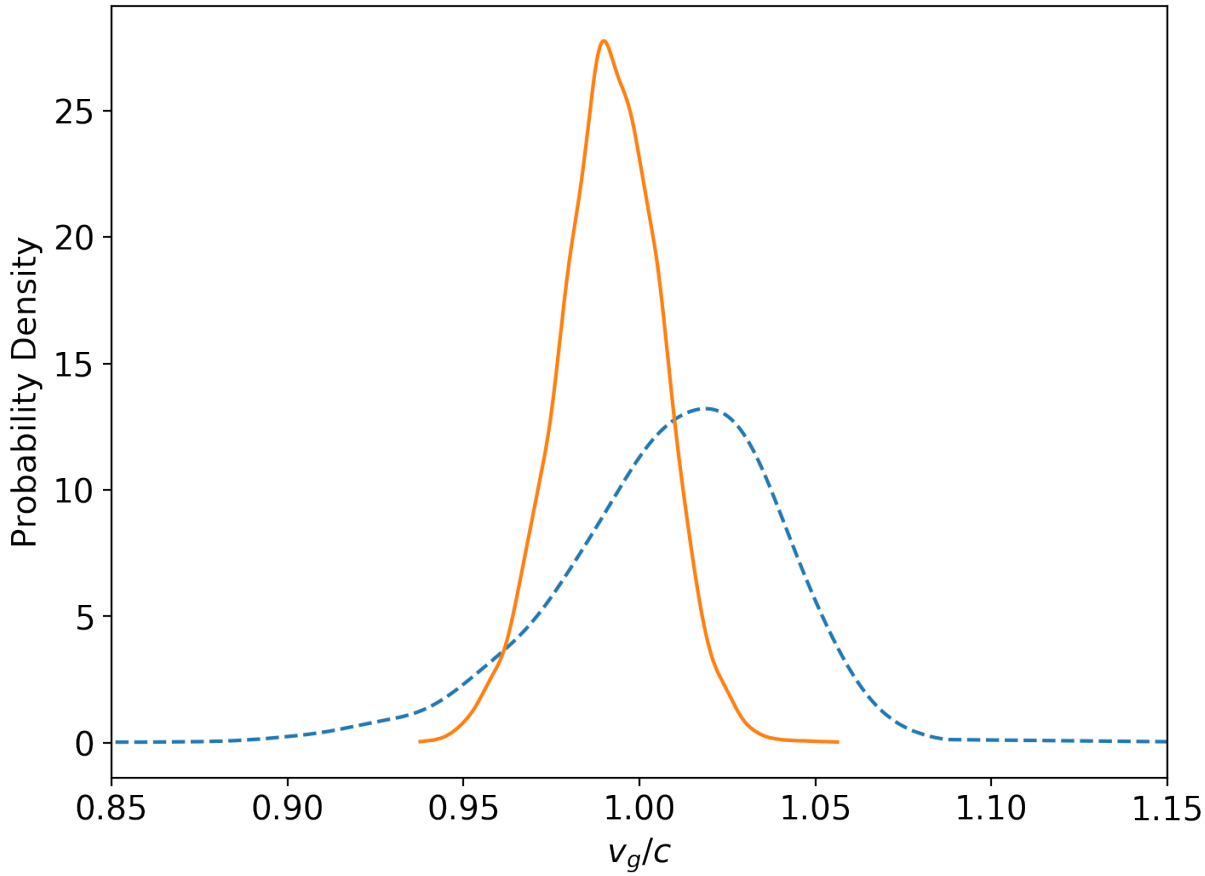

Figure 4.1: Marginalized posterior distributions of v_g for GW170817. The solid line is obtained from the run with fixing α and δ at the electromagnetic counterpart, whereas the dashed line obtained from the run without fixing α and δ.

$\exp(-(v_g-\mu)^2/(2\sigma^2))$. Then, the combined posterior becomes $p(v_g|d_1, d_2, ..., d_n) \propto \exp(-(v_g-\mu)^2/(2\sigma^2/n))$. Therefore, the combing method is expected to reduce standard deviation of a single measurement by a factor of $\sqrt{n}$.

4.3 Results

We use `LALINFERENCE_MCMC` [54] which implements MCMC with Metropolis-Hastings algorithm to run the Bayesian parameter estimation. In this paper, we use a uniform prior in v_g, the prior upper bound of v_g can be estimated by using GW coalescence times [37] at two LIGO detectors and assuming GW source, and two LIGO detectors are on the same line.

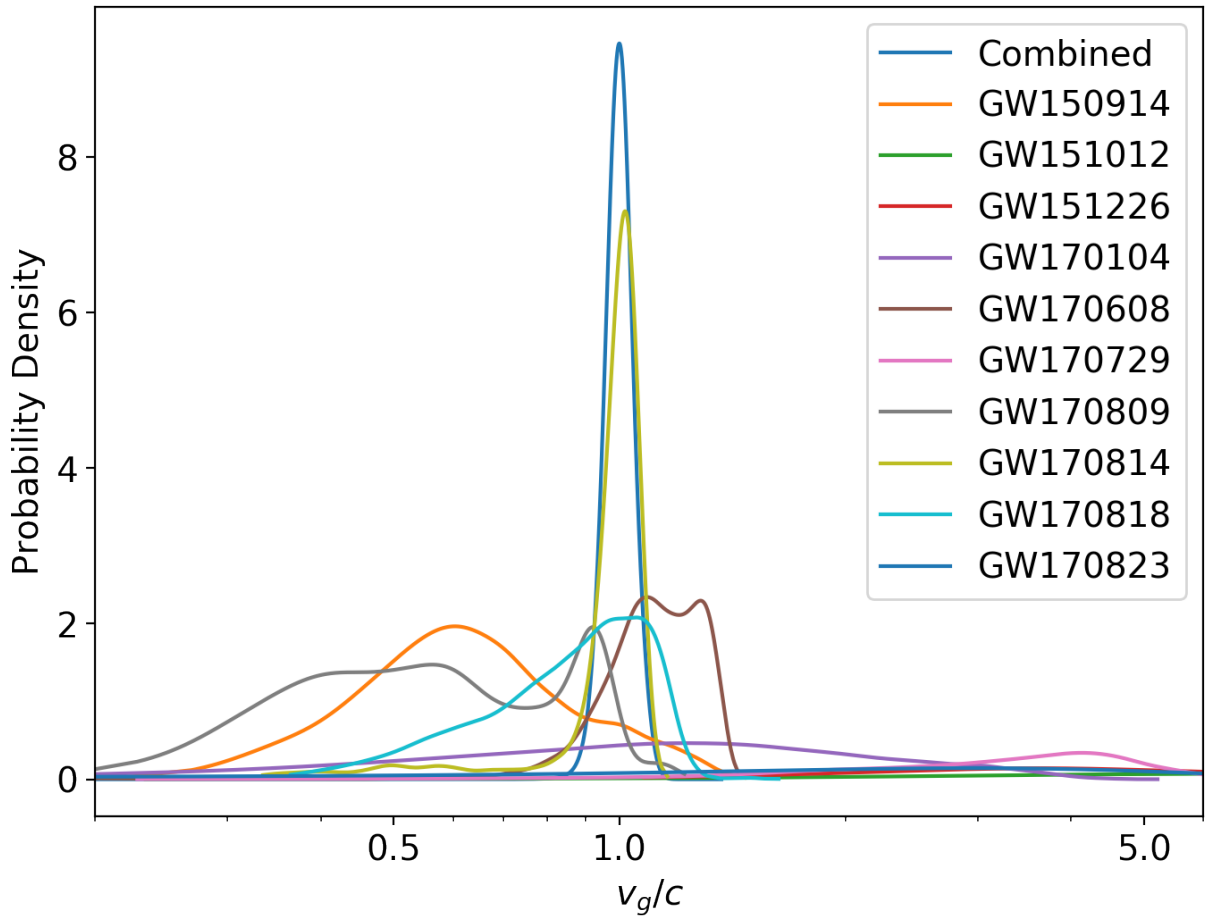

Figure 4.2: Posterior distributions of v_g for ten BBH events: GW150914, GW151012, GW151226, GW170104, GW170608, GW170729, GW170809, GW170814, GW170818, GW170823, and combined posterior. The combined posterior is computed using Eq. 4.7.

Here, we take coalescence time to be the time when the GW amplitude peaks. Suppose that for a GW event, the coalescence time at Hanford is t_H, Livingston is t_L and distance between Hanford and Livingston is d, then the prior upper bound $max(v_g) = d/(|t_H - t_L| + 2\sigma)$, where σ is the uncertainty of the coalescence time.

In our analysis, we choose the IMRPhenomPv2 waveform [89] for all BBH events and TaylorF2 for the BNS event. IMRPhenomPv2 is a processing BBH waveform with inspiral, merger and ringdown. TaylorF2 [90, 91, 92, 93, 94, 95] is a frequency domain post-Newtonian waveform model that includes tidal effects.

The first detection of binary neutron star inspiral GW170817 by Advanced LIGO and Advanced Virgo provides an accurate measurement for v_g. The BNS event has a network signal to noise ratio(SNR) 33 [8] which is the highest in all GW events detected in O1 and O2. The sky localization is precisely constrained to an area of 16 deg^2. Those two aspects of GW170817 allow an accuracy v_g measurement to a $(0.95c, 1.06c)$ 90% confidence interval. The later electromagnetic counterpart was discovered in the galaxy NGC4993 [96], which enable us to fix the right ascension(α) and declination(δ) at the electromagnetic counterpart during MCMC sampling. The later measurement shrinks the 90% confidence interval of v_g to $(0.97c, 1.02c)$. The marginalized posteriors of v_g for GW170817 with and without fixing α and δ at the electromagnetic counterpart are shown in FIG. 4.1.

FIG. 4.2 shows the posterior distributions of v_g for ten O1 and O2 BBH events, and the combined posterior is obtained by using Eq. 4.7. Narrow sky localization and high SNR of a GW event can help to better constrain on v_g. v_g for GW170809, GW170814 and GW170818 are well constrained due to the fact that they were observed by the three GW detectors which can help to better localize the GW sources. GW170729 was also observed by the three detectors, due to its lower SNR, v_g of GW170729 is poorly measured. GW150914 and GW170608 were only observed by the two LIGO detectors, however, due to its higher SNR, they are better constrained than GW170729. GW151012, GW151226, GW170104, and GW170823 were also observed by the two LIGO detectors, but the sky localization

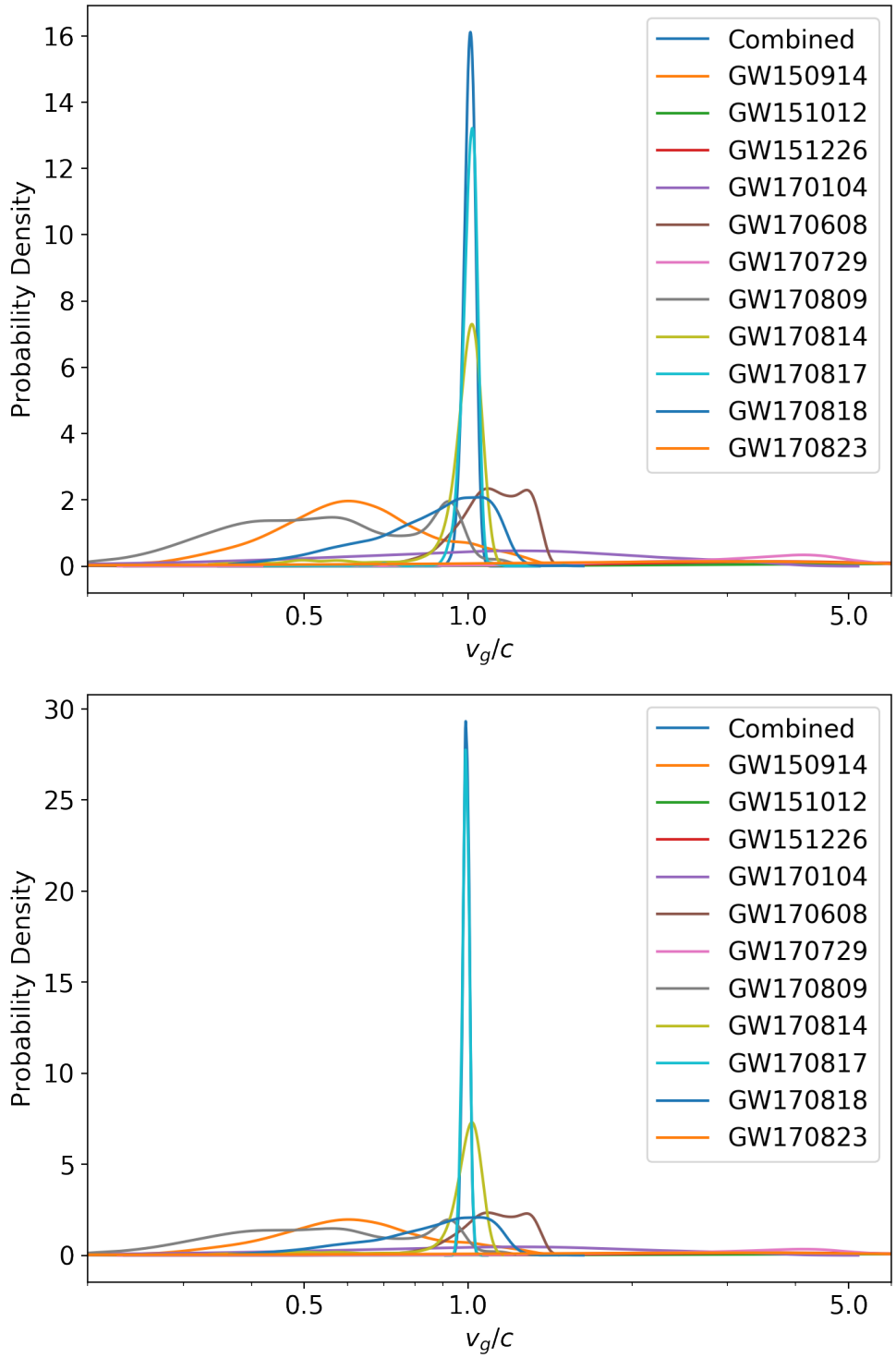

Figure 4.3: Posterior distributions of v_g for ten BBH and a BNS detected in O1 and O2: GW150914, GW151012, GW151226, GW170104, GW170608, GW170729, GW170809, GW170814, GW170817, GW170818, GW170823, and combined posterior. For GW170817 α and δ are free parameters in the top plot, in the bottom plot α and δ are fixed at the electromagnetic counterpart.

Table 4.1: 90% credible intervals of v_g from individual events posteriors and combined posteriors. GW170817(fixed) obtain from the MCMC run with fixing α and δ at the electromagnetic counterpart and GW170817 treats α and δ as free parameters. Combined(BBH) obtained from the seven BBH. Combined(fixed) and Combined uses seven BBH and GW170817 with and without fixing α and δ respectively. Network SNR values are reported from the GstLAL search pipeline [8]. 90% confidence regions of the sky localization (Ω) with fixing v_g at c are presented in GWTC-1[8] and without fixing v_g are computed from posteriors of α and δ.

Events	90% Confidence Intervals	Network SNR	Ω/deg^2 GWTC-1	Ω/deg^2
GW150914	(0.35c, 1.14c)	24.4	182	2385
GW151012	(2.95c, 16.19c)	10.0	1523	6607
GW151226	(1.22c, 12.00c)	13.1	1033	6515
GW170104	(0.34c, 3.27c)	13.0	924	5313
GW170608	(0.91c, 1.38c)	14.9	396	1269
GW170729	(1.56c, 5.83c)	10.8	1033	1287
GW170809	(0.30c, 1.01c)	12.4	340	2252
GW170814	(0.88c, 1.11c)	15.9	87	250
GW170817	(0.95c, 1.06c)	33.0	16	53
GW170817(fixed)	(0.97c, 1.02c)	33.0	0	0
GW170818	(0.59c, 1.21c)	11.3	39	168
GW170823	(0.10c, 12.19c)	11.5	1651	6412
Combined(BBH)	(0.93c, 1.07c)			
Combined	(0.97c, 1.05c)			
Combined(fixed)	(0.97c, 1.01c)			

of these events are poorly constrained, hence posteriors of v_g for these two events are relatively flat. The 90% confidence interval of v_g for GW170814 is (0.88c, 1.11c) which is the best measurement among the BBH events detected in O1 and O2. The 90% confidence interval of the combined posterior of all BBH shrinks to (0.93c, 1.07c) which improved by 30% relative to GW170814. The 90% confidence intervals for all individual events and the combined posteriors are listed in TABLE 4.1.

By including the ten BBH events and the BNS event, the combined posterior is constrained to (0.97c, 1.05c) and (0.97c, 1.01c) for GW170817 with and without fixing α and δ at the electromagnetic counterpart respectively. Top plot of FIG. 4.3 shows the combined posterior alone with posteriors of seven BBH events and GW170817 without fixing α and δ, and the bottom plot shows the results with fixing α and δ at the electromagnetic counterpart. We can see that most of the contribution to the combined posteriors comes from GW170817 because it is measured more accuracy than other BBH events. The narrow posterior of GW170817 can also help to remove tails from the combined posteriors, the two combined posteriors with GW170817 show fewer tails than the combined posterior with BBH only.

The speed of gravitational waves is correlated with the sky localization of a GW source. When v_g is allowed as a free parameter in the parameter estimation, the uncertainty of α and δ tend to increase. FIG. 4.4 shows the comparison of skymaps with and without fixing v_g at c, and the corresponding 90% confidence regions of the sky localization are listed in TABLE 4.1. If gravitational waves propagate at a speed different at the speed of light, the skymap obtained from the parameter estimation where v_g is fixed at the speed of light could be biased.

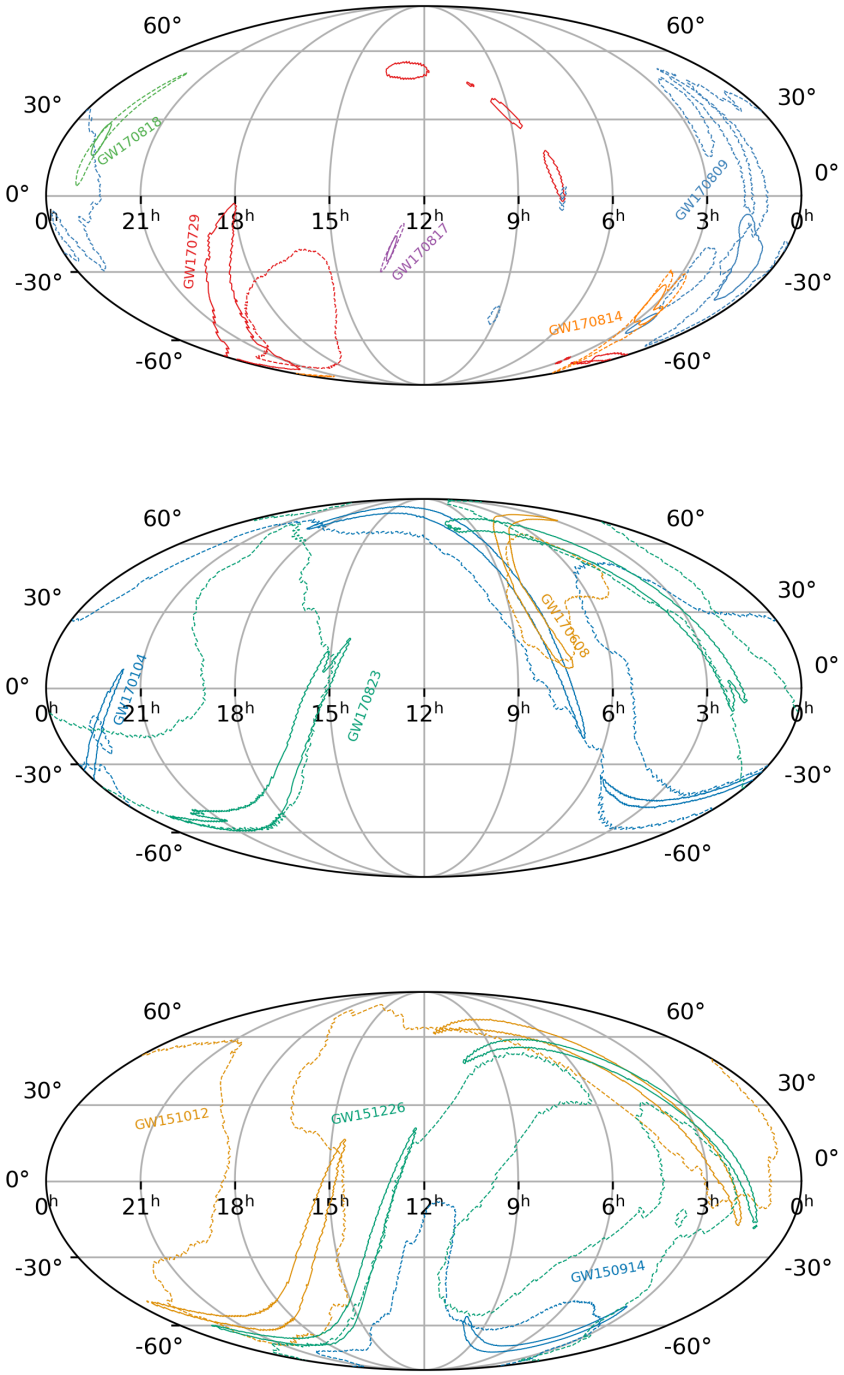

Figure 4.4: 90% credible regions for the sky localizations of all GW events detected in O1 and O2. The solid contours are obtained from the posteriors where the speed of gravitational waves is fixed at the speed of light, the dashed contours shows the results for v_g as a free parameter. Top: events detected by Advanced LIGO and Advanced Virgo (GW170729, GW170809, GW170814, GW170817, GW170818); middle: events detected by the two Advanced LIGO detectors in O2 (GW170104, GW170608, GW170823); bottom: events detected in O1 (GW150914, GW151012, GW151226).

4.4 Local Lorentz Violation

The 9 nondispersive, nonbirefringent coefficients for Lorentz violation in the gravity sector of the SME cause modification of the group velocity of GWs. Using natural units and the assumption that the nongravitational sectors, including the photon sector, are Lorentz invariant, the modified group velocity can be written as follows [84]:

$$v_g = 1 + \tfrac{1}{2}\sum_{jm}(-1)^j Y_{jm}(\alpha,\delta)\overline{s}_{jm}. \tag{4.8}$$

Here a basis of spherical harmonics Y_{jm} in which $j \leq 2$ has been used to express the 9 Lorentz-violating degrees of freedom $\overline{s}_{jm}$ present in this limit of the SME. While the sum on m ranges from $\pm j$ in Eq. (4.8), the equivalent expansion over positive m:

$$v_g = 1 + \sum_j (-1)^j \Big(\tfrac{1}{2}\overline{s}_{j0} Y_{j0} + \sum_{m>0} [\mathrm{Re}\ \overline{s}_{jm} \mathrm{Re}\ Y_{jm} - \mathrm{Im}\ \overline{s}_{jm} \mathrm{Im}\ Y_{jm}] \Big), \tag{4.9}$$

is conventionally chosen in expressing experimental sensitivities.

With 11 GW events detected in O1 and O2, it is possible to simultaneously constrain all 9 of the $\overline{s}_{jm}$ coefficients for Lorentz violation. However, some of these have significant uncertainty in both v_g and sky position α, δ. Hence we explore a model formed by the $j \leq 1$ subspace of the full SME, using 4 of the most sensitive events and the following methods.

In the earlier sections of the paper, data from the multiple events were combined under the assumption of isotropic GW speeds to obtain a more sensitive measurement. Here we exploit a complementary advantage of the multiple observations in constraining direction-dependent speeds. To develop the methods, imagine that one had an exact measurement of v_g as well as sky position for a GW event. Then Eq. (4.9) would form 1 equation with 4 unknowns (the 4 coefficients $\overline{s}_{jm}$ in our model). Given 4 such events, assuming unique

sky locations, the system of 4 equations that results could be solved for the 4 coefficients $\overline{s}_{jm}$ forming a measurement of Lorentz violation. Of course in the present case of real experimental work we have a distribution for each of our 4 events rather than a signal value. We use this data by randomly drawing a sample from the distribution for each of the 4 events, solving for the corresponding values of the 4 coefficients $\overline{s}_{jm}$, and repeating the process to build the $\overline{s}_{jm}$ distribution.

Using GW170608, GW170814, GW170817, and GW170818 (lines 2, 5, 6, and 8 of Table 4.1) we obtain the results shown in Fig. 4.5. In Fig. 4.6, we use the same events but with the fixed sky position as in line 7 of Table 4.1. This generates a modest narrowing of the one sigma range for some coefficients. This generates only small changes in the plot. We also explored setting the speed of gravity for the GW170817 event to that found in Ref. [76]. This also results in an insignificant effect on the confidence bands.

Note that the measurements of the $\overline{s}_{jk}$ shown in Figs. 4.5 and 4.6 are consistent with zero. Hence we can interpret the one sigma range shown as upper and lower bounds on the values of the $\overline{s}_{jk}$ coefficients, an exclusion of the simplest types of direction-dependent speeds. As with v_g, these limits are considerably weaker than some found in the literature [80]. However, they carry value in that they are obtained from significantly different methods than other tests, are the first effort to simultaneously constrain multiple $\overline{s}_{jk}$ using speed of gravity measurements, and begin establishing methods for future higher-sensitivity tests.

As a final note, we point out that if the isotropic limit of the SME is considered such that $\overline{s}_{00}$ is the only nonzero coefficient for Lorentz violation, then the combined v_g results in the last line of Table 4.1 may be applied. Doing so yields $-0.2 < \overline{s}_{00} < 0.07$.

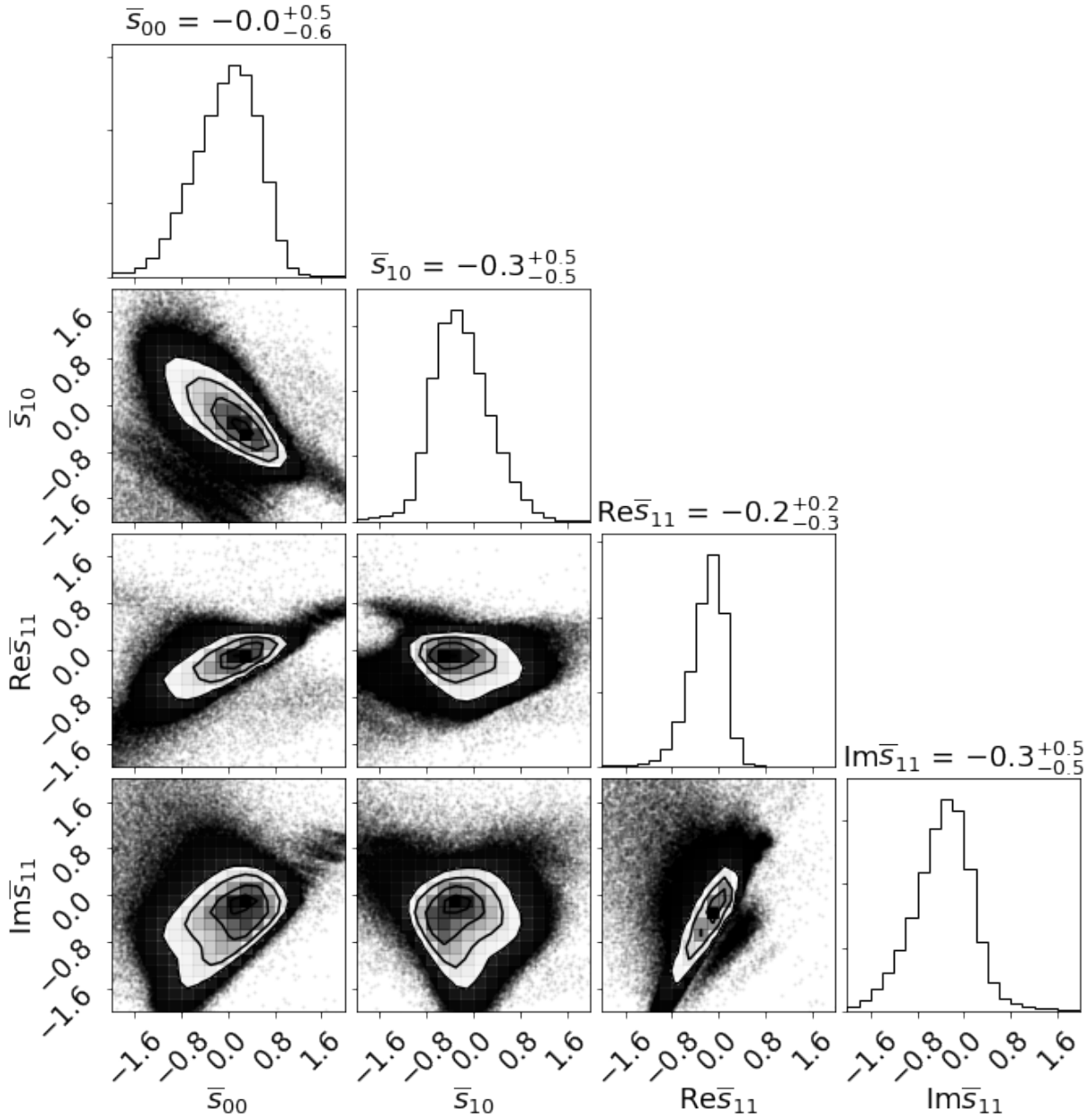

Figure 4.5: The distribution of $\bar{s}_{jm}$ values implied by the events listed on lines 2, 5, 6, and 8 of Table 4.1. Numbers above the plots show best values with a one sigma range.

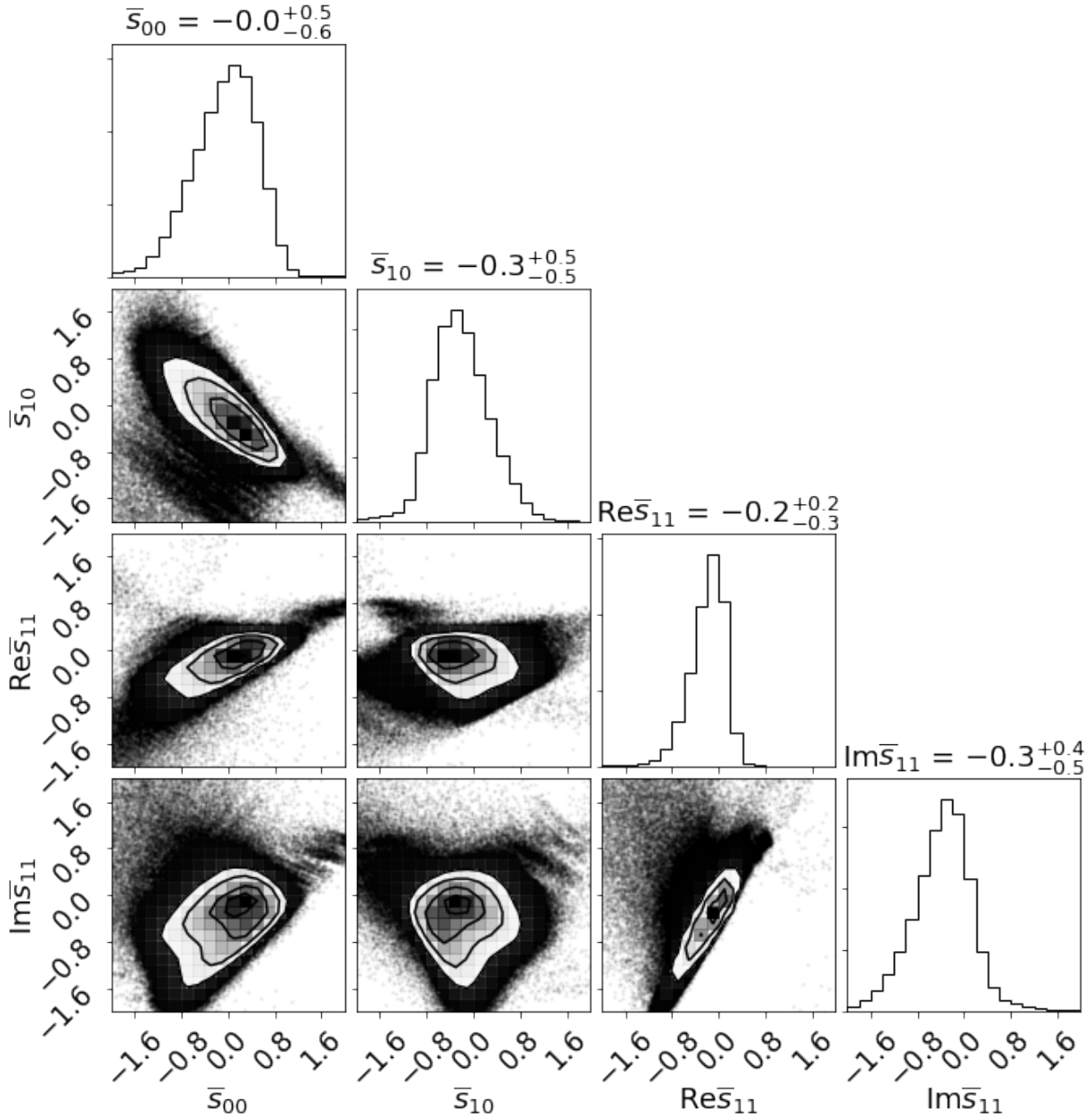

Figure 4.6: The distribution of $\overline{s}_{jm}$ values implied by the events listed on lines 2, 5, 7, and 8 of Table 4.1. That is, relative to Fig. 4.5, the sky position of GW170817 is fixed. Numbers above the plots show best values with a one sigma range.

4.5 Conclusions

While the association between GWs and gamma-rays observed with GW170817 and GRB 170817A have provided an extremely tight bound on the difference between the speed of gravitational waves and the speed of light, in this paper we have presented an independent method of directly measuring v_g, which, while less precise, is based solely on GW observations and so not reliant on multimessenger observations. We continue to find measured values of v_g consistent with the speed of light, as predicted by General Relativity, not just for GW170817 but also for other signals detected during the second observation run of Advance LIGO and Virgo. By combining these measurements and assuming isotropic propagation, we constrain the speed of gravitational waves to (0.97c, 1.01c) which is within 3% of the speed of light in a vacuum. We also obtain simultaneous constraints on nonbirefringent, nondispersive coefficients for Lorentz violation in the test framework of the SME. Though the constraints are not as strong as other methods, we simultaneously limit multiple coefficients using direct speed of gravity tests for the first time, directly constraining the possibility of an anisotropic speed of gravity. Other implications for deviations from general relativity arising from cosmological evolution were considered in Ref. [97].

There are some limitations of the approach used here that must be acknowledged. First, should the speed of gravitational waves differ from the speed of light — in violation of the predictions of General Relativity — then we would not necessarily expect other assumptions based on General Relativity predictions to necessarily hold. Among the assumptions that could affect us is the assumption that the gravitational waves only exist in two tensorial transverse polarizations. More general metric theories of gravity could allow for up to 6 independent polarizations, including in addition two longitudinal-vector polarizations and two scalar polarizations (one longitudinal and one transverse, thought these are indistinguishable in interferometric detectors). The observations of GW170817 as well as others events detected in O1 and O2 show that the pure tensor mode is strongly favored over the pure vector or pure scalar mode [98, 99]. The dominant tensor mode could be

mixed with smaller scalar and/or vector modes propagating with the same speed. Even in that case, the presence of the vector mode has already constrained weakly with GW170817 by constructing a null stream [100]. Our parameter estimation has continued to assume that only the tensor polarization states exists. Furthermore, we continue to assume that the gravitational waveforms are as predicted by general relativity. Nevertheless, our measurement of v_g is mostly constrained by the measured times of arrival of the signal in the various detectors, so we believe it is reasonably robust.

In addition, as noted in Ref. [75] the searches that identify GW signals normally require a signal to be seen in two detectors and impose a time window. For example, for the LIGO Hanford Observatory and the LIGO Livingston Observatory, the searches required arrival times within 15 ms (while the light travel time between those detectors is 10 ms) [101]. This would seemingly create a selection bias against gravitational wave signals with $v_g < \frac{2}{3}c$. However (again as noted in Ref. [75]) a gravitational wave signal can also be identified in a single detector, and, for sufficiently loud signals, the presence of a signal in another detector at similar time would unlikely go unnoticed. For this reason we do not think there is a strong selection bias against slow moving gravitational waves.

Chapter 5

Identifying strong gravitational-wave lensing during the second observing run of Advanced LIGO and Advanced Virgo [1]

5.1 Introduction

When gravitational waves (GWs) propagate near massive galaxies or galaxy clusters, similar to light, the GWs can be strongly lensed. If the massive galaxies or galaxy clusters are along the line of sight of the GW source, GW observatories are expected to see multiple images with a time delay of hours to weeks [103] from the same astrophysical source as long as both images are above the GW detection threshold. Based on predictions of the number of expected GW sources and the distribution of lenses in the universe, [104, 105] suggested that around one in a thousand events observed by Advanced LIGO and Advanced Virgo [11, 6, 24, 10] at design sensitivity will be lensed. The rate computations typically assume

[1] This chapter is based on Ref [102]

that a single image is detected, and the majority of the lenses are galaxy lenses. The lensing rate is expected to be lower at O2 sensitivity and even lower when considering double images. Galaxy cluster lenses have been investigated in [106, 107, 108, 109, 110], who found that the rate of galaxy cluster lensing is around $10^{-5}\,\mathrm{yr}^{-1}$ at O1 sensitivity, and given the fact that the small sensitivity improvement in O2, we do not expect that the rate has notably increased. Lensing event rates can also be inferred with the measured amplitude of the BBH background as shown in [111, 112].

Under the presence of a lens, the corresponding strongly lensed GW signal is magnified such that $\rho_l = \sqrt{\mu}\rho$ [113], where ρ_l and ρ are the signal-to-noise ratios (SNRs) under the lensed and unlensed models, respectively, and μ is the relative magnification factor [114, 115]. Since the gravitational wave frequency evolution is not affected by strong lensing, the lensing magnification is equivalent to a scaling of the source luminosity distance by a factor of $1/\sqrt{\mu}$ [113, 116]. Thus, a loud and nearby GW signal observed by GW detectors could potentially be lensed and thus appear to be more distant than it seems. Also, inferring the source frame chirp mass $\mathcal{M}_c^{source}$ relies on the detector frame chirp mass $\mathcal{M}_c$ and the redshift z: $\mathcal{M}_c = (1+z)\mathcal{M}_c^{source}$. In the geometrical optics regime, lensing does not affect frequencies; hence, and hence the detector frame chirp mass is not affected. Rather, the inferred amplitude is larger (smaller) if the event is magnified (demagnified), and if we assume the event is an unlensed event in the background cosmology, the relation between distance (through the amplitude) and the redshift would lead us to infer a larger (smaller) source frame mass.

In addition, according to [117, 118], lensing shifts the original phase of the waveform by $\Delta\phi$ in such a way that the shift is absorbed into the phase of the coalescence $\Delta\phi_c$ in the case of of gravitational waves with the relation $\Delta\phi = 2\Delta\phi_c$ (except if precession, eccentricity, or higher modes are present) [119]. The shift depends on the type of lensed image: Type-I induces no phase shift, type-II induces a $+\pi/2$ phase shift, and type-III images induce a $+\pi$ phase shift. In electromagnetic observations, Type-III images are typically suppressed and

rarely seen (save for some rare exceptions [120, 4]), because they occur near the maximum of the lens potential, where there is usually a lens galaxy or galaxy cluster; hence, it is hard to pick out faint images on top of a luminous lens. In GW observations, this type of image is expected to be demagnified; therefore, one would typically expect lensed gravitational waves to consist of type-I or type-II images.

During the second observing run of Advanced LIGO and Advanced Virgo, seven binary black holes [72, 73, 74, 8] and one binary neutron star (BNS) [14] were detected. A search for gravitational-wave lensing signatures on the GWTC-1 catalog [8] was performed in [115], but no good evidence of strong lensing was found. Note that the highest Bayes factor event pair in the analysis was the GW170104-GW170814 pair, but this was disfavored due to 1) the large time-delay between the events and 2) the prior probability of lensing being low, around $\sim 10^{-5}\,\mathrm{yr}^{-1}$ at O1 sensitivity [106] for galaxy cluster lensing, and relative lensing rate of $\lesssim 10^{-2}$ for galaxy lensing [121, 115]. If one or more of the observed images is of type-III, the rate is understood to be significantly lower.

The same event pair was studied in more detail in [109], which appeared at the time of writing of this article. A third, sub-threshold image consistent with the lensing hypothesis was found, GWC170620, which was first discovered in the PyCBC sub-threshold search [122]. The authors further analyzed the image configurations required for the lensing hypothesis, finding that it would consist of either one or two type-III images, and would require a galaxy cluster lens due to the long time delay. Neglecting the a priori probability of lensing, the false alarm probability for the double (triplet) was estimated at $\sim 10^{-4} - 10^{-2}$ depending on specific O2 GW events [109]. However, when accounting for the prior probability of lensing and the fact that the observed images would require a very peculiar image configuration, the lensing hypothesis is disfavored; the authors concluded that there is not sufficient evidence to concluded that the event pair is lensed. The authors exclude the mass and other binary parameters that rely on the knowledge of the BBH population parameters to determine the false alarm rate of the pair due to lensing.

If the double/triplet events were lensed, then it would likely imply that the existing estimates of the lensing statistics are likely incorrect in predicting the relative fraction of galaxy cluster lenses and the total rate of lensed events (and hence the merger rate density of BBHs at high redshift). Another likely implication is a population of lenses that can form type-III images more frequently than observed in the electromagnetic spectrum. To reconcile for the discrepancy, one would likely require all of the following: 1) the merger rate density of BBHs rising at a higher rate than existing estimates from the usual formation channels, 2) galaxy cluster lenses making up a significant portion of the lensing optical depth, and 3) prominence of lensing configurations that can form heavily magnified type-III images in GW channels but not in electromagnetic channels.

In this paper, we present a Bayesian model selection method similar to [103], but instead of computing the lensing model evidence using kernel density estimation (KDE) from independent event posterior samples, we calculate the lensing evidence directly with parameter estimation by jointly fitting both images. We explicitly test the expected phase shifts and use an astrophysically motivated prior for the relative magnification factor. Moreover, we calculate the Bayes factors between the lensed and unlensed hypothesis, and from the measured time delays, we determine the prior odds for any two events to be likely images of each other to produce an odds ratio that we can use to test the lensed and unlensed hypotheses.

5.2 Gravitational lensing model selection

For a GW signal at luminosity distance D_L, the amplitudes of the corresponding lensed images are magnified by a factor of $\sqrt{\mu_i}$, where i labels the corresponding absolute magnification factor for each image so that the observed luminosity distances will be

$$D_L^{(i)} = D_L/\sqrt{\mu_i}\,, \tag{5.1}$$

Since the magnification factors and luminosity distances are degenerate, the individual magnification factors are difficult to constrain. Thus, we instead use the relative magnification factor μ,

$$\mu = \left(\frac{D_L^{(1)}}{D_L^{(2)}}\right)^2 = \frac{\mu_2}{\mu_1}\,, \tag{5.2}$$

where $D_L^{(1)}$ and $D_L^{(2)}$ are the observed luminosity distances of the first and second images, respectively, and μ_1 and μ_2 are the corresponding absolute magnification factors.

For strong lensing, the probability distribution for the individual magnifications is well known in the high-magnification limit and is given by $p(\mu_i) \propto \mu_i^{-3}$ [123]. To estimate the prior distribution of the relative magnification factor μ, we follow the simulation in [103], and obtain $p(\mu) \propto \mu$ for $\mu < 1$, $p(\mu) \propto \mu^{-3}$ for $\mu \geqslant 1$.

Given two observed detector strains $d_1(t)$ and $d_2(t)$ with confirmed GW detections, we want to determine whether these two signals are lensed or not. The lensed hypothesis $\mathcal{H}_L$ states that the two signals come from the same astrophysical source and are thus lensed. Meanwhile, the unlensed model $\mathcal{H}_U$ assumes that the two signals are from independent astrophysical sources. Under the lensing hypothesis, we first introduce a set of common parameters for the two events, $\eta = \{m_1, m_2, a_1, a_2, \iota, \alpha, \delta, \psi\}$, where m_1 and m_2 are the component detector frame masses, a_1 and a_2 are the component spins, ι is the inclination angle of the binary, α and δ are the right ascension and declination, and ψ is the polarization angle. We also introduce lensing dependent parameters, $\zeta = \{D_L, \phi_c, t_c\}$ where D_L is the luminosity distance to the source, ϕ_c is the coalescence phase, which can only be discretely different, and t_c the time at coalescence. Hence, for the lensed hypothesis, we expect the common parameters η to be the same for the two events and only for the lensing dependent parameters to differ. Thus, the likelihood under the lensed hypothesis, given GW strain data d_1 and d_2, can be written as:

$$P(d_1, d_2|\vec{\theta_1}, \mathcal{H}_L) = P(d_1|\eta, \zeta_1, \mathcal{H}_L)P(d_2|\eta, \zeta_2, \mathcal{H}_L), \tag{5.3}$$

where d_1, ζ_1, and d_2, ζ_2 are the data and independent parameters for the first and second images respectively. Note that for this model, we sample the magnification factor μ instead of $D_L^{(2)}$ in the independent parameters ζ_2.

For the unlensed hypothesis, the parameters of the two events are sampled independently. The likelihood in the unlensed hypothesis $\mathcal{H}_U$, is simply the product of the likelihoods of the two events, since they are independent of each other,

$$P(d_1, d_2|\vec{\theta_2}, \mathcal{H}_U) = P(d_1|\eta_1, \zeta_1, \mathcal{H}_U)P(d_2|\eta_2, \zeta_2, \mathcal{H}_U), \tag{5.4}$$

where η_1, ζ_1, and η_2, ζ_2 are the parameters for the first and the second GW events, respectively.

To compare the two models, we compute the ratio of the evidences $P(d_1, d_2|n_j, \mathcal{H}_L)$ and $P(d_1, d_2|\mathcal{H}_U)$, also known as the Bayes factor,

$$B_U^L = \frac{P(d_1, d_2|n_j, \mathcal{H}_L)}{P(d_1, d_2|\mathcal{H}_U)} = \frac{\int P(d_1|\eta, \zeta_1, \mathcal{H}_L)P(d_2|\eta, \zeta_2, \mathcal{H}_L)P(\eta, \zeta_1, \zeta_2|\mathcal{H}_L, n_j)d\eta d\zeta_1 d\zeta_2}{\int P(d_1|\eta_1, \zeta_1, \mathcal{H}_U)P(d_2|\eta_2, \zeta_2, \mathcal{H}_U)P(\eta_1, \zeta_1, \eta_2, \zeta_2|\mathcal{H}_U)d\eta_1 d\zeta_1 d\eta_2 d\zeta_2}, \tag{5.5}$$

where n_j is the Morse index, which determines the type of lensing image (type-I/II/III) and thus the expected phase difference for the pair, while $P(\eta, \zeta_1, \zeta_2|\mathcal{H}_L, n_j)$ and $P(\eta_1, \zeta_1, \eta_2, \zeta_2|\mathcal{H}_U)$ are the priors for the lensed and unlensed hypothesis, respectively. We calculate the lensing evidence with nested sampling [53, 52] using `LALINFERENCE_NEST` [54].

The time delay between any two events can also be used to compute a corresponding timing Bayes factor [103, 115],

$$B_t = \frac{P(\Delta t|\mathcal{H}_L)}{P(\Delta t|\mathcal{H}_U)}. \tag{5.6}$$

We estimate the probability distribution $P(\Delta t|\mathcal{H}_L)$ through simulation following the methodology of [103]. We compute $P(\Delta t|\mathcal{H}_U)$, by assuming that independent (unlensed) events are Poisson distributed.

To obtain the odds for the lensed and unlensed hypotheses we compute,

$$O_U^L = \frac{P(d_1, d_2|n_j, \mathcal{H}_L)}{P(d_1, d_2|\mathcal{H}_U)} \frac{P(\Delta t|\mathcal{H}_L)}{P(\Delta t|\mathcal{H}_U)} \frac{P(\mathcal{H}_L)}{P(\mathcal{H}_U)}, \tag{5.7}$$

where the ratio $P(\mathcal{H}_L)/P(\mathcal{H}_U)$ is the prior odds for lensing compared to the unlensed event model. However, type-III images are very rare; hence, it is likely that the image shift corresponding to $\Delta\phi = \pm\pi$ is heavily disfavored: $p(n_j = 1|\mathcal{H}_L) \ll p(n_j = \{0, 1/2\}|\mathcal{H}_L)$.

The prior odds reflect our belief in the probability of lensing for any two events and can be estimated through simulations, as well as from electromagnetic observations. As such, we compute this via the ratio of expected lensed event to independent event rate. The relative lensed event rate has been estimated for galaxy lenses to be around $p(\mathcal{H}_L)/p(\mathcal{H}_U) \sim 10^{-3}$ at design sensitivity [104, 105], while Ref. [106] found the rate of galaxy cluster lensing to be $p(\mathcal{H}_L|\mathrm{O}_1) \sim 10^{-5} yr^{-1}$ at O1 sensitivity; we expect this to be somewhat larger at O2 sensitivity.

When comparing two models, the Bayesian evidence penalizes a more complex model. If we compare two models, the one with smaller prior volume or fewer parameters would be favored. This penalty is known as the Occam factor [124], which is automatically achieved by Bayesian inference. In our analysis, the lensing model has fewer parameters due to the parameter sharing. Indeed, when a signal is consistent with the lensed hypothesis, the magnitude of the Bayes factor is entirely set by the prior volume; a larger prior can increase the Bayes factor by several orders of magnitude, and vice versa. In order to reduce the prior volume difference between the two models, we impose a uniform in $\log(m_1)$ and $\log(m_2)$ priors, instead of the typical uniform priors on m_1 and m_2 (both in the detector frame). We impose a prior within the mass range of $1 - 100 M_\odot$. The difference between the prior volumes can be reduced by a factor of $10^2 - 10^3$ when using the uniform in log space prior. Also, the posteriors are almost unaffected by the change from one prior to another, because masses can be well constrained from data. In other words, this choice of

prior has a much greater effects on the prior volume rather than the posteriors. We note that an astrophysically motivated mass prior could be used instead, such as the power-law model used by the LVC [125], however, for the reasons stated above we decided to use the uniform in log prior instead.

We also take care of selection effects in the joint parameter estimation, since gravitational-wave detectors are not sensitive enough to at detecting all the binaries in the prior parameter space. Thus, we incorporate a selection function in the parameter estimation directly that keeps a sample if it is above the detection SNR threshold, otherwise it rejects the sample. We also note that taking into account selection effects is important when one or both events are below the detection threshold [126, 127], as will be the case when performing the joint parameter estimation using the potential third image, GWC170620 [109].

5.3 Results

We analyze potential pairs of lensed events from the second observing run of Advanced LIGO and Virgo. Due to the high computational cost of the parameter estimation, we select pairs of events that have similar sky localizations. We then run `LALINFERENCE_NEST` [54] to obtain the lensed and unlensed model evidences. We apply the selection function implemented in `LALINFERENCE_NEST` to the parameter estimation and set the network SNR threshold to 10 for single events and 14 for joint events, except for the sub-threshold event GWC170620. We sample uniformly in $\log(m1)$ and $\log(m2)$ for both lensed and unlensed models in order to mitigate the prior volume difference between models. The waveform used in our analysis is the IMRPhenomD approximant [41, 42], a non-precessing and spin aligned (22-mode only) frequency domain BBH waveform that enables us to test the different coalescence phase shifts due to different image types. Since there is no evidence that precession has been observed in any of the events detected in O1 and O2 [8], we expect that the IMRPhenomD model is sufficiently accurate for this analysis.

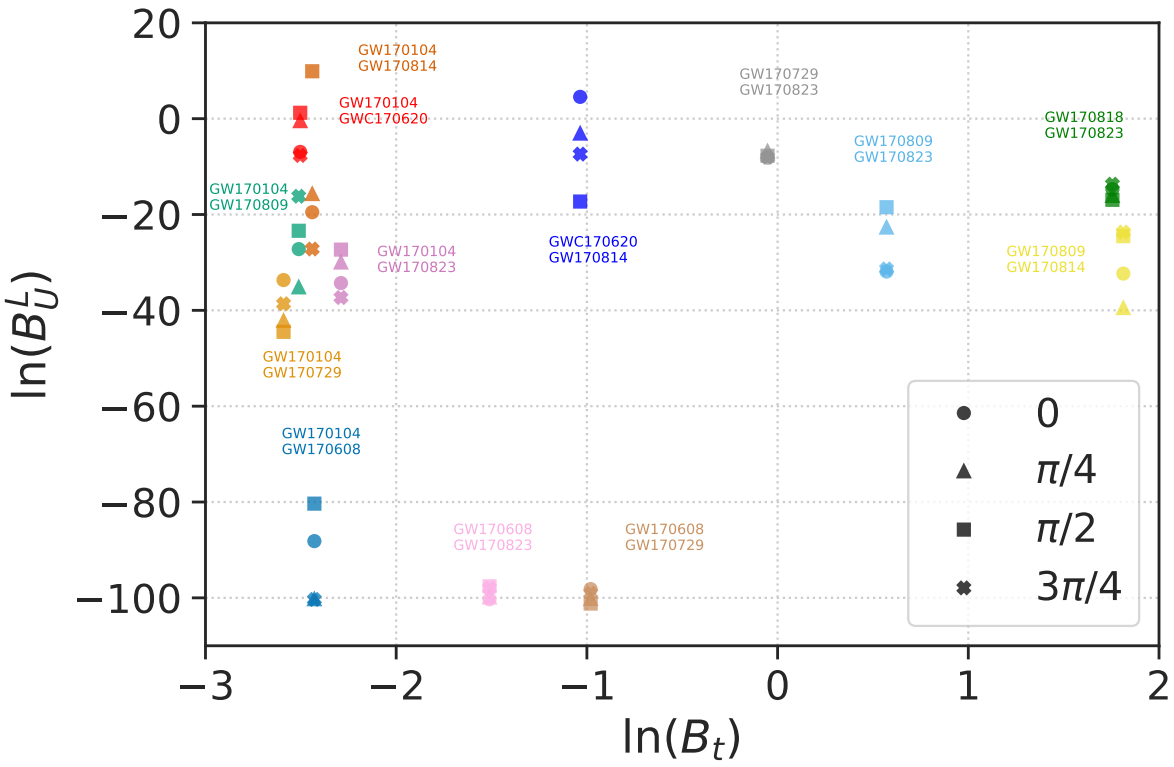

Figure 5.1: Natural logarithm of the Bayes factor B_U^L and B_t with 0, $\pi/4$, $\pi/2$, and $3\pi/4$ coalescence phase shifts for pairs of events detected in O2. The Bayes factors B_U^L are computed using `LALINFERENCE_NEST`, and the Bayes factor B_t is computed using the time delay between any two events.

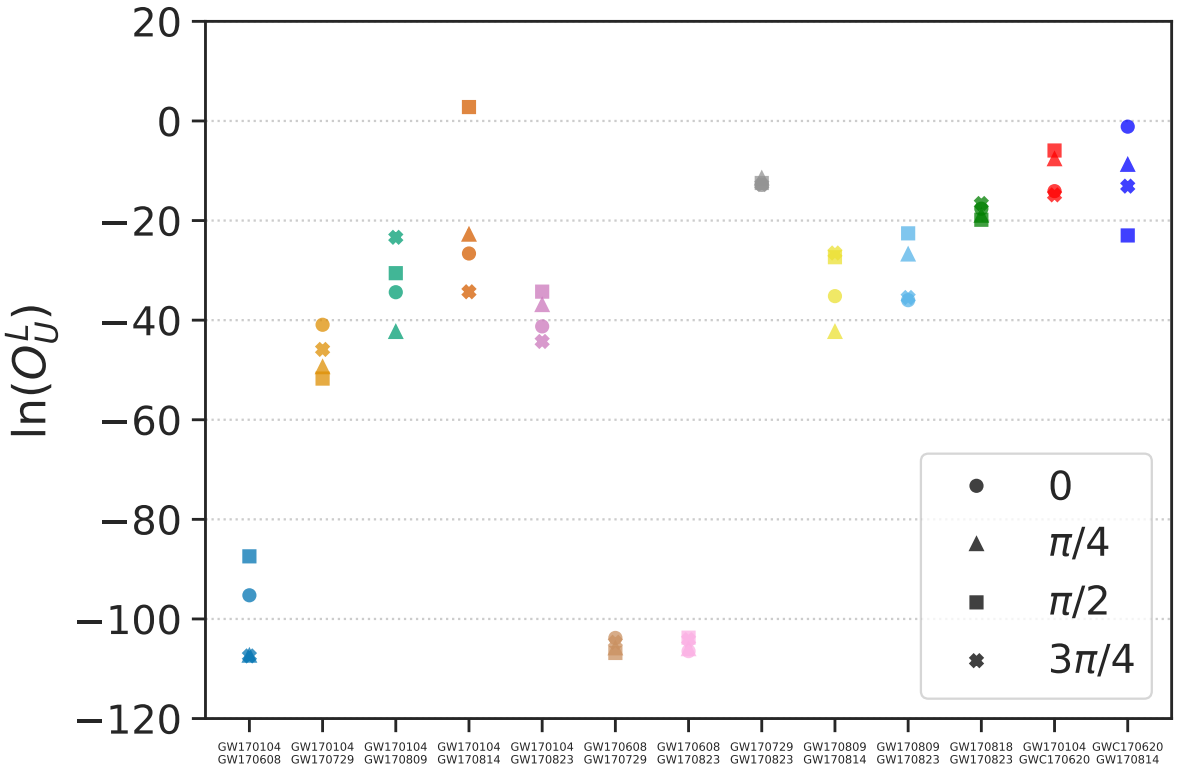

Figure 5.2: Natural logarithm of the odds O_U^L with 0, $\pi/4$, $\pi/2$, and $3\pi/4$ coalescence phase shifts for pairs of events detected in O2. The odds are computed using Eq. 5.7.

In Fig. 5.1 we show the Bayes factors B_U^L and B_t for pairs of events in O2. The lensed models for each pair of events are evaluated with the four different possible coalescence phase shifts. For the unlensed model, we sample the phases for each event independently. The GW170104-GW170814 pair with a $\pi/2$ coalescence phase shift has the largest Bayes factor $B_U^L \sim 1.98 \times 10^4$, favoring the lensed hypothesis in the absence of prior probability. The event could still be an unlensed event, however, as the two events could be from independent sources that have similar parameters. Therefore, we note that a high Bayes factor is not necessarily indicative of lensing. Nevertheless, it is intriguing that the event favors the lensing hypothesis even when including all of the binary parameters. The GW170809-GW170814 pair, which was suggested as a lensed event by Ref. [128], is clearly disfavored by the model selection.

The sky localization posterior for the GW170104-GW170814 pair is shown in Fig. 5.3. The sky localization posterior inferred under the lensing hypothesis (joint parameter estimation) is better constrained and lies within the overlap region of the GW170104 and GW170814 independent parameter estimation runs. The 90 percent confidence region is better constrained because the joint run has higher SNR than each individual run and benefits from the "extra detectors" (more baselines for localization) due to the different times of arrival of each image with respect to the rotation of the earth. We also show the posterior distributions over the parameters that we expect to be unchanged due to lensing in Fig. 5.4. Similarly, the parameters inferred under the lensing hypothesis are better constrained compared to those inferred independently.

Assuming an observation time of 9 months for O2, and the simulations in [103] we obtain an estimate for $P(\Delta t|L)$. For the unlensed case, we assume that the detected event rate follows a Poisson distribution, that is, $P(\Delta t|U) = 2(T - \Delta t)/T^2$, where T is the observation time. In Fig. 5.1 we show the Bayes Factor B_t of the lensing model with four different phase shifts compared to the unlensed model. Due to the ~ 7 month time delay between GW170104 and GW170814, the Bayes factor B_t is $\sim 8.7 \times 10^{-2}$. The Bayes factor

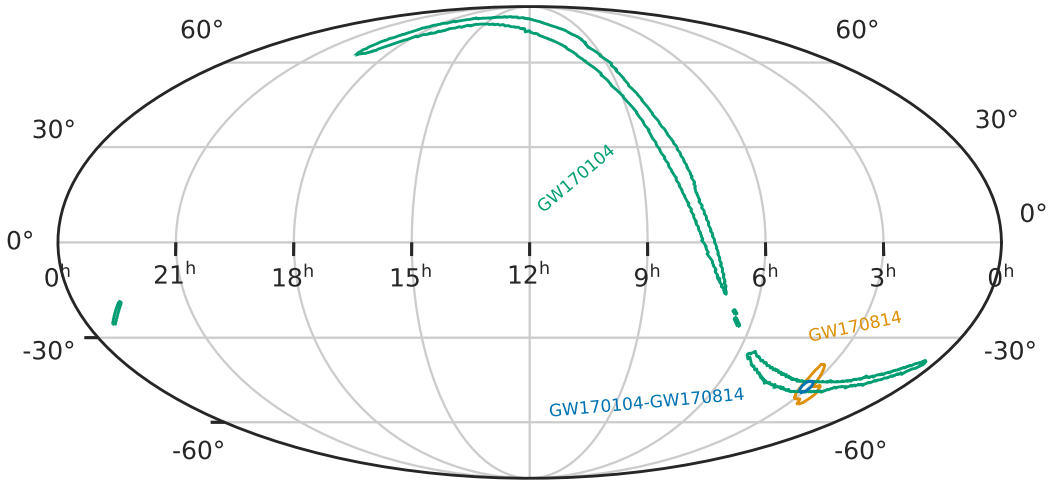

Figure 5.3: The contours show 90% confidence regions for the sky localizations posteriors of GW170104, GW170814 (treated as independent events) as well as the joint GW170104-GW170814 sky localization posterior inferred under the lensing hypothesis with a coalescence phase shift of $\pi/2$.

B_t can be large if the time delay is only a few days, such as for the GW170809-GW170814 and GW170818-GW170823 pairs, which results in $B_t \sim 6$.

The two Bayes factors B_U^L and B_t together with the prior odds for lensing, can be combined to compute the odds (Eq. 5.7). The lensed event rate is estimated for O2 to be $\sim 0.1\text{yr}^{-1}$ [121, 115]. During O2, there were eight events detected in nine months of observing time; therefore, the prior odds are ~ 0.009. In Fig. 5.2, we show the odds for events detected in O2. The odds for GW170104 and GW170814 with a $\pi/2$ coalescence phase shift is $O_U^L \sim 20$. It is the only pair of events that moderately prefers the lensing hypothesis even with prior information folded in. For other pairs detected in O2, we do not see any lensed evidence, as the odds are much less than 1.

Our B_t and prior odds estimations are based on galaxy lensing. However, the long time delay may point to lensing by a galaxy cluster. Galaxy cluster lensing is expected to be rare at O2 sensitivity. The prior probability of galaxy cluster lensing is $\sim 10^{-5}\text{yr}^{-1}$ [106]. Meanwhile, because the phase shift corresponds to π, or a type-III image as pointed out in

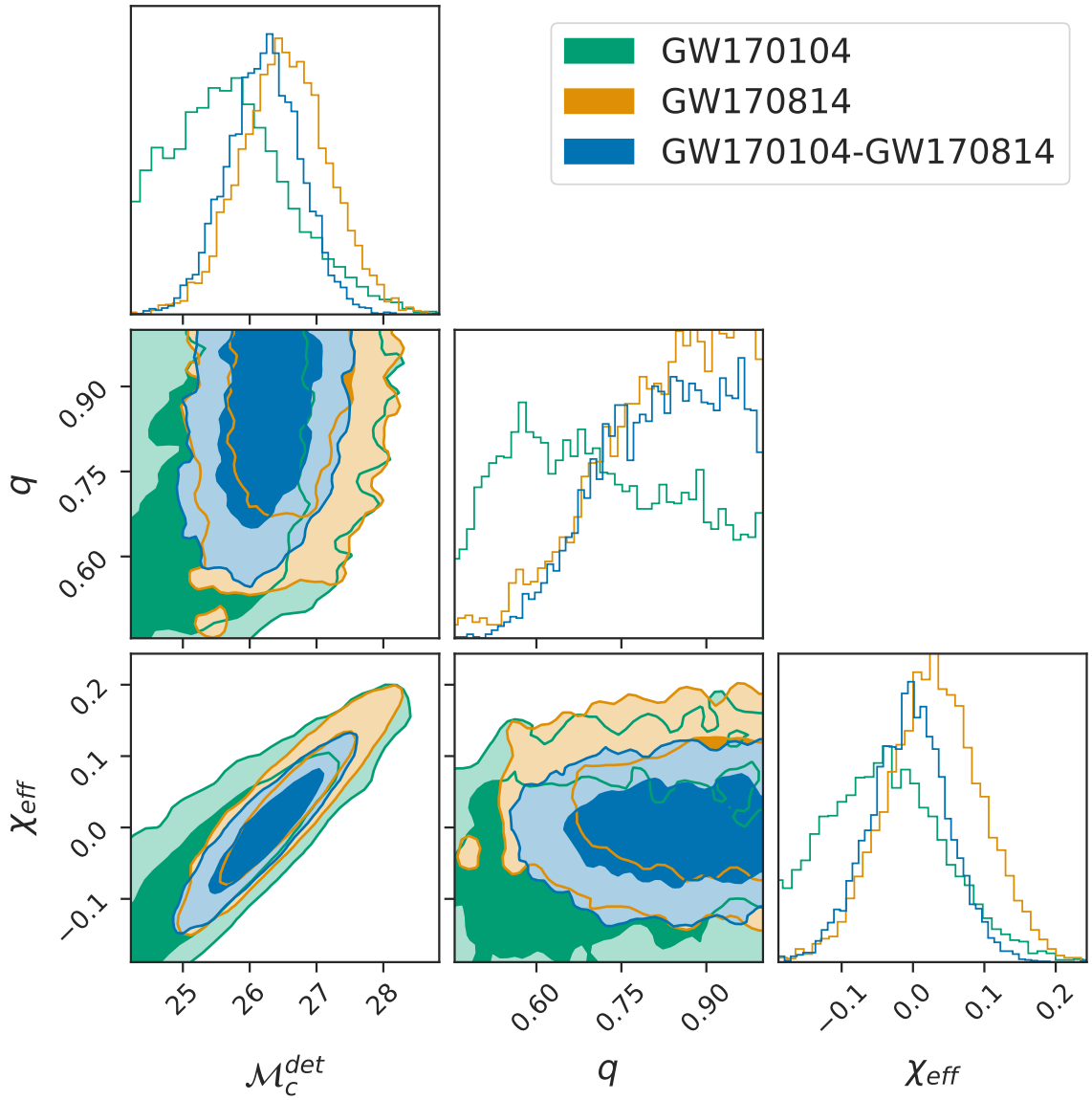

Figure 5.4: Corner plot showing the posterior distributions of the detector-frame chirp mass $\mathcal{M}_c$, mass ratio $q = m_2/m_1$, and the effective spin parameter χ_{eff}. We show the 68% and 98% credible regions for the independent GW170104, GW170814 posteriors as well the jointly inferred posteriors for the GW170104-GW170814 pair under the lensing hypothesis (with coalescence phase shift of $\pi/2$).

[109], the probability of lensing is further disfavored; The probability of observing type-III images should be very low, such that $p(n_j|\mathcal{H}_L) \ll 1$. Indeed, type-III images are rarely observed in the electromagnetic band.

5.4 Discussion and conclusions

To summarize, we used Bayesian model selection to identify lensed events in the second observing run of Advanced LIGO and Virgo. We test the lensing model with $0, \pi/4$, $\pi/2$, and $3\pi/4$ coalescence phase shifts and take care of selection effects. The most significant event pair is found to be GW170104-GW170814 at a very high Bayes factor; however, the two signals may come from two independent sources and have similar parameters, and therefore it is not clear if this is indicative of lensing. Moreover, the event is disfavored as a lensed candidate based on the understanding of lens configurations and the BBH and lens populations by an overwhelming amount; Indeed, the probability of observing lensing configurations with these types of time-delays and image configurations is low for both galaxies and galaxy clusters. The estimates of lensed rates and the relative contribution of galaxies and galaxy clusters may vary to some degree, but no current estimate predicts that galaxy cluster lensing should become prominent at O2 sensitivity.

Let us then entertain the possibility that the event was lensed. If this were the case, then unless we were to accept that we were simply incredibly lucky, it would likely imply all of the following:

1. The relative contribution of galaxy cluster lensing is more important than previously believed, which would explain the high time-delay between the events. Refs. [106, 107, 108, 110] have studied galaxy cluster lensing, and argued that highly magnified events have been historically observed more prominently lensed by galaxy cluster scale lenses.

2. The merger-rate density of binary black holes must rise at a significantly higher

rate than previously predicted. Indeed, the current lensing rate estimates rely on black holes tracing the star-formation rate density. For example, the Belczynski distribution is often used to model the merger-rate density [129]. Out of the studied models of black hole formation, none predict high enough merger rates that galaxy cluster lensing would become observable at O2 sensitivity [105].

3. Type-III images are more prominent for gravitational-wave sources than they are for electromagnetic sources.

Let us therefore state that extraordinary claims require extraordinary evidence. Based on the prior probability of lensing by these types of systems, we advise the reader to be very careful in interpreting the results. Indeed, in the absence of clear-cut evidence to the contrary, we must conclude that there is insufficient evidence to claim that the event is lensed, in agreement with [109] and [115].

However, two pieces of evidence could together possibly determine if the events were lensed. First, it is vital to perform injection campaigns to determine the probability of a non-lensed event. A similar study was conducted in [109] with false alarm probability between 10^{-4} and 10^{-2} for O2 events. Moreover, another intriguing possibility for cross-verification is through searches in the electromagnetic channels, as pointed out by [109]; if the events are lensed, then their host galaxy must also be lensed [130]. If the third event proposed as a lensed candidate for the pair in [109], then it would likely afford us three time delays, which would allow for a unique opportunity to localize the host galaxy and the galaxy cluster that lensed it in an electromagnetic follow up. Ref. [130, 131] demonstrated that such a search is possible for galaxies. We note that due to the rarity of galaxy clusters, the search is expected to be even more powerful for galaxy clusters. In the case of doubly lensed events, such as the GW170104-GW170814 pair, the single time-delay estimate may be quite degenerate with the lens parameters and the source alignment.

Bibliography

[1] J. D. E. Creighton and W. G. Anderson, *Gravitational-wave physics and astronomy: An introduction to theory, experiment and data analysis*, 2011.

[2] R. A. Isaacson, *Gravitational Radiation in the Limit of High Frequency. I. The Linear Approximation and Geometrical Optics*, Phys. Rev. **166**, 1263 (1968).

[3] R. A. Isaacson, *Gravitational Radiation in the Limit of High Frequency. II. Nonlinear Terms and the Ef fective Stress Tensor*, Phys. Rev. **166**, 1272 (1968).

[4] T. E. Collett et al., *Core or Cusps: The Central Dark Matter Profile of a Strong Lensing Cluster with a Bright Central Image at Redshift 1*, Astrophys. J. **843**, 148 (2017).

[5] L. Blanchet, G. Faye, B. R. Iyer, and B. Joguet, *Gravitational wave inspiral of compact binary systems to 7/2 postNewtonian order*, Phys. Rev. D **65**, 061501 (2002), [Erratum: Phys.Rev.D 71, 129902 (2005)].

[6] J. Aasi et al., *Advanced LIGO*, Class. Quant. Grav. **32**, 074001 (2015).

[7] B. P. Abbott et al., *Observation of Gravitational Waves from a Binary Black Hole Merger*, Phys. Rev. Lett. **116**, 061102 (2016).

[8] B. P. Abbott et al., *GWTC-1: A Gravitational-Wave Transient Catalog of Compact Binary Mergers Observed by LIGO and Virgo during the First and Second Observing Runs*, Phys. Rev. X **9**, 031040 (2019).

[9] B. P. Abbott et al., *GW151226: Observation of Gravitational Waves from a 22-Solar-Mass Binary Black Hole Coalescence*, Phys. Rev. Lett. **116**, 241103 (2016).

[10] F. Acernese et al., *Advanced Virgo: a second-generation interferometric gravitational wave detector*, Class. Quant. Grav. **32**, 024001 (2015).

[11] B. Abbott et al., *Prospects for Observing and Localizing Gravitational-Wave Transients with Advanced LIGO, Advanced Virgo and KAGRA*, Living Rev. Rel. **21**, 3 (2018).

[12] R. A. Hulse and J. H. Taylor, *Discovery of a pulsar in a binary system*, Astrophys. J. Lett. **195**, L51 (1975).

[13] J. H. Taylor and J. M. Weisberg, *A new test of general relativity: Gravitational radiation and the binary pulsar PS R 1913+16*, Astrophys. J. **253**, 908 (1982).

[14] B. P. Abbott et al., *GW170817: Observation of Gravitational Waves from a Binary Neutron Star Inspiral*, Phys. Rev. Lett. **119**, 161101 (2017).

[15] B. P. Abbott et al., *Gravitational Waves and Gamma-rays from a Binary Neutron Star Merger: GW170817 and GRB 170817A*, Astrophys. J. Lett. **848**, L13 (2017).

[16] B. P. Abbott et al., *Multi-messenger Observations of a Binary Neutron Star Merger*, Astrophys. J. Lett. **848**, L12 (2017).

[17] B. P. Abbott et al., *GWTC-1: A Gravitational-Wave Transient Catalog of Compact Binary Mergers Observed by LIGO and Virgo during the First and Second Observing Runs*, Phys. Rev. X **9**, 031040 (2019).

[18] R. Abbott et al., *GWTC-2: Compact Binary Coalescences Observed by LIGO and Virgo During the First Half of the Third Observing Run*, (2020).

[19] B. P. Abbott et al., *GW190425: Observation of a Compact Binary Coalescence with Total Mass* $\sim 3.4 M_{\odot}$, Astrophys. J. Lett. **892**, L3 (2020).

[20] R. Abbott et al., *GW190814: Gravitational Waves from the Coalescence of a 23 Solar Mass Black Hole with a 2.6 Solar Mass Compact Object*, Astrophys. J. Lett. **896**, L44 (2020).

[21] R. Abbott et al., *GW190521: A Binary Black Hole Merger with a Total Mass of* $150 M_{\odot}$, Phys. Rev. Lett. **125**, 101102 (2020).

[22] R. Abbott et al., *Properties and Astrophysical Implications of the 150* $M_{\odot}$ *Binary Black Hole Merger GW190521*, Astrophys. J. Lett. **900**, L13 (2020).

[23] B. P. Abbott et al., *Prospects for observing and localizing gravitational-wave transients with Advanced LIGO, Advanced Virgo and KAGRA*, Living Rev. Rel. **23**, 3 (2020).

[24] G. M. Harry, *Advanced LIGO: The next generation of gravitational wave detectors*, Class. Quant. Grav. **27**, 084006 (2010).

[25] B. P. Abbott et al., *GW170817: Measurements of neutron star radii and equation of state*, Phys. Rev. Lett. **121**, 161101 (2018).

[26] B. P. Abbott et al., *Model comparison from LIGO–Virgo data on GW170817's binary components and consequences for the merger remnant*, Class. Quant. Grav. **37**, 045006 (2020).

[27] B. F. Schutz, *Determining the Hubble Constant from Gravitational Wave Observations*, Nature **323**, 310 (1986).

[28] B. P. Abbott et al., *A gravitational-wave standard siren measurement of the Hubble constant*, Nature **551**, 85 (2017).

[29] W. L. Freedman et al., *Final results from the Hubble Space Telescope key project to measure the Hubble constant*, Astrophys. J. **553**, 47 (2001).

[30] B. P. Abbott et al., *Tests of general relativity with GW150914*, Phys. Rev. Lett. **116**, 221101 (2016), [Erratum: Phys.Rev.Lett. 121, 129902 (2018)].

[31] B. P. Abbott et al., *Tests of General Relativity with GW170817*, Phys. Rev. Lett. **123**, 011102 (2019).

[32] B. P. Abbott et al., *Tests of General Relativity with the Binary Black Hole Signals from the LIGO-Virgo Catalog GWTC-1*, Phys. Rev. D **100**, 104036 (2019).

[33] E. Payne, C. Talbot, and E. Thrane, *Higher order gravitational-wave modes with likelihood reweighting*, Phys. Rev. D **100**, 123017 (2019).

[34] J. W. T. Hessels et al., *A radio pulsar spinning at 716-hz*, Science **311**, 1901 (2006).

[35] W. G. Anderson, P. R. Brady, J. D. E. Creighton, and E. E. Flanagan, *An Excess power statistic for detection of burst sources of gravitational radiation*, Phys. Rev. D **63**, 042003 (2001).

[36] J. Veitch et al., *Parameter estimation for compact binaries with ground-based gravitational-wave observations using the LALInference software library*, Phys. Rev. D **91**, 042003 (2015).

[37] B. Allen, W. G. Anderson, P. R. Brady, D. A. Brown, and J. D. E. Creighton, *FINDCHIRP: An Algorithm for detection of gravitational waves from inspiraling compact binaries*, Phys. Rev. D **85**, 122006 (2012).

[38] N. J. Cornish and T. B. Littenberg, *BayesWave: Bayesian Inference for Gravitational Wave Bursts and Instrument Glitches*, Class. Quant. Grav. **32**, 135012 (2015).

[39] T. B. Littenberg and N. J. Cornish, *Bayesian inference for spectral estimation of gravitational wave detector noise*, Phys. Rev. D **91**, 084034 (2015).

[40] P. J. GREEN, *Reversible jump Markov chain Monte Carlo computation and Bayesian model determination*, Biometrika **82**, 711 (1995).

[41] S. Husa et al., *Frequency-domain gravitational waves from nonprecessing black-hole binaries. I. New numerical waveforms and anatomy of the signal*, Phys. Rev. D **93**, 044006 (2016).

[42] S. Khan et al., *Frequency-domain gravitational waves from nonprecessing black-hole binaries. II. A phenomenological model for the advanced detector era*, Phys. Rev. D **93**, 044007 (2016).

[43] A. Buonanno and T. Damour, *Effective one-body approach to general relativistic two-body dynamics*, Phys. Rev. D **59**, 084006 (1999).

[44] M. Hannam et al., *Simple Model of Complete Precessing Black-Hole-Binary Gravitational Waveforms*, Phys. Rev. Lett. **113**, 151101 (2014).

[45] L. London et al., *First higher-multipole model of gravitational waves from spinning and coalescing black-hole binaries*, Phys. Rev. Lett. **120**, 161102 (2018).

[46] T. Dietrich, S. Bernuzzi, and W. Tichy, *Closed-form tidal approximants for binary neutron star gravitational waveforms constructed from high-resolution numerical relativity simulations*, Phys. Rev. D **96**, 121501 (2017).

[47] T. Dietrich et al., *Matter imprints in waveform models for neutron star binaries: Tidal and self-spin effects*, Phys. Rev. D **99**, 024029 (2019).

[48] A. Bohé et al., *Improved effective-one-body model of spinning, nonprecessing binary black holes for the era of gravitational-wave astrophysics with advanced detectors*, Phys. Rev. D **95**, 044028 (2017).

[49] M. Pürrer, *Frequency domain reduced order models for gravitational waves from aligned-spin compact binaries*, Class. Quant. Grav. **31**, 195010 (2014).

[50] N. Metropolis et al., *Equation of State Calculations by Fast Computing Machines*, J. Chem. Phys. **21**, 1087 (1953).

[51] W. Hastings, *Monte Carlo sampling methods using Markov chains and their applications*, Biometrika **57**, 97 (1970).

[52] J. Veitch et al., *Parameter estimation for compact binaries with ground-based gravitational-wave observations using the LALInference software library*, Phys. Rev. D **91**, 042003 (2015).

[53] J. Skilling, *Nested sampling for general Bayesian computation*, Bayesian Anal. **1**, 833 (2006).

[54] LIGO Scientific Collaboration, LIGO Algorithm Library - LALSuite, free software (GPL), 2018.

[55] J. R. Oppenheimer and G. M. Volkoff, *On Massive neutron cores*, Phys. Rev. **55**, 374 (1939).

[56] R. C. Tolman, *Effect of Inhomogeneity on Cosmological Models*, Proceedings of the National Academy of Science **20**, 169 (1934).

[57] R. C. Tolman, *Static Solutions of Einstein's Field Equations for Spheres of Fluid*, Physical Review **55**, 364 (1939).

[58] L. Lindblom, *Determining the Nuclear Equation of State from Neutron-Star Masses and Radii*, Astrophys. J. **398**, 569 (1992).

[59] F. Özel and P. Freire, *Masses, Radii, and the Equation of State of Neutron Stars*, Ann. Rev. Astron. Astrophys. **54**, 401 (2016).

[60] J. S. Read, B. D. Lackey, B. J. Owen, and J. L. Friedman, *Constraints on a phenomenologically parameterized neutron-star equation of state*, Phys. Rev. D **79**, 124032 (2009).

[61] A. W. Steiner et al., *Constraining the Mass and Radius of Neutron Stars in Globular Clusters*, Mon. Not. Roy. Astron. Soc. **476**, 421 (2018).

[62] N. Baillot d'Etivaux et al., *New constraints on the nuclear equation of state from the thermal emission of neutron stars in quiescent low-mass X-ray binaries*, Astrophys. J. **887**, 48 (2019).

[63] E. E. Flanagan and T. Hinderer, *Constraining neutron star tidal Love numbers with gravitational wave detectors*, Phys. Rev. D **77**, 021502 (2008).

[64] L. Wade et al., *Systematic and statistical errors in a bayesian approach to the estimation of the neutron-star equation of state using advanced gravitational wave detectors*, Phys. Rev. D **89**, 103012 (2014).

[65] T. Hinderer et al., *Effects of neutron-star dynamic tides on gravitational waveforms within the effective-one-body approach*, Phys. Rev. Lett. **116**, 181101 (2016).

[66] B. P. Abbott et al., *Constraining the p-Mode–g-Mode Tidal Instability with GW170817*, Phys. Rev. Lett. **122**, 061104 (2019).

[67] S. Ghosh et al., *Rapid model comparison of equations of state from gravitational wave observation of binary neutron star coalescences*, arXiv e-prints , arXiv:2104.08681 (2021).

[68] X. Liu et al., *Measuring the speed of gravitational waves from the first and second observing run of Advanced LIGO and Advanced Virgo*, Phys. Rev. D **102**, 024028 (2020).

[69] B. P. Abbott et al., *Observation of Gravitational Waves from a Binary Black Hole Merger*, Phys. Rev. Lett. **116**, 061102 (2016).

[70] B. P. Abbott et al., *Binary Black Hole Mergers in the first Advanced LIGO Observing Run*, Phys. Rev. X **6**, 041015 (2016).

[71] B. P. Abbott et al., *GW151226: Observation of Gravitational Waves from a 22-Solar-Mass Binary Black Hole Coalescence*, Phys. Rev. Lett. **116**, 241103 (2016).

[72] B. P. Abbott et al., *GW170104: Observation of a 50-Solar-Mass Binary Black Hole Coalescence at Redshift 0.2*, Phys. Rev. Lett. **118**, 221101 (2017), [Erratum: Phys.Rev.Lett. 121, 129901 (2018)].

[73] B. P. Abbott et al., *GW170608: Observation of a 19-solar-mass Binary Black Hole Coalescence*, Astrophys. J. **851**, L35 (2017).

[74] B. P. Abbott et al., *GW170814: A Three-Detector Observation of Gravitational Waves from a Binary Black Hole Coalescence*, Phys. Rev. Lett. **119**, 141101 (2017).

[75] N. Cornish, D. Blas, and G. Nardini, *Bounding the Speed of Gravity with Gravitational Wave Observations*, Phys. Rev. Lett. **119**, 161102 (2017).

[76] B. P. Abbott et al., *Gravitational Waves and Gamma-rays from a Binary Neutron Star Merger: GW170817 and GRB 170817A*, Astrophys. J. Lett. **848**, L13 (2017).

[77] R. Ciolfi and D. Siegel, Short gamma-ray bursts in the "time-reversal" scenario, in *APS April Meeting Abstracts*, volume 2015 of *APS Meeting Abstracts*, page E14.004, 2015.

[78] L. Rezzolla and P. Kumar, *A novel paradigm for short gamma-ray bursts with extended X-ray emission*, Astrophys. J. **802**, 95 (2015).

[79] D. Tsang, J. S. Read, T. Hinderer, A. L. Piro, and R. Bondarescu, *Resonant Shattering of Neutron Star Crusts*, Phys. Rev. Lett. **108**, 011102 (2012).

[80] V. A. Kostelecký and N. Russell, *Data tables for Lorentz and CPT violation*, *Data tables for Lorentz and CPT violation*, 2018 Edition, .

[81] D. Colladay and V. A. Kostelecky, *Lorentz violating extension of the standard model*, Phys. Rev. D **58**, 116002 (1998).

[82] V. A. Kostelecky, *Gravity, Lorentz violation, and the standard model*, Phys. Rev. D **69**, 105009 (2004).

[83] Q. G. Bailey and V. A. Kostelecky, *Signals for Lorentz violation in post-Newtonian gravity*, Phys. Rev. D **74**, 045001 (2006).

[84] V. A. Kostelecký and M. Mewes, *Testing local Lorentz invariance with gravitational waves*, Phys. Lett. B **757**, 510 (2016).

[85] M. Mewes, *Signals for Lorentz violation in gravitational waves*, Phys. Rev. D **99**, 104062 (2019).

[86] R. Xu, *Modifications to Plane Gravitational Waves from Minimal Lorentz Violation*, Symmetry **11**, 1318 (2019).

[87] L. Shao, *Combined search for anisotropic birefringence in the gravitational-wave transient catalog GWTC-1*, Phys. Rev. D **101**, 104019 (2020).

[88] N. A. Flowers, C. Goodge, and J. D. Tasson, *Superconducting-Gravimeter Tests of Local Lorentz Invariance*, Phys. Rev. Lett. **119**, 201101 (2017).

[89] M. Hannam et al., *Simple Model of Complete Precessing Black-Hole-Binary Gravitational Waveforms*, Phys. Rev. Lett. **113**, 151101 (2014).

[90] B. S. Sathyaprakash and S. V. Dhurandhar, *Choice of filters for the detection of gravitational waves from coalescing binaries*, Phys. Rev. D **44**, 3819 (1991).

[91] J. Vines, E. E. Flanagan, and T. Hinderer, *Post-1-Newtonian tidal effects in the gravitational waveform from binary inspirals*, Phys. Rev. D **83**, 084051 (2011).

[92] B. Mikoczi, M. Vasuth, and L. A. Gergely, *Self-interaction spin effects in inspiralling compact binaries*, Phys. Rev. D **71**, 124043 (2005).

[93] A. Bohe, S. Marsat, and L. Blanchet, *Next-to-next-to-leading order spin–orbit effects in the gravitational wave flux and orbital phasing of compact binaries*, Classical and Quantum Gravity **30**, 135009 (2013).

[94] A. Bohe, G. Faye, S. Marsat, and E. K. Porter, *Quadratic-in-spin effects in the orbital dynamics and gravitational-wave energy flux of compact binaries at the 3PN order*, Classical and Quantum Gravity **32**, 195010 (2015).

[95] K. G. Arun, A. Buonanno, G. Faye, , and E. Ochsner, *Higher-order spin effects in the amplitude and phase of gravitational waveforms emitted by inspiraling compact binaries: Ready-to-use gravitational waveforms*, Phys. Rev. D **79**, 104023 (2009).

[96] B. P. Abbott et al., *Multi-messenger Observations of a Binary Neutron Star Merger*, Astrophys. J **848**, 2 (2017).

[97] A. Bonilla, R. D'Agostino, R. C. Nunes, and J. C. N. de Araujo, *Forecasts on the speed of gravitational waves at high z*, JCAP **2020**, 015 (2020).

[98] B. P. Abbott et al., *Tests of General Relativity with GW170817*, Phys. Rev. Lett. **123**, 011102 (2019).

[99] B. P. Abbott et al., *Tests of General Relativity with the Binary Black Hole Signals from the LIGO-Virgo Catalog GWTC-1*, Phys. Rev. D **100**, 104036 (2019).

[100] Y. Hagihara, N. Era, D. Iikawa, A. Nishizawa, and H. Asada, *Constraining extra gravitational wave polarizations with Advanced LIGO, Advanced Virgo and KAGRA and upper bounds from GW170817*, Phys. Rev. D **100**, 064010 (2019).

[101] B. P. Abbott et al., *GW150914: First results from the search for binary black hole coalescence with Advanced LIGO*, Phys. Rev. D **93**, 122003 (2016).

[102] X. Liu, I. M. Hernandez, and J. Creighton, *Identifying strong gravitational-wave lensing during the second observing run of Advanced LIGO and Advanced Virgo*, Astrophys. J. **908**, 97 (2021).

[103] K. Haris, A. K. Mehta, S. Kumar, T. Venumadhav, and P. Ajith, *Identifying strongly lensed gravitational wave signals from binary black hole mergers*, arXiv e-prints , arXiv:1807.07062 (2018).

[104] S.-S. Li, S. Mao, Y. Zhao, and Y. Lu, *Gravitational lensing of gravitational waves: A statistical perspective*, Mon. Not. Roy. Astron. Soc. **476**, 2220 (2018).

[105] M. Oguri, *Effect of gravitational lensing on the distribution of gravitational waves from distant binary black hole mergers*, Mon. Not. Roy. Astron. Soc. **480**, 3842 (2018).

[106] G. P. Smith et al., *What if LIGO's gravitational wave detections are strongly lensed by massive galaxy clusters?*, Mon. Not. Roy. Astron. Soc. **475**, 3823 (2018).

[107] G. Smith et al., *Strong-lensing of Gravitational Waves by Galaxy Clusters*, IAU Symp. **338**, 98 (2017).

[108] G. Smith et al., *Deep and rapid observations of strong-lensing galaxy clusters within the sky localization of GW170814*, Mon. Not. Roy. Astron. Soc. **485**, 5180 (2019).

[109] L. Dai, B. Zackay, T. Venumadhav, J. Roulet, and M. Zaldarriaga, *Search for Lensed Gravitational Waves Including Morse Phase Information: An Intriguing Candidate in O2*, (2020).

[110] A. Robertson et al., *What does strong gravitational lensing? The mass and redshift distribution of high-magnification lenses*, (2020).

[111] S. Mukherjee, T. Broadhurst, J. M. Diego, J. Silk, and G. F. Smoot, *Inferring the lensing rate of LIGO-Virgo sources from the stochastic gravitational wave background*, (2020).

[112] R. Buscicchio et al., *Constraining the lensing of binary black holes from their stochastic background*, (2020).

[113] Y. Wang, A. Stebbins, and E. L. Turner, *Gravitational lensing of gravitational waves from merging neutron star binaries*, Phys. Rev. Lett. **77**, 2875 (1996).

[114] R. Narayan and M. Bartelmann, *Lectures on Gravitational Lensing*, arXiv e-prints , astro (1996).

[115] O. A. Hannuksela et al., *Search for gravitational lensing signatures in LIGO-Virgo binary black hole events*, Astrophys. J. Lett. **874**, L2 (2019).

[116] L. Dai, T. Venumadhav, and K. Sigurdson, *Effect of lensing magnification on the apparent distribution of black hole mergers*, Phys. Rev. D **95**, 044011 (2017).

[117] R. Takahashi and T. Nakamura, *Wave effects in gravitational lensing of gravitational waves from chirping binaries*, Astrophys. J. **595**, 1039 (2003).

[118] L. Dai and T. Venumadhav, *On the waveforms of gravitationally lensed gravitational waves*, arXiv e-prints , arXiv:1702.04724 (2017).

[119] J. M. Ezquiaga, D. E. Holz, W. Hu, M. Lagos, and R. M. Wald, *Phase effects from strong gravitational lensing of gravitational waves*, (2020).

[120] H. Dahle et al., *SDSSJ2222+2745 A Gravitationally Lensed Sextuple Quasar with Maximum Image Separation of 15.1' Discovered in the Sloan Giant Arcs Survey*, Astrophys. J. **773**, 146 (2013).

[121] K. K. Y. Ng, K. W. K. Wong, T. Broadhurst, and T. G. F. Li, *Precise LIGO Lensing Rate Predictions for Binary Black Holes*, Phys. Rev. D **97**, 023012 (2018).

[122] A. H. Nitz et al., *2-OGC: Open Gravitational-wave Catalog of binary mergers from analysis of public Advanced LIGO and Virgo data*, Astrophys. J. **891**, 123 (2019).

[123] R. Blandford and R. Narayan, *Fermat's principle, caustics, and the classification of gravitational lens images*, Astrophys. J. **310**, 568 (1986).

[124] E. Thrane and C. Talbot, *An introduction to Bayesian inference in gravitational-wave astronomy: parameter estimation, model selection, and hierarchical models*, Publ. Astron. Soc. Austral. **36**, e010 (2019), [Erratum: Publ.Astron.Soc.Austral. 37, e036 (2020)].

[125] B. Abbott et al., *Binary Black Hole Population Properties Inferred from the First and Second Observing Runs of Advanced LIGO and Advanced Virgo*, Astrophys. J. Lett. **882**, L24 (2019).

[126] A. K. Li et al., *Targeted Sub-threshold Search for Strongly-lensed Gravitational-wave Events*, (2019).

[127] C. McIsaac et al., *Search for Strongly Lensed Counterpart Images of Binary Black Hole Mergers in the First Two LIGO Observing Runs*, (2019).

[128] T. Broadhurst, J. M. Diego, and I. Smoot, George F., *Twin LIGO/Virgo Detections of a Viable Gravitationally-Lensed Black Hole Merger*, arXiv e-prints , arXiv:1901.03190 (2019).

[129] K. Belczynski, D. E. Holz, T. Bulik, and R. O'Shaughnessy, *The first gravitational-wave source from the isolated evolution of two 40-100 Msun stars*, Nature **534**, 512 (2016).

[130] O. A. Hannuksela, T. E. Collett, M. Çalı şkan, and T. G. Li, *Localizing merging black holes with sub-arcsecond precision using gravitational-wave lensing*, (2020).

[131] H. Yu, P. Zhang, and F.-Y. Wang, *Strong lensing as a giant telescope to localize the host galaxy of gravitational wave event*, Mon. Not. Roy. Astron. Soc. **497**, 204 (2020).

Curriculum Vitae

Xiaoshu Liu

Education

University of Wisconsin-Milwaukee
Ph.D., Physics, May 2021

Shanghai University
B.E., Applied Physics, July 2014

Publications

Short Author List Publications

X. Liu, I. M. Hernandez, and J. Creighton, Identifying strong gravitational-wave lensing during the second observing run of Advanced LIGO and Advanced Virgo, Astrophys. J. 908, 97 (2021).

X. Liu, V. He, T. Mikulski, D. Palenova, C. Williams, J. Creighton, and J. Tasson, Measuring the speed of gravitational waves from the first and second observing run of Advanced LIGO and Advanced Virgo, Phys. Rev. D 102, 024028 (2020).

S. Ghosh, X. Liu, J. Creighton, W. Kastaun, G. Pratten, and I. M. Hernandez, Rapid model comparison of equations of state from gravitational wave observation of binary neutron star coalescences, arXiv:2104.08681 (2021).

Collaboration Publications (Contributing)

B. P. Abbott et al., GW190425: Observation of a Compact Binary Coalescence with Total Mass $\sim 3.4 M_{\odot}$, Astrophys. J. Lett. 892, L3 (2020).

B. P. Abbott et al., Search for lensing signatures in the gravitational-wave observations from the first half of LIGO-Virgo's third observing run, in preparation (2021).

Presentations

Identifying strong gravitational-wave lensing during the second observing run of Advanced LIGO and Advanced Virgo, 30th Annual Midwest Relativity Meeting, Notre Dame, IN (October 2020).

Measuring tidal deformability of binary neutron stars with gravitational-wave signals, CGCA Seminar, Milwaukee, WI (May 2018).